COMPLEX MODE THEORY AND APPLICATIONS IN SILICON PHOTONICS

COMPLEX MODE THEORY AND APPLICATIONS IN SILICON PHOTONICS

BY

HAIBO LIANG. B. Eng

A Thesis

Submitted to the School of Graduate Studies

in Partial Fulfillment of the Requirements

for the Degree of

Doctor of Philosophy

Doctor of Philosophy (2016) McMaster University

(Electrical and Computer Engineering) Hamilton, Ontario, Canada

TITLE:	Complex Mode Theory and Applications in Silicon Photonics
AUTHOR:	Haibo Liang B. Eng., (Electronics and Information Engineering) University of Science and Technology of China
SUPERVISORS:	Prof. Wei-Ping Huang, Prof. Xun Li
NUMBER OF PAGES:	xx, 152

Abstract

Silicon photonics has witnessed rapid development in recent years for its fabrication compatibility with the cost-effective CMOS technology. The advancement of relevant simulation tools, however, is at a relatively slow pace. The high index contrast of the usual silicon waveguide that has imposed new challenges to the convergence and accuracy of the solution technique, the growing intricacy in solitary component design, and the increased complexity of their integration, are the impelling factors that motivate us to improve the computer-aided design, modeling, simulation, and optimization methods.

The theme of the thesis is on the frequency domain simulation methods supported by the complex mode theory. The complex mode theory is introduced to the simulation domain truncated by the perfectly matching layers (PMLs) enclosed in the perfectly reflected boundaries (PRBs), wherein the discrete complex modes as eigen solutions can represent the continuous radiation fields, thus yields a unified approach for handling both guided (discrete) and radiation (continuous) waves.

In this thesis, theoretical investigations have been conducted along a few different lines aiming at improving the efficiency and accuracy in complex mode expansion. Properties of high-order complex Berenger modes are firstly addressed through asymptotic solutions, and it is found that as the mode order increases, the symmetry of the cladding and substrate in the simulation domain, instead of the guiding schemes, plays a more and more decisive role regarding mode classification and modal field distribution. A weighed optical path method is then proposed to unify the high-order Berenger modes, and to enhance the symmetry of high order modes' field distributions in the asymmetric structures, leading to the improvement in convergence speed and stability in the mode expansion. Next, an improved mode-matching method (MMM) is proposed based on an error-minimizing method instead of the conventional approach relying on the unreliable modal orthogonal property. The newly proposed method is significantly more robust as numerical errors usually jeopardize the modal orthogonality. This claim is exemplified by simulation results on silicon channel waveguide facet, bending waveguide, and silicon-germanium photo-detector waveguide.

As a direct application of the improved complex mode theory, a hybrid plasmonic-photonic nano-ribbon waveguide is proposed, standing as a combination of the silicon slot and surface plasmon polariton (SPP) waveguides, is proposed and analyzed. We have found that the fundamental mode is featured at low loss as in optical waveguide as well as high confinement as in plasmonic structure. Simulations have shown that millimeter range propagation can be sustained with strong confinement. We have further studied such waveguide with an extra layer of phase changing material incorporated, attempting

to realize the efficient electro-optical phase and/or loss modulation. Finally, an optical switch design is proposed by taking the full advantage of the aforementioned structure.

Acknowledgments

I would like to express my deepest gratitude to Dr. Wei-Ping Huang and Dr. Xun Li as my co-supervisors during my Ph. D. career, for their patient and insightful guidance and instructions.

I would like to express my sincere thanks to the committee members, Prof. Shiva Kumar and Prof. Chang-Qing Xu, for their precious suggestions, comments and encouragement in my research. I also greatly appreciate Dr. Jian-Wei Mu and Dr. Richard A. Soref, for their instructions, advices, and discussions with plenty of wisdom and mind-blowing ideas during the academic cooperations. I would like to thank Dr. Lin Han and Dr. Jia Zhao for their generous help for my research. I also owe my appreciation to Dr. A. Patriciu, Dr. M. Bakr, Dr. J. P. Reilly and Dr. T. N. Davidson for all the knowledge imparted.

I would like to thank Ms. Cheryl Gies for her administrative works and encouragement. I am also grateful to all my colleagues in Photonics CAD Lab for the friendship and companionship.

Finally, my great gratitude to my parents for their love and support.

Abbreviations

PML	perfectly matched layer
PRB	perfectly reflecting boundary
MMM	mode matching method
FDTD	finite difference time domain
BPM	beam propagation method
FDM	finite difference method
FEM	finite element method
SPP	surface plasmon polariton
GST	$Ge_2Sb_2Te_5$
TE	transverse electric
TM	transverse magnetic
1D	one dimension
2D	two dimension
3D	three dimension

HSSPP	hybrid slot/SPP
CGC	conductor gap conductor
CGD	conductor gap dielectric
DGCGD	dielectric gap conductor gap dielectric
SOI	silicon-on-insulator
IL	insertion loss
ER	extinction ratio
CT	crosstalk
SGS	Si/GST/Si
SIGIS	Si/ITO/GST/ITO/Si
SGIG	Si/GST/ITO/GST/Si
VOA	variable optical attenuator
SiN	silicon nitride
UOPD	unadjusted optical path distance
WOPD	weighted optical path distance
CMMM	conventional MMM
IMMM	improved MMM

Contents

List of Tables

List of Figures

Chapter 1.

Introduction

1.1 Research background

1.1.1. Recent development in silicon photonics

Silicon Photonics[1]~[4] is featured with compactness, scalability, and compatibility with the dominant CMOS technology. Recent developments in silicon photonics can be categorized into either passive or active components. For passive components, thanks to the high index contrast in the silicon on insulator platform and fairly smooth surface roughness[5], superior features including high confinement, small propagation loss, small bending loss, and high compactness can be expected. In the silicon photonics circuits or systems, the major role of passive devices is to transmit signals. High quality silicon channel waveguide[6], ridge waveguide[7], and low loss bending structures[8] have been proposed and fabricated, along with y-branches[9], multi-modal interfaces[10], directional couplers[11], and crossing structures[12] with low insertion loss and low

crosstalk forming the signal routing circuits. Components with band pass or band rejection filtering properties are also available in silicon photonics mainly for the wavelength division multiplexing use, like the Mach-Zander interferometers[13][14], ring or disk resonators[15], Bragg gratings[16], and arrayed waveguide gratings [17]. The grating couplers [18]which can covert the in-plane wave to the vertical direction radiation wave or vise versa, are often used as the optical input-output components connected with optical fibers. Besides, special waveguide structures such as photonic crystal [6] and the surface plasmon polariton (SPP) waveguides [19] can also be realized on a silicon photonics platform.

Though the silicon is not suitable for lasing for its direct bandgap feature, silicon photonics devices can still generalize some "active effects". Through doping in the ridge waveguides or deposit functional electro-optical layers in the channel waveguides, current or voltage controlled phase and/or loss modulations can be realized. The free carrier injection induced plasmon diffusion effect is widely used by building lateral p-n or p-i-n structures in the doped silicon ridge waveguide[20]. Thermal tuning is another way to realize the phase and/or loss modulation[21]. Except for the ridge waveguides, embedding functional layers into silicon channel waveguides, is another way to realize the phase and/or loss modulations. For example, the organic polymer layers with the second-order Pockels effect[22], the conductor-like doped indium tin oxide (ITO) with strong plasmon diffusion effect[23], and the phase change materials like VO_2[24] or $Ge_2Sb_2Te_5$ (GST)[25] with the self-sustained states which can be switched by external optical or electrical pulps are all possible in the silicon photonics devices. Different from

the ridge waveguides adopting the lateral doping mostly, the channel waveguides with embedded active functional layers usually use vertical doping, and normally yielding larger phase and/or loss modulation depth due to a stronger interaction between light and the special materials.

1.1.2. Simulation methods for silicon photonics

Akin to the electronic integrated circuit designs [26],[27], the computer aid simulation is the first step of the design and fabrication cycle for silicon photonics integrated deveices and circuits, and of great necessity to avoid worthless, repeated yet expansive fabrications and tests. The mainstream simulation methods for silicon photonics can be divided into two categories based on the analysis domain: time-domain simulation and frequency-domain simulation. For the time-domain methods, the most eminent competitor is the finite-difference time-domain (FDTD) method [28][29]. FDTD is always viewed as a universal simulation tool, because it simply discretizes the Maxwell equations in time and space domains without any further approximation. With sufficiently small discretization steps, the simulation will converge to the accurate solution theoretically. However, the accuracy is not the only concern in simulations for silicon photonics devices or circuits, the flexibility and efficiency in optimization and integration processes are also important. As FDTD discretize the space in all three dimensions and then iterate in discretized time sequences, all the field values at all the mesh nodes and in some case at every time slice are needed to be stored, which is not a storage friendly and efficient method especially for large scale devices or systems. In addition, FDTD simulation starts from the transient

analysis, which is unnecessary for problems only involving steady states, and takes much longer time iterating in the time domain. This issue becomes more serious when the resonance effect is involved. Besides, frequency domain simulation methods are much more suitable for the extremely dispersive medium.

With some pre-knowledge about the target structures, the simulation can be simplified to save huge time and computer storage consumption. As for the problems involving only single frequency at the steady state, the frequency domain simulation methods are superior to the FDTD. The beam propagation method (BPM) [30] is a practical tool in this class, with the merits of suitability for relatively arbitrary shapes, feasibility for radiation field simulations with modified operators [31][32], etc. However, as BPM is adopting the slow-varying envelope approximation, it will be very challenging to simulate structures with large angles or/and with high index contrast, which are the inevitable features of most silicon photonics devices.

1.2 Development of the mode theory

The mode theory provides an alternative simulation methodology instead of BPM and FDTD. The modes are the eigen-solutions of Maxwell equations in the transverse plane of a certain structure, and will propagate in the longitudinal direction without dispersion if the structure is homogeneous along the propagation direction. As a complete set, modes can expand spatially arbitary fields satisfying the same boundary conditions of the studied waveguides.

The modal analysis (the simulation methods from mode theory) shows significant strength in the waveguide design, in which the guided modes are the major design targets, and through modal analysis, important properties such as propagation constants, loss coefficients, confinements, etc., can be determined and investigated simply through mode solvers [19][25]. When the waveguide propagation meets the discontinuities and interfaces, scattering phenomenon appears and radiation fields emerge. The scattering problem can be handled through modal analysis methods such as mode matching method (MMM) [33][34], or coupled mode theory [35][36].

The advantages of modal analysis can be asserted into four aspects. First, the modal analysis methods can be formulated analytically without approximation of discretization. Unlike the FDTD, which needs discretization in all four dimensions, modal analysis only needs two dimension discretization at most for mode solutions at the initial stage making it a semi-analytical method. Second, via the modal expansion, the simulations of electromagnetic fields will be transferred from the field domain dealing with differential equations to the mode domain with linear algebra calculations regarding the modal coefficients only, which is much simpler in the mathematical derivation, easier for the numerical simulation, and with much fewer data for storage. Third, when we escalate the simulation from the device level to the system level, modes are always selected and extracted as the port parameters in the scattering matrices parameterizing the devices as in the lumped model, which is a similar simulation manner as in the electronics integrated circuit [37]. Fourth, mode theory always provides clear physics insights for the device operating principles.

1.2.1. Guided mode model

The earlier mode theory was mainly employing the guided modes, and several key issues in waveguides such as the propagation constant, loss, dispersion, field confinement, excitement, and the transmission/reflection of guided waves, etc., could be well handled. However, the guided modes alone cannot form a complete mode set, and they cannot represent the radiation effect along the propagation. However, radiation fields are important, sometimes even dominant in silicon photonics, such as in the evanescent coupling (directional coupler, bus-ring resonator, etc.), scattering problems (waveguide junction, fact, crossing, etc.), and the leaky structures (bending, taper, grating, etc.).

1.2.2. Open waveguide model

The rigorous simulation to the radiation fields is challengeable, and is also the motivation of development of mode theory. Other than the microwave structures, the silicon photonics devices are mostly open structures without any metallic structures acting as reflecting boundaries, and the electro-magnetic fields will fill in the entire space. The accurate and physical simulation model for silicon photonics should be the open structure model with nature boundaries located at the infinities.

The complete mode set of an open waveguide structure could be classified into four types: guided modes, leaky modes, radiation modes and evanescent modes [38][39]. Regarding the modal indies, the guided modes and leaky modes are both discrete, and are pure real or complex, respectively. The radiation modes and evanescent modes are of continuous modal indies, and are real or imagery respectively. As for the field

distributions, the guide modes have standing waves in the guiding region, and evanescent waves in the ambient environment, decaying to zeros at the infinities. The leaky modes are the opposite, their fields are exponentially increasing in terms of field intensity in the surrounding area, and will diverge at the infinities. Thus, the leaky modes are not physical but only mathematical solutions of Maxwell equations. The radiation modes and evanescent modes will have standing wave distributions outside the guiding region. Finally, regarding the propagation situation along the longitudinal direction, guided modes and radiation modes are normally lossless if the waveguide does not consists of any lossy medium. The leaky modes and evanescent modes decay exponentially with the progress of mode propagation forwardly.

In the open waveguide model, as the guided modes, radiation modes, and evanescent modes are already forming a complete mode set, they can be used to expand arbitrary field directly. Though straightforward, this method is troublesome in formulation and simulation. First, due to the unbounded feature, radiation and evanescent modes are incompatible with the numerical methods based on discretization such as finite difference method (FDM), or finite element method (FEM), which makes them unattainable for most practical structures with complicated transverse configuration, leaving only limited simple cases with analytical solutions. Also unbounded modes cannot be normalized. Second, because of the continuous modes spectrum, tedious integrations are involved in the modal analysis algorithm, like mode expansion, MMM, and coupled mode theory.

The leaky modes, though are not part of the complete mode set and physically non-existing solutions of Maxwell equations, could be utilized to represent radiation loss under certain constraints [40]~[43]. Though leaky modes are discrete, they are still unbounded and grow exponentially in the waveguide cladding and substrate; so they cannot be treated uniformly in terms of normalization and orthogonality as are guided modes.

1.2.3. Box mode model

Therefore, an ideal simulation model must bear discrete modes with boundaries instead of the "unbounded and continuous" modes in open structure. Besides, though boundaries are introduced to yield bounded modes, they must not influence the fields inside, as the target simulation structure is still the open structure with no reflections from the ambient environment. Also, the guided and leaky modes determined by the guiding structures are also need to be preserved.

The most straightforward and highly intuitive approach is to enclose the waveguide with perfectly reflecting boundaries (PRBs) [44].The key assumption of the above computation model is that the computation window, i.e., the size of the artificial box is much larger than the dimension of waveguide, e.g., the thickness of the guiding region. Under this assumption, the closed waveguide (waveguide with the perfectly reflecting boundaries or ideal metals) is expected to be a good approximation to the open waveguide. Consequently, the guided modes in the open waveguide structure correspond to the guided modes in the close waveguide structure and are not affected, whereas the radiation

modes and evanescent modes in the open waveguide structure correspond to the box-guided and box-evanescent modes in the close waveguide. The box-guided modes are the modes confined by the PRBs. They have real propagation constants, which means no loss in propagation. In the field distribution, the standing wave can be observed in the whole domain due to the reflection from PRBs. As for the box-evanescent modes, they are sharing similar transverse field distributions as the box-guided modes, only with purely imagery propagation constants, which means exponentially decay will be observed in the modal propagation progress. The box-guided and box-evanescent modes are providing high order spatial frequency components in the modal expansion. Such a model avoids the difficulties with the continuous radiation modes and can treat all modes equally to describe the guided and radiation fields of an open waveguide.

Nevertheless, reflections from the edges of the computation widow always exist regardless the size of the box as long as it remains finite. The reflection is always in the field distribution of box-guided and evanescent modes. Such reflection will impact the accuracy of simulation for radiative fields, especially when the window size is not very large so as to the number of box modes are not excessive. On the other hand, to enlarge the window will reduce the effect of the reflection but at the same time increase the number of modes and hence defeating the original purpose of discretization for simplicity. Not to mention the extra computational resource consumed with enlarged computational window in numerical simulations.

1.2.4. Complex mode model

To tackle the reflection from PRBs, the absorbing boundaries have been introduced as additional layers of media with complex refractive index placed adjacent to the PRBs. However, to eliminate the reflection from the box boundaries, but not to induce the parasitic reflection from the absorption medium, it seemed to be impossible by introduction of a physical media with different index from the adjacent media of the optical waveguide considering the fact that such reflection is caused by the index difference (including both real and imaginary parts). This is perhaps true if we limit ourselves to the electromagnetic waves governed by Maxwell equations in physical media. Thanks to the pioneer work of Berenger [45] , we now have an ideal absorber, referred to as the perfectly matched layer (PML), to fulfill our simulation model as illustrated in Figure 1.1 wherein the transverse plane is truncated by PMLs and PRBs. By analytically extending the Maxwell's equations into a modified form, Berenger discovered that it is possible to introduce an artificial layer for which the solutions of the modified Maxwell equations can match perfectly with the solutions of the original Maxwell's equations in a given adjacent medium.

In the complex mode model with PML and PRB, the absorption or the reflection of PML determines the performance of the model. With zero absorption (total reflection) the model turns into the box mode model. With infinite absorption (zero reflection) the model converges exactly to the open structure in the non-PML region, which however, is not implementable either numerically or analytically, for the singularities will appear at the boundaries. Normally, the convergence test is necessary in the complex mode theory, for

a certain problem, we need to gradually increase the PML absorption or reduce the reflection, until the results converge.

The complex modes can be categorized into three classes. The first category is complex guided modes. With the introduction of lossy media, even the guided modes will have a tiny imagery part in the modal indies, which are non-physical and should be neglected. Generally, the complex guided modes shows the same properties as guided modes in open structure model and the box mode model. The second class is the quasi-leaky modes. When the model converges with absorption of PML, quasi-leaky modes' modal indies will converge to the corresponding leaky modes' in the open structures. The coincidence can also be observed in terms of field distributions in the non-PML region. In the PML region, the quasi-leaky modes will stop growing exponentially, but start to decay to zero at the PRBs (for transverse electric fields or perpendicular magnetic fields). The feasibility to approximate the leaky modes shows the correctness of complex mode model. Besides, as the quasi-leaky modes are bounded, they can be treated in the same manner as other complex modes in terms of orthogonality and normalization. The last kind of modes are complex Berenger modes, or PML modes. They are the approximation to the radiation and evanescent modes in open structures. They have complex modal indies, and will decay along the propagation direction. In the transverse plane, field distributions are similar to the quasi-leaky modes. The difference between quasi-leaky modes and complex Berenger modes are that the latter are always dependent on the PML absorption, with no convergence occurred, while the former will converge as the PML absorption increases or the reflection decreases.

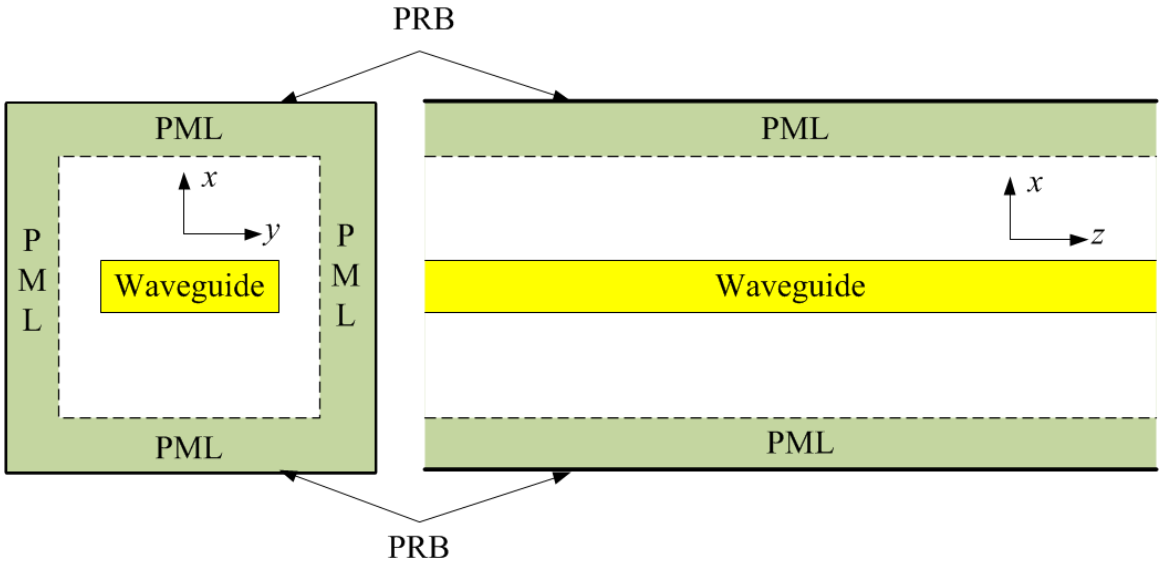

Figure 1.1 Computation model of perfectly reflecting boundaries(PRBs) with perfectly matched layers(PMLs).

1.3 Formulation for complex mode

The complex modes are governed by the modified Maxwell equations as mentioned before. The PML medium can also be regarded as an artificial anisotropic media with coordinate-varying constitutional parameters as first pointed by Chew et.al. [46]. The Maxwell's equations with anisotropic media can be written as

$$\nabla \cdot [\Lambda]\mathbf{E} = 0 \tag{1.1a}$$

$$\nabla \cdot [\Lambda]\mathbf{H} = 0 \tag{1.1b}$$

$$\nabla \times \mathbf{E} = -j\omega\mu_o [\Lambda]\mathbf{H} \tag{1.1c}$$

$$\nabla \times \mathbf{H} = j\omega\varepsilon_o\varepsilon_r [\Lambda]\mathbf{E} \tag{1.1d}$$

where the dielectric tensor for PML is given by

$$[\Lambda] = \begin{bmatrix} \frac{\alpha_y}{\alpha_x} & 0 & 0 \\ 0 & \frac{\alpha_x}{\alpha_y} & 0 \\ 0 & 0 & \alpha_x \alpha_y \end{bmatrix} \tag{1.2}$$

and PMLs are defined as the complex stretching parameters

$$\alpha_x = \kappa_x - j\frac{\sigma_x}{\omega\varepsilon} \tag{1.3a}$$

$$\alpha_y = \kappa_y - j\frac{\sigma_y}{\omega\varepsilon} \tag{1.3b}$$

The real part of the stretching parameter κ is introduced in Eq. (1.3) to control the attenuation for the evanescent waves, and the imaginary part represents the attenuation parameter for the traveling waves. Eq. (1.1) describes the material with absorption within the transverse plane, and we might only need the absorption for one dimension to solve for 1D complex modes. For the direction without absorption, we simply set the stretching parameters to be unity.

Mathematically, through stretched coordinates along directions of PML, we can transform Eq. (1.1) back to the Maxwell equations in isotropic medium, so that the existent model solvers could be adopted for the calculations for complex modes. Define a set of stretched complex coordinates along *x* and *y* as

$$\tilde{x} = \int_0^x \alpha_x(x)dx \tag{1.4a}$$

$$\tilde{y} = \int_0^x \alpha_y(y)dy \tag{1.4b}$$

we have

$$\frac{1}{\alpha_x}\frac{d}{dx}=\frac{d}{d\tilde{x}} \tag{1.5a}$$

$$\frac{1}{\alpha_y}\frac{d}{dy}=\frac{d}{d\tilde{y}} \tag{1.5b}$$

Therefore, the governing equations for the electric and magnetic fields are rewritten as

$$\tilde{\nabla}\cdot\mathbf{E}'=0 \tag{1.6a}$$

$$\tilde{\nabla}\cdot\mathbf{H}'=0 \tag{1.6b}$$

$$\tilde{\nabla}\times\mathbf{E}'=-j\omega\mu_o\mathbf{H}' \tag{1.6c}$$

$$\tilde{\nabla}\times\mathbf{H}'=j\omega\varepsilon_o\varepsilon_r\mathbf{E}' \tag{1.6d}$$

where $\tilde{\nabla}=(\frac{d}{d\tilde{x}},\frac{d}{d\tilde{y}},\frac{d}{dz})$, $\mathbf{E}'=\frac{E_x}{\alpha_x}\vec{\mathbf{x}}+\frac{E_y}{\alpha_y}\vec{\mathbf{y}}+E_z\vec{\mathbf{z}}$ and $\mathbf{H}'=\frac{H_x}{\alpha_x}\vec{\mathbf{x}}+\frac{H_y}{\alpha_y}\vec{\mathbf{y}}+H_z\vec{\mathbf{z}}$.

Eq.(1.6) can be further simplified into the eigen-problem regarding the transverse electric or magnetic field only. If we eliminate the electric field (because the magnetic fields are more convenient to deal with for its general continuity at all dielectric interfaces), then the formula involving magnetic fields only are

$$[\frac{\partial^2}{\partial\tilde{x}^2}+\varepsilon\frac{\partial}{\partial\tilde{y}}\frac{1}{\varepsilon}\frac{\partial}{\partial\tilde{y}}+(\omega^2\mu\varepsilon-\beta^2)]H_x'+[\frac{\partial^2}{\partial\tilde{x}\partial\tilde{y}}-\varepsilon\frac{\partial}{\partial\tilde{y}}\frac{1}{\varepsilon}\frac{\partial}{\partial\tilde{x}}]H_y'=0 \tag{1.7a}$$

$$[\varepsilon\frac{\partial}{\partial\tilde{x}}\frac{1}{\varepsilon}\frac{\partial}{\partial\tilde{x}}+\frac{\partial^2}{\partial\tilde{y}^2}+(\omega^2\mu\varepsilon-\beta^2)]H_y'+[\frac{\partial^2}{\partial\tilde{x}\partial\tilde{y}}-\varepsilon\frac{\partial}{\partial\tilde{x}}\frac{1}{\varepsilon}\frac{\partial}{\partial\tilde{y}}]H_x'=0 \tag{1.7b}$$

Here β is the propagation constant of mode. With the PRBs condition, discrete complex modes can be achieve as eigen-solutions from Eq. (1.7). The longitudinal magnetic field can be derived from transverse components following magnetic Gaussian law (Eq. (1.6b))

$$H_z = \frac{1}{j\beta}\left(\frac{\partial H_x^{'}}{\partial \tilde{x}} + \frac{\partial H_y^{'}}{\partial \tilde{y}}\right) \tag{1.8}$$

And the electric field then can be derived from the magnetic field from Ampere's law (Eq. (1.6d)) as:

$$E_x^{'} = \frac{1}{j\omega\varepsilon}\frac{\partial H_z}{\partial \tilde{y}} + \frac{\beta}{\omega\varepsilon}H_y^{'} \tag{1.9a}$$

$$E_y^{'} = -\frac{1}{j\omega\varepsilon}\frac{\partial H_z}{\partial \tilde{x}} - \frac{\beta}{\omega\varepsilon}H_x^{'} \tag{1.9b}$$

$$E_z = \frac{1}{j\omega\varepsilon}\left(\frac{\partial H_y^{'}}{\partial \tilde{x}} - \frac{\partial H_x^{'}}{\partial \tilde{y}}\right) \tag{1.9c}$$

The algorithms solving Eq. (1.7) for modal effective indies and field distributions are called mode solvers, among which the FDM and the FEM are two of the most popular approaches. The FDM gains its popularity owing to its simplicity and effectiveness [47]~[49]. On the other hand, the FEM is more adaptive for complex waveguide structures with irregular interfaces [50][51]. Besides the numerical methods based on discretization, a semi-analytical mode matching method is also available for mode solution [44], though the initial guess and complex plane root searching are troublesome, it will bring clearer physics insight about 2D modes and better modeling for the corner region, where the singularity exists.

1.4 Challenges for complex mode theory

Complex mode theory still faces several challenges in practical applications. First, the accuracy of the large number of high order modes required in modal analysis is difficult

to be guaranteed. Theoretically with small enough mesh step, we can always attain enough number of modes with required accuracy, however, this practice violates our original intention to pursue the mode theory – reduce the time and storage consumption compared with fully discretized algorithm FDTD. Under fixed mesh size, the accuracy of modes is decreasing with the growth of mode order. In the modal expansions, lots of high order modes are involved to provide higher spatial frequencies with faster oscillations in the transverse plane. The fast oscillation feature brings the error when mesh is not fine enough. In addition, the PML is another factor sabotaging the modes' accuracy. With the introduction of PML, field distributions will change and concentrate in the PML regions with higher amplitude and faster oscillation. To simulate the fields in PMLs accurately, smaller mesh size is needed, which is an effort we are not willing to take. At last, the 2D modes are normally much more difficult to attain and much less accurate compared with the 1D counterpart. It is obvious that with the same computation effort, the mesh in 2D is much loose than in 1D. Also, 2D modes are more complicated than 1D cases. In 2D, the full vector modes always have six components, and with singularities at the corner regions. In 1D, transverse electric/magmatic modes are decoupled with only three component for each, and there is no singular point. The mode solvers in 2D case are also less developed compared with 1D cases. In 1D case, the analytical solution exists from transfer matrix method with smooth transient process for complex mode searching[52]. And the FDM is much more advanced with higher order accuracy differential operators[53][54]. In 2D we do not have those techniques to enhance the accuracy .

The second challenge is, as mode accuracy is hard to guaranteed for high order modes, the modal orthogonality which is sensitive to the accuracy of modes fails. In the conventional formulation, the mode orthogonality is adopted and essential in modal expansion. The third challenge is the increasing number of modes required in modal expansion when PMLs are introduced. The introduction of PMLs will decrease the expansion efficiency of modes, which means even for the same target field, with stronger absorption of PML, more modes are needed in modal expansion, though higher accuracy is the trade-off prize.

The inhomogeneous distribution of modes in asymmetric structures may also lead to challenge in terms of the tedious process of mode selection. The complex Berenger modes will be further classified due to the different substrate and cladding around the guiding structure. Different kinds of Berenger modes may have field concentrations in different PML layers. Normally in the modal expansion, only parts of the modes may have the largest overlap integral with the excited waves. To increase the expansion efficiency and stability, mode selection is necessary.

1.5 Main contribution of the thesis

Aiming at the challenges discussed above, the main contributions of this thesis will be illustrated as below:

Compared with guided modes, the Berenger modes are less investigated. In this thesis, I showed the analytical investigation on the high order Berenger modes. The asymptotic solutions will be derived, and the modes' behavior will be related to the

weighted optical path distance, which can be adjusted through customized PML design. Finally different types of complex Berenger modes in the asymmetric structure could degenerate into one, so as to avoid the mode selection. Besides, the field distributions of high order complex Berenger modes will be modified to be more symmetric, which may enhance the modal expansion efficiency.

An improved mode matching method is proposed, which is derived from the optimization methodology, other than from the problematic orthogonality as in the conventional MMM. Instead of assuming the tangential field continuity at the interface as a premise, we take the finite number of modes as the new presumption, and then try to minimize the mismatch error at the interfaces. Consequently, we can achieve an algorithm with faster convergence speed, and smaller reliance on the modal orthogonality. Silicon channel waveguide facet, right angle bending, silicon-germanium photo-detector structure are studied to show the effectiveness and feasibility of the aforementioned improvement.

With the fulfilled complex mode theory, several passive and active designs are simulated and realized in this thesis. As mentioned at the very beginning, functional layer embedded with silicon channel waveguide, is a common mechanism to introduce phase and/or loss modulations into the traditional silicon photonics waveguides. We insert a thin ribbon of metallic material into the semiconductor channel waveguide, and proposed a hybrid plasmonic-photonic nano-ribbon waveguide, whose fundamental guided mode is a novel TM hybrid slot/surface-plasmon-polariton (SPP) mode. The newly proposed waveguide is a combination of the photonic slot and the plasmonic SPP waveguide, with merits of both long propagation distance and high field confinement. We applied the

complex mode theory with PML and PRB instead of the simple box truncation for this investigation, because we explored the cases when the size of waveguide shrank to the cut-off condition, under which condition the guided modes became very leaky and the field distributions expanded into a large area. With the PMLs, a much smaller simulation window could be utilized to enhance the simulation accuracy and efficiency.

A layer of phase changing material – $Ge_2Sb_2Te_5$ (GST) was incorporated into the Si channel waveguide. Through the modal analysis, distinguished phase and/or loss change for the fundamental TE/TM mode are found. This waveguide could be employed in electro-optical phase and/or loss modulation in several forms, including a three- and four-waveguides directional couplers which could be analyzed and designed through the improved MMM.

The above researches have resulted in the following publications:

Journal papers:

1.H. Liang, R. Soref, J. Mu, X. Li, and W. P. Huang "Electro-optical Phase-change 2x2 Switching Using Three- and Four- Waveguide Directional Couplers", Applied Optics 54 (19), 5897, 2015.

2.H. Liang, R. Soref, J. Mu, A. Majumdar, X. Li, and W. P. Huang "Simulation of Silicon-on-insulator Channel-waveguide Electro-optical 2 x 2 Switches and 1 x 1 Modulators Using a Ge2Sb2Te5 Self-holding Layer", IEEE Journal of Lightwave Technology, 33, 1805-1813 (2015).

3.R. Soref, J. Hendrickson, H. Liang, A. Majumdar, J. Mu, X. Li, W.P. Huang, "Electro-optical switching at 1550 nm using a two-state GeSe phase-change material", Optics Express 23 (2), 1536-1546, 2015.

4.H. Liang, J. Mu, R. Soref, X. Li, and W. P. Huang, “An optical mode-matching method with improved accuracy and efficiency”, IEEE Journal of Quantum Electronics 51 (2), 6100108, 2015

5.H. Liang, R. Soref, J. Mu, X. Li, W. P. Huang, "Long range mid-infrared propagation in Si and Ge hybrid plasmonic-photonic nano-ribbon waveguides", Optics Express 22 (23), 28489-28499,2014

6.H. Liang, J. Mu, X. Li, and W.P. Huang, “Insights into complex Berenger modes: a view from the weighted optical path distance perspective”, Optics Letters 39(9), 2811-2814, 2014

7.J. Mu, H. Liang, X. Li, B. Xu, and W. P. Huang, “Vector Mode Analysis of Optical Waveguides by Quadratic Spline Collocation Method,” Progress In Electromagnetics Research M. 27, 97-107,2012

Conference papers:

8.H. Liang, J. Mu, X. Li, and W. P. Huang, “Improved Complex Mode Matching Method for Optical Waveguides Analysis”, in Integrated Photonics Research, Silicon and Nanophotonics, pp. IT1A-5. Optical Society of America, 2014.

9.H. Liang, J. Mu, X. Li, and W. P. Huang, “An Investigation into the Phase Angles of High-Order Berenger Modes”, In Integrated Photonics Research, Silicon and Nanophotonics, pp. JT3A-35. Optical Society of America, 2014.

10.J. Mu, L. Han, H. Liang, W. P. Huang, "Circuit Model Analysis of Radiation Coupling", In Photonics in Switching, pp. JT3A-34. Optical Society of America, 2014.

11.H. Liang, J. Mu, X. Li, and W. P. Huang, "Roles of High Order Bend Modes in Optical Wave Coupling", in Photonics North 2014, pp. 928813-928813, International Society for Optics and Photonics.

Chapter 2.

Insights into High Order Complex Berenger Modes

2.1 Introduction

When we come to the problems involving scattering, evanescent coupling, or leaky structures, the radiation effect will play an important role. In the complex mode theory, the radiation field is represented by discrete complex modes, especially the complex Berenger modes. In the chapter, we will show some properties of high order Berenger modes, and some techniques to modify the Berenger modes to achieve high simulation efficiency in modal expansion of radiation field.

Radiation coupling plays an important role in photonics device design and optical waveguide excitations [55]~[59]. One of the most difficult problems in radiation coupling applications is how to represent a continuum of infinite radiation modes. This challenge

has been solved recently by a computation model facilitated by PMLs with PRB conditions. The aforementioned computation model provided solutions for two essential difficulties of radiation modes: normalization and the continuous mode spectrum [34][60]~[63].

The complete mode spectrum of an open waveguide structure can be categorized into three types: guided modes with real modal effective indices, continuous radiation modes with real modal effective indices, and evanescent modes with pure imaginary modal effective indices [38][39]. Leaky modes, which are physically non-existing solutions of Maxwell equations governing the light propagation in an open waveguide structure, are also utilized to represent radiation loss under certain constraints [40]~[43]. Within the computation model with PML and PRB, leaky modes, radiation modes, and evanescent modes are mapped to a set of complex modes which preserves normal modes properties such as normalization and orthogonality [60][64]~[68]. Consequently, the radiation modes and evanescent modes can be dealt with in the same fashion as guided modes, so that the computation effort is greatly saved [67]~[70].

For waveguides with asymmetric refractive index distribution profile (substrate material differs from cladding material), such as ridge waveguides, silicon wires, etc. , higher order radiation modes can be further be categorized into two types in terms of their electromagnetic field distribution, namely: substrate radiation modes, and cladding radiation modes [71]. Correspondingly, within the framework of PML and PRB computation model, higher order complex Berenger modes split into two branches with different phase angles. Those higher order modes are trouble makers in mode expansion.

Since the overlapping integral among guided modes and those complex modes are small, naturally two issues arise: 1) coefficient matrix becomes very singular and convergence problems appear; 2) more modes are required to represent the total field precisely thus computation effort increases. In this chapter, we demonstrated that the aforementioned two issues can be overcome by adjusting the phase angle of high order Berenger modes.

2.2 Asymptotic solutions of high order complex Berenger modes

Without losing generality, we consider a multiplayer waveguide structure shown in Figure 2.1. This multilayer waveguide consists of *N* layers, PMLs are used to simulate the open waveguide structure, and PRBs are utilized to truncate the computation window.

The filed inside the *i*-th layer of this multilayer waveguide structure is given by [52][72]

$$\phi_m(x) = a_i^+ e^{-j\kappa_i(x-x_i)} + a_i^- e^{j\kappa_i(x-x_i)}, \kappa_i = k_0\sqrt{n_i^2 - n_{eff,m}^2} \tag{2.1}$$

Here $\phi_m(x)$ indicates the *m*-th transverse electric filed E_{my} for TE modes or the *m*-th transverse magnetic field H_{my} for TM modes, k_0 the wave number in vacuum, and $n_{eff,m}$ the modal effective index of the m-th mode. a_i^+ and a_i^- are the amplitude coefficients of the forward (+) and backward (-) waves at the incident interface of *i*-th layer, respectively. b_i^+ and b_i^- are the amplitude coefficients of the forward (+) and

backward (-) waves at the exit interface of *i*-th layer, respectively. The relation between $a_i^{\pm}$ and $b_i^{\pm}$ is given by

$$B_i = P_i A_i \tag{2.2}$$

Here $A_i = [a_i^+, a_i^-]^T$, $B_i = [b_i^+, b_i^-]^T$ and P_i is the propagation matrix for layer *i* as

$$P_i = \begin{bmatrix} e^{-j\kappa_i d_i} & 0 \\ 0 & e^{j\kappa_i d_i} \end{bmatrix} \tag{2.3}$$

with $d_i = x_{i+1} - x$, denoting the thickness of *i*-th layer.

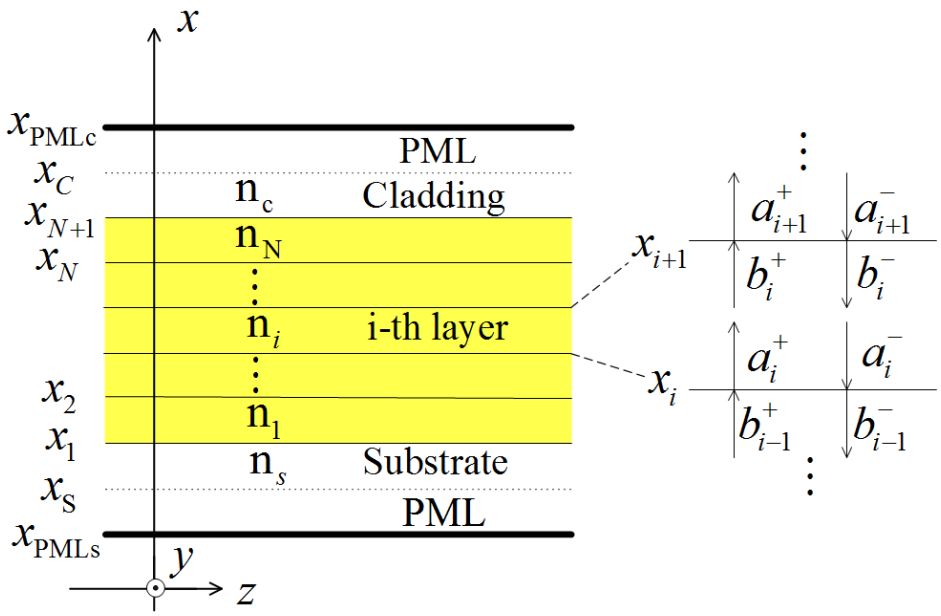

Figure 2.1 A multilayer waveguide structure with semi-infinite substrate and cladding truncated by PML and PRB. a_i^+ and a_i^- are amplitude coefficients of the forward (+) and backward (-) waves at the incident interface of *i*-th layer, respectively. b_i^+ and b_i^- are the amplitude coefficients of the forward (+) and backward (-) waves at the exit interface of layer, respectively.

The boundary condition is given by

$$D_i B_i = D_{i+1} A_{i+1} \tag{2.4}$$

with $D_i = \begin{bmatrix} 1 & 1 \\ \eta_i & -\eta_i \end{bmatrix}$ and $\eta_i = \begin{cases} \kappa_i & \text{for TE} \\ \kappa_i / n_i^2, & \text{for TM} \end{cases}$.

With Eq.(2.3) and Eq.(2.4), we can easily find the transfer matrix T linking A_{N+1} and B_0. Here the "s" and "c" in Figure 2.1 are replaced with subscripts " 0" and "N+1 ".

$$A_{N+1} = D_{N+1}^{-1} \prod_{i=N}^{1} (D_i P_i D_i^{-1}) D_0 B_0 = T B_0 \tag{2.5}$$

$D_i P_i D_i^{-1}$ can be further expressed as

$$D_i P_i D_i^{-1} = \frac{1}{\eta_i} \begin{bmatrix} \eta_i \cos(\kappa_i d_i) & -j \sin(\kappa_i d_i) \\ -j\eta_i^2 \sin(\kappa_i d_i) & \eta_i \cos(\kappa_i d_i) \end{bmatrix} \tag{2.6}$$

For simplicity, we express the modal effective index of m-th Berenger modes as $n_{eff,m} = | n_{eff,m} | e^{-j\theta_m}$, where θ_m is from 0 to $\frac{\pi}{2}$. As the order increases, we can apply the approximations in [66]:

$$\lim_{m \to \infty} | n_{eff,m} | = \infty, \lim_{m \to \infty} \theta_m = \theta_0 \tag{2.7}$$

Here θ_0 is a constant ($\theta_0 \in (0, \pi/2)$). From Eq.(2.7), further approximation can be made for in Eq. (2.6) as

$$\kappa_i d_i = k_0 | n_{eff,m} d_i | e^{j(\frac{\pi}{2} - \theta_m)} \sqrt{1 - n_i^2 / n_{eff,m}^2} \approx k_0 | n_{eff,m} d_i | [\sin(\theta_0) + j \cos(\theta_0)] \tag{2.8}$$

It should be noted that there are always two possible roots when finding the square roots in Eq.(2.1). We discarded the roots with negative real parts since those roots are conflicted with propagation direction definition in Eq. (2.1).

As $Im(\kappa_i d_i) \to +\infty$ when $m \to \infty$, we can reasonably assume that $\cos(\kappa_i d_i) = \frac{1}{2} e^{-j\kappa_i d_i}$ and $\sin(\kappa_i d_i) = j\frac{1}{2} e^{-j\kappa_i d_i}$ for high order Berenger modes. Eq. (2.6) can be simplified as:

$$D_i P_i D_i^{-1} = \frac{e^{-j\kappa_i d_i}}{2\eta_i} \begin{bmatrix} 1 \\ \eta_i \end{bmatrix} \begin{bmatrix} \eta_i & 1 \end{bmatrix} \tag{2.9}$$

Using Eq.(2.9) into Eq. (2.5), we have the explicit expression of *T* as:

$$T = e^{j\sum_{i=1}^{N} \kappa_i d_i} \prod_{i=0}^{N} \frac{\eta_{i+1} + \eta_i}{2\eta_{i+1}} \begin{bmatrix} 1 \\ \dfrac{\eta_{N+1} - \eta_N}{\eta_{N+1} + \eta_N} \end{bmatrix} \begin{bmatrix} 1 & \dfrac{\eta_1 - \eta_0}{\eta_1 + \eta_0} \end{bmatrix} \tag{2.10}$$

It is noted that this expression is only valid for the high order Berenger modes, which satisfy the assumptions in Eq.(2.7).

The field in the cladding and substrate (including PML region) is

$$\phi(x) = \begin{cases} a_{N+1}^{+} e^{-j\kappa_{N+1}(\tilde{x}(x) - \tilde{x}(x_{N+1}))} + a_{N+1}^{-} e^{j\kappa_{N+1}(\tilde{x}(x) - \tilde{x}(x_{N+1}))}, & x_{N+1} < x < x_{PMLc} \\ b_0^{+} e^{-j\kappa_0(\tilde{x}(x) - \tilde{x}(x_1))} + b_0^{-} e^{j\kappa_0(\tilde{x}(x) - \tilde{x}(x_1))}, & x_{PMLs} < x < x_1 \end{cases} \tag{2.11}$$

where $\tilde{x}$ is the complex coordinate in [46][73] which is also expressed by Eq.(1.4a). $\alpha(x)$ here is the coordinate stretching factor, and can be expressed in terms of PML's reflection *R* and thickness along with the structure parameters as in [67]

$$\alpha(x) = \begin{cases} 1 - j\dfrac{3\lambda}{4\pi n} \dfrac{\rho^2}{d_{PML}^3} \ln\left(\dfrac{1}{R}\right) & \text{in PML} \\ 1 & \text{otherwise} \end{cases} \tag{2.12}$$

where ρ is the distance from PML starting interface. Under the complex coordinate, the equivalent complex thicknesses of cladding and substrate are given by

$$\tilde{d}_{s,c} = d_{s,c} - j\frac{\lambda}{4\pi n_{s,c}} \ln\frac{1}{R_{s,c}} = |\tilde{d}_{s,c}| e^{-j\delta_{s,c}} \tag{2.13}$$

Boundary conditions for PRB are given:

$$\phi(x_{PMLc}) = a_{N+1}^{+} e^{-j\kappa_{N+1}\tilde{d}_c} + a_{N+1}^{-} e^{j\kappa_{N+1}\tilde{d}_c} = 0 \tag{2.14a}$$

$$\phi(x_{PMLs}) = b_0^{+} e^{j\kappa_0\tilde{d}_s} + b_0^{-} e^{-j\kappa_0\tilde{d}_s} = 0 \tag{2.14b}$$

Using Eq.(2.5), Eq.(2.10) and Eq.(2.14), we can obtain a characteristic equation for high order Berenger modes as

$$(\eta_1 + j\eta_0 cot(\kappa_0\tilde{d}_s))(\eta_N + j\eta_{N+1} cot(\kappa_{N+1}\tilde{d}_c)) = 0 \tag{2.15}$$

which decouples to two separate equations as

$$\eta_1 + j\eta_0 cot(\kappa_0\tilde{d}_s) = 0 \tag{2.16a}$$

$$\eta_N + j\eta_{N+1} cot(\kappa_{N+1}\tilde{d}_c) = 0 \tag{2.16b}$$

Eq.(2.16) describes the characteristic equations for S-Berenger modes and C-Berenger modes, respectively. For S-Berenger modes, consider $\kappa_0\tilde{d}_s$ in Eq. (2.16a) under the assumption in Eq. (2.7) in the same way as for Eq.(2.8)

$$\kappa_0\tilde{d}_s \approx k_0 \,|\, n_{eff,m}\tilde{d}_s \,|\, e^{-j(\theta_m - \frac{\pi}{2} + \delta_s)} \tag{2.17}$$

For high order S-Berenger modes, θ_0 approaches $\pi/2 - \delta_s$ in order to bear discrete modes to satisfy Eq. (2.16a). Thus we have

$$\tan\theta_0^s = \cot\delta_s = -2k_0 \frac{\varphi_s}{\ln(R_s)} \tag{2.18}$$

where $\varphi_s = n_s d_s$ is the optical path distance in substrate (including the PML area).

Similarly for C-Berenger,

$$\tan\theta_0^c = \cot\delta_c = -2k_0\frac{\varphi_c}{\ln(R_c)} \tag{2.19}$$

where $\varphi_c = n_c d_c$ is the optical path distance in cladding.

2.3 Weighed optical path distance

From Eq.(2.18) and Eq.(2.19), it is clear that S-Berenger and C-Berenger modes will have the same phase angle if

$$\frac{\varphi_s}{\ln(R_s)} = \frac{\varphi_c}{\ln(R_c)} \tag{2.20}$$

Eq.(2.20) shows that, there are two key factors which affect the phase angle of Berenger modes, namely, the reflection coefficients at PRB (determine the absorption strength), and the optical path distance φ . Since the computation window is usually preset in practice, Eq.(2.20) indicates that the complex Berenger modes with the same phase angle can be obtained by weighting the optical path distance with PML reflection coefficients.

2.4 Integrated Germanium photo-detector structure

We take an integrated Germanium photo-detector structure as an example[59]. The TE light is launched from a silicon nitride (SiN) slab waveguide and is coupled into a Germanium photo-detector (Figure 2.2). The refractive indices of SiN, silicon (Si), Ge, and silicon dioxide (SiO_2) are given as 2.2, 3.47, 4.1, and 1.44, respectively. The thicknesses of SiN slab, and Si buffer layer are 400 nm and 200 nm, respectively. The

cladding region (SiO_2) and substrate region (Ge) are set to 500 nm and they are enclosed with 2 μm PMLs as artificial absorbing media. The operating wavelength is1550 nm.

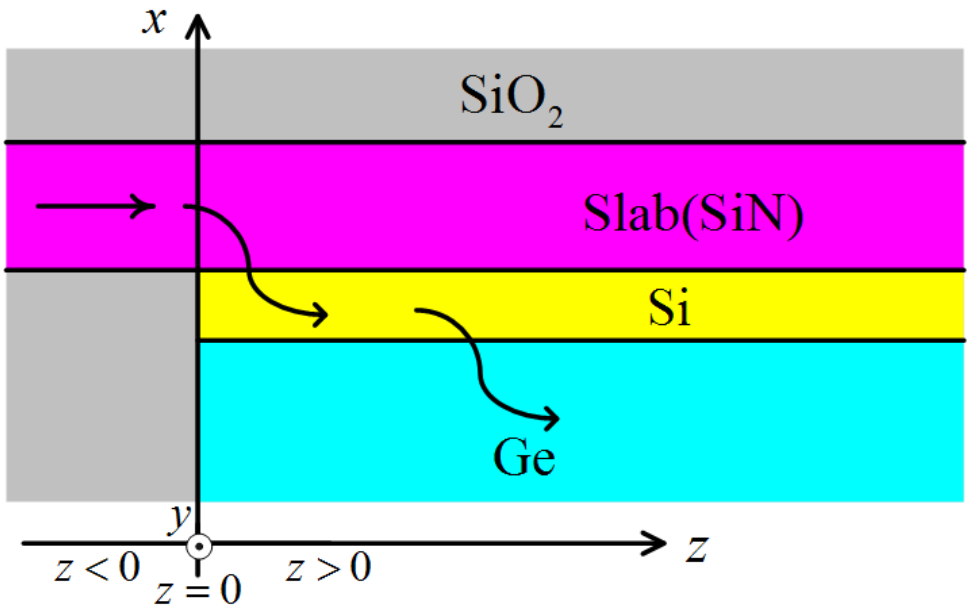

Figure 2.2 An integrated Germanium photo-detector [59]. TE light is launched from a silicon nitride (SiN) slab waveguide along +z direction and is coupled into a Germanium photo-detector.

The multilayer waveguide structure in the region for $z>0$ is leaky so that the evanescent coupling occurs. We utilized a FDM with incorporation of a high order boundary condition [54] to find the mode spectrum. For simplicity in the comparison, we refer the results from unadjusted optical path distances to "UOPD", and the results from weighted optical path distances to "WOPD". In the UOPD case, we set the PML reflection coefficients in cladding and substrate both to 0.005. In the WOPD case, however, we set the reflection coefficient in cladding to 0.005, whereas in substrate to 2.8 x 10^{-7}, to satisfy Eq.(2.20).

As shown in Figure 2.3(a), for UOPD, we clearly observe two different branches of PML modes, corresponding to C-Berenger modes and S-Berenger modes, with asymptotic phase angle 79.7° and 86.4° respectively. For WOPD in Figure 2.3 (b), however, the phase angles of C-Berenger modes and S-Berenger modes converge as the increase of the mode order. We traced the field patterns of the 81st (S-Berenger) and 82nd (C-Berenger) mode from both WOPD and UOPD cases. Results in Figure 2.3 (c) and Figure 2.3 (d) show that, with WOPD, more electromagnetic field is concentrated inside the central region. Here we want to emphasize that, within the framework of PMLs and PRB model, modal distributions of higher order complex Berenger modes varies with PMLs parameters. From this point of view, mode set from both WOPD and UOPD can represent the total field precisely if we use a large number of complex Berenger modes.

With the mode sets obtained from WOPD and UOPD, we consider an excitation problem described in Figure 2.2. The light is launched from a SiN slab waveguide ($z<0$) to Ge photodetector ($z>0$). SiN slab waveguide ($z<0$) is a well-defined waveguide structure so we set PML reflection coefficients in substrate and cladding regions to 0.05. We use a complex MMM to evaluate the mode set obtained from WPOD and UOPD, and use the result obtained by the FDTD method as the benchmark. We define relative field error to evaluate the performance. The relative field error is given by

$$\Delta F(N) = \frac{\int_x |E_{y,z=0,MMM}(N) - E_{y,z=0,FDTD}|\,dx}{\int_x |E_{excitation}|\,dx} \tag{2.21}$$

Here the field error ΔF defines the deviation of the total electric field obtained by MMM from that obtained by FDTD at $z=0$. Simulation data shown in Figure 2.4 reveal that: 1)

the result from MMM with the mode set in the UOPD case fluctuates with the total number of modes involved more significantly; 2) MMM with the mode set in the WOPD case converges more rapidly. The improvements can be explained by the fact that the SiN slab structure ($z<0$) is a symmetric structure, so the corresponding field pattern can be matched well by fewer symmetric modes from WOPD than asymmetric modes from UOPD.

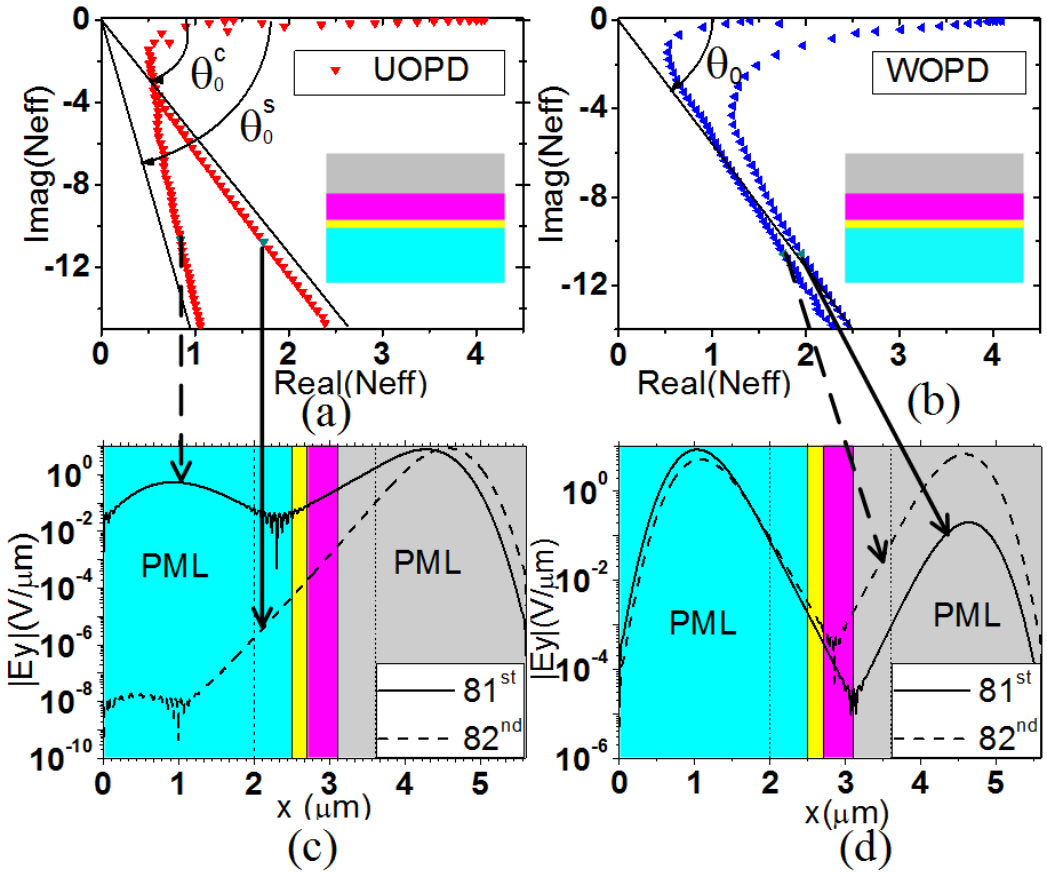

Figure 2.3 Modal spectrum of SiN slab on Ge. a) Modal spectrum using UOPD, phase angles of C-Berenger modes differs significantly from that of S-Berenger modes. b) Modal spectrum using WOPD, phase angles of C-Berenger modes and S-Berenger modes

converge. c) Electric field patterns of the 81-st and 82-nd modes using UOPD. d) Electric field patterns of the 81-st and 82-nd modes using WOPD.

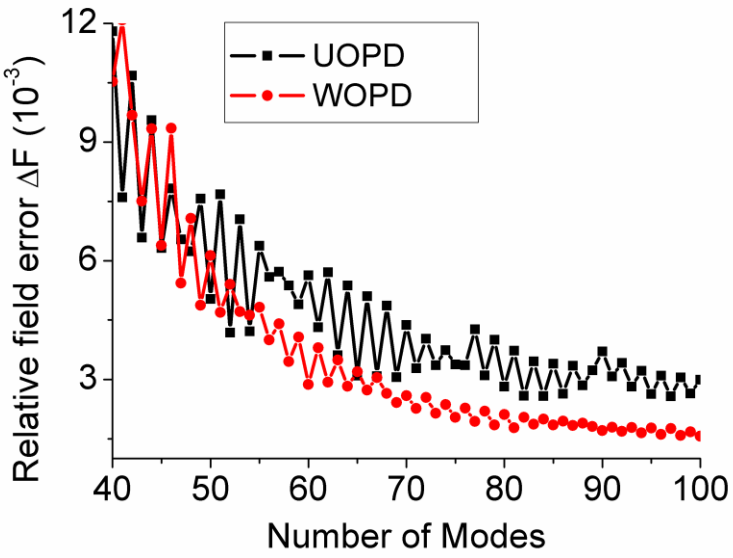

Figure 2.4 The relative field errors as functions of the total number of modes involved in MMM. MMM in the WOPD scheme shows smaller relative field error and fluctuations. Red dot: results from MMM with WOPD, Black Square: results from MMM with UOPD.

2.5 Summary

In summary, we theoretically show that, Berenger modes split into two branches, namely, cladding Berenger modes (C-Berenger modes), and substrate Berenger modes (S-Berenger modes), which are corresponding to cladding radiation modes and substrate radiation modes in open waveguide structures. Moreover, we derived a simple yet insightful condition which discloses the relation between high order Berenger modes and the PML parameters as well as optical path distance in cladding and substrate regions.

Further, we propose a computation model based on a weighted optical path distances which is easy for implementation for calculating high order complex Berenger modes. Using this model, the phase angles of S-Berenger modes and C-Berenger modes can be adjusted to the same, which is meaningful and significant: modal field patterns become symmetric, and fewer modes are needed to represent the total field which greatly simplifies the mode expansion computation in practice. We applied mode expansion method together with the proposed weighted optical path distance approach to investigate the light excitation problem in a Ge photo-detector. Simulation results show that the proposed method has merits of simple implementation, robustness, and improved accuracy.

Chapter 3.

An Optical Mode-matching Method with Improved Accuracy and Efficiency

3.1 Introduction

Mode matching method (MMM), or known as mode expansion method provides a solution to handle scattering problem analytically. The conventional mode-matching method (CMMM) is an accurate and efficient frequency-domain simulation scheme especially for optical waveguide propagation problems. In that MMM, the optical waveguide structure is divided into multiple *z*-invariant segments (*z* is the propagation direction) [74]~[77]; then the eigen-modes of each *z*-invariant segment are calculated by mode solvers. Knowing the complete set of the eigen-modes of each segment, we can expand an arbitrary electromagnetic field of each segment in terms of eigen-modes. By applying the tangential field-component continuity condition as well as mode

orthogonality, we obtain a scattering matrix which describes the transmission and reflection relation between the inputs and output ports.

Early development of the CMMM experienced the challenge of handling the continuous spectrum of radiation modes and the evanescent modes of an open waveguide structure [77]. The leaky mode approximation has therefore been proposed to circumvent the complexity of including radiation and evanescent modes. Leaky modes, on the other hand, are unbounded and grow exponentially in the waveguide cladding and substrate; so they cannot be treated uniformly in terms of normalization and orthogonality as are guided modes [40],[42]. Recent progress in the CMMM is attained in the framework of PML terminated by the PRB condition [34][60]~[63]. There, the continuous spectrum of radiation modes and evanescent modes are discretized into discrete complex modes (Berenger modes) which possess the characteristics of normalization and orthogonality, so that guided modes and radiation modes can be treated in a united fashion[66][67]. The CMMM based on complex modes has been proved to be an efficient and accurate method in its application as treating waveguide facets [78], waveguide discontinuities [79], and Bragg gratings[70],[80]. Self- consistency of this complex CMMM has been proven by power conservation, and it has been shown that complex CMMM is capable of simulating the coupling of radiation waves perpendicular to the waveguide axis, for instance, in waveguide crossings, T-junctions, and in corner- and cavity-assisted T-junctions [81]. We also noticed the progress of alternative implementations of MMM, for instance, the quadric directional eigen-mode expansion method based on non-orthogonal modes is demonstrated to be an effective and accurate tool for the analysis of off-axis wave

propagations [82]. A vertical mode expansion method, in which one-dimensional modes along the propagation direction are used to match the two-dimensional boundary condition, reduces the original three-dimensional problem to a two-dimensional problem with fairly high accuracy [83]. Recently, MMM combined with full vectorial three-dimensional whispering gallery modes have been employed to study the radiation coupling involving multi-mode microcavity , which is important and promising in SOI platform simulation [84],[85]. Besides, based on the concepts of a generalized CMMM, a rigorous and efficient circuit model has been proposed and demonstrated recently [37].

The fundamental assumptions of CMMM are that the mode set is complete and that the tangential-field continuity condition is satisfied. Those assumptions imply that an infinite number of complex modes are required in the formulation. However, in practice, the number of modes is limited by the computation expense; thus in practice the tangential boundary continuity condition fails, leading to field-mismatch errors - the difference of fields restored by the modes from two structures next to the interface. The field mismatch error could be significantly large if only a few modes are employed, or if high-index-contrast waveguide structures, are investigated. The second scenario arises frequently nowadays for dense silicon photonic-device integration applications wherein the strong radiation effects have to be understood.

In this work, we have revisited the details of MMM implementation with an eye towards reducing the field mismatch errors arising from unsatisfied tangential boundary conditions. Our investigation has revealed that the CMMM can be improved by reconstructing the auxiliary coefficient matrix. We have shown that this new formulation

yields many merits over CMMM such as: a smaller field mismatch error, faster convergence speed and less computation effort. In this work, the reformulated CMMM is referred to as the improved MMM or IMMM, and CMMM is understood to include mode orthogonality.

This chapter is organized as follows: First we review the basic equations and formulations of the CMMM approach. Next we arrive at the critical case of limited number N of modes that leads to practical problems. Then we derive our IMMM approach with an improved transfer matrix. This leads to a new accuracy criterion that will minimize field-mismatch error. Finally we show the value and competence of IMMM by numerical evaluation of errors in three waveguide cases: a truncated SOI channel waveguide, a 90^o bend and a 1D Ge-photo-detector structure. For all the examples, we present strong evidence that a significant improvement in accuracy is attained along with enhanced computational efficiency. With the assistance of IMMM, the high order bending modes are investigated in optical coupling.

3.2 Review of the CMMM formulation

Here we review the formulation of the prior-art MMM to highlight the issues in applying it. Considering the basic scenario in MMM, in which light propagates along a straight waveguide with a discontinuity at $z=z_0$ (z is the propagation direction and $z_0>0$) as shown in Figure 3.1 where light is launched from the left at $z=0$. The interface of discontinuity is located at $z=z_0$, partitioning the waveguide into two z-invariant structures A and B. We calculate the modes in the framework of PMLs and PRBs for both structures, in which all

the radiation modes at $z=z_0$ are discretized into a set of complex modes. Generally, structures *A* and *B* are homogeneous in the *z*-direction and the transverse modes in the *x*-*y* plane are calculated here. The transverse electric and magnetic fields are both continuous at the interface, and can be expanded with different sets of complex modes from structure A and B if infinite number of modes is available [78]:

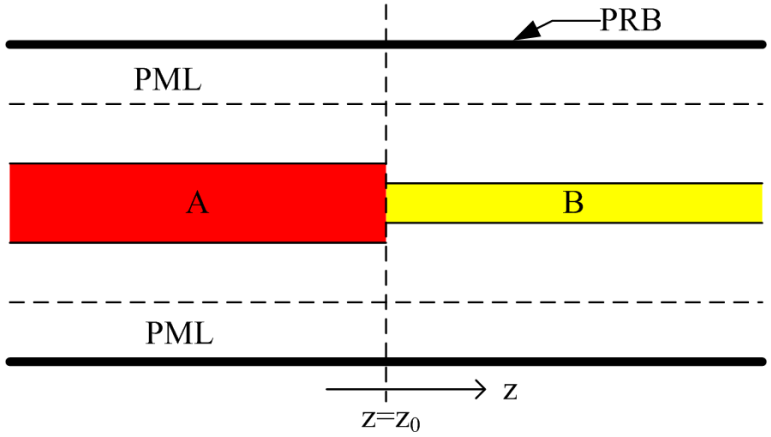

Figure 3.1 Straight waveguide with a discontinuity at $z=z_0$ in the framework of PMLs and PRBs. Light is propagating along +z direction, and the waveguide can be partitioned into two *z*-invariant structures *A* and *B*.

$$\sum_{i=1}^{+\infty}(a_i^+ + a_i^-)\mathbf{e}_{ti}^A(\mathbf{t}) = \sum_{i=1}^{+\infty}(b_i^+ + b_i^-)\mathbf{e}_{ti}^B(\mathbf{t}) \tag{3.1a}$$

$$\sum_{i=1}^{+\infty}(a_i^+ - a_i^-)\mathbf{h}_{ti}^A(\mathbf{t}) = \sum_{i=1}^{+\infty}(b_i^+ - b_i^-)\mathbf{h}_{ti}^B(\mathbf{t}) \tag{3.1b}$$

Here, $\mathbf{e}_t$ and $\mathbf{h}_t$ are the mode's transverse electric and magnetic fields respectively, $\mathbf{t}$ denotes the position in the transverse plane, the subscripts i denotes the mode index, and the superscripts denotes which structure the mode belongs. $a_i^{\pm}$ and $b_i^{\pm}$ are the amplitude

coefficients of the *i*-th forward(+) and backward(-) modes for structure *A* and *B* respectively.

Normally, we truncate the mode set by taking *N* modes, and then assume that the equality relation in Eq. (3.1) still holds. Then in matrix form Eq. (3.1) can be expressed as:

$$\begin{bmatrix} \mathbf{E}_t^{A,N}(\mathbf{t}) & \mathbf{E}_t^{A,N}(\mathbf{t}) \\ \mathbf{H}_t^{A,N}(\mathbf{t}) & -\mathbf{H}_t^{A,N}(\mathbf{t}) \end{bmatrix} \cdot \mathbf{A} = \begin{bmatrix} \mathbf{E}_t^{B,N}(\mathbf{t}) & \mathbf{E}_t^{B,N}(\mathbf{t}) \\ \mathbf{H}_t^{B,N}(\mathbf{t}) & -\mathbf{H}_t^{B,N}(\mathbf{t}) \end{bmatrix} \cdot \mathbf{B} \tag{3.2}$$

where $\mathbf{E}_t^N(\mathbf{t}) = [\mathbf{e}_{t1}(\mathbf{t}), \mathbf{e}_{t2}(\mathbf{t}), \cdots, \mathbf{e}_{tN}(\mathbf{t})]$, and $\mathbf{H}_t^N(\mathbf{t})$ is defined in the same manner. Besides, coefficient vector $\mathbf{A}$ is defined as $\mathbf{A} = [a_1^+, a_2^+, \cdots, a_N^+, a_1^-, a_2^-, \cdots, a_N^-]^T$ and $\mathbf{B}$ is following the same manner.

Through the expansion of the input field, half of the coefficients can be determined, and the key issue left for CMMM is to derive the transfer matrix or scattering matrix to relate the known and unknown coefficients. The transfer matrix $\mathbf{T}$ is defined as $\mathbf{A} = \mathbf{T} \cdot \mathbf{B}$, and one general expression is:

$$\mathbf{T} = \left(\iint_S \mathbf{M}(\mathbf{t}) \cdot \begin{bmatrix} \mathbf{E}_t^{A,N}(\mathbf{t}) & \mathbf{E}_t^{A,N}(\mathbf{t}) \\ \mathbf{H}_t^{A,N}(\mathbf{t}) & -\mathbf{H}_t^{A,N}(\mathbf{t}) \end{bmatrix} dS \right)^{-1} \cdot \left(\iint_S \mathbf{M}(\mathbf{t}) \cdot \begin{bmatrix} \mathbf{E}_t^{B,N}(\mathbf{t}) & \mathbf{E}_t^{B,N}(\mathbf{t}) \\ \mathbf{H}_t^{B,N}(\mathbf{t}) & -\mathbf{H}_t^{B,N}(\mathbf{t}) \end{bmatrix} dS \right) \tag{3.3}$$

Here $\mathbf{M}$ is an arbitrary *N*-by-2 matrix making the item in the right side's first parentheses invertible, and "S" denotes the transverse plane. To obtain Eq. (3.3) from Eq. (3.2), firstly both sides of Eq. (3.2) are left-multiplied by **M**, and then for each item in the matrix we take the overlap integral in the transverse plane. Then the following steps are taken to rewrite the equation because the definition of $\mathbf{T}$ is straightforward. Normally, $\mathbf{M}$ is constructed through the mode orthogonality, which is given by [67].

$$\iint_S \mathbf{h}_{ti}(\mathbf{t}) \times \mathbf{e}_{tj}(\mathbf{t}) \cdot \mathbf{z} dS = N_i \delta_{i,j},\ j = 1, 2, \cdots \tag{3.4}$$

Here $\delta_{i,j}$ is the Dirac function, and N_i is the normalization coefficient for the *i*-th mode. $\mathbf{z}$ is the unit vector along +*z*. The formula above can also be rewritten in matrix form as:

$$\iint_S (\mathbf{H}_t^N(\mathbf{t}))^T \times \mathbf{E}_t^N(\mathbf{t}) \cdot \mathbf{z} dS = diag(N_1, N_2, \cdots N_N) \tag{3.5}$$

Here the superscript "T" denotes the transpose operator. If we choose $\mathbf{M}(\mathbf{t})$ as

$$\mathbf{M}(\mathbf{t}) = \begin{bmatrix} \mathbf{H}_t^{A,N}(\mathbf{t}) & \mathbf{H}_t^{A,N}(\mathbf{t}) \\ -\mathbf{E}_t^{A,N}(\mathbf{t}) & \mathbf{E}_t^{A,N}(\mathbf{t}) \end{bmatrix}^T \tag{3.6}$$

Eq. (3.3) will be finally simplified as:

$$\mathbf{T} = \frac{1}{2} diag(\frac{1}{N_1^A}, \frac{1}{N_2^A}, \cdots, \frac{1}{N_N^A}, \frac{1}{N_1^A}, \frac{1}{N_2^A}, \cdots, \frac{1}{N_N^A}) \cdot \left(\iint_S \mathbf{M}(\mathbf{t}) \times \begin{bmatrix} \mathbf{E}_t^{B,N}(\mathbf{t}) & \mathbf{E}_t^{B,N}(\mathbf{t}) \\ \mathbf{H}_t^{B,N}(\mathbf{t}) & -\mathbf{H}_t^{B,N}(\mathbf{t}) \end{bmatrix} \cdot \mathbf{z} dS \right) \tag{3.7}$$

3.3 New theory for IMMM

It was assumed in previous uses of CMMM that mode orthogonality and normalization would be sufficient to provide clear physical understanding of **T**. Today, however, the realization has come that, with finite mode number, the fields at each interface cannot be matched precisely and so this is a deficiency of the prior art. Here we now present a formulation that solves this deficiency. We begin by rewriting Eq. (3.2) above into the following form:

$$\begin{bmatrix} \mathbf{E}_t^{A,N}(\mathbf{t}) & \mathbf{E}_t^{A,N}(\mathbf{t}) \\ \mathbf{H}_t^{A,N}(\mathbf{t}) & -\mathbf{H}_t^{A,N}(\mathbf{t}) \end{bmatrix} \cdot \mathbf{A} \approx \begin{bmatrix} \mathbf{E}_t^{B,N}(\mathbf{t}) & \mathbf{E}_t^{B,N}(\mathbf{t}) \\ \mathbf{H}_t^{B,N}(\mathbf{t}) & -\mathbf{H}_t^{B,N}(\mathbf{t}) \end{bmatrix} \cdot \mathbf{B} \tag{3.8}$$

The optimum **T** should be the one that causes the field residue error in Eq.(3.8) to be minimized. Based on this optimization idea, we can derive an IMMM by focusing upon those errors.

The field residue error from Eq.(3.8) can be defined as:

$$\Delta\mathbf{E}(\mathbf{t}) = \left[\mathbf{E}_t^{A,N}(\mathbf{t}) \quad \mathbf{E}_t^{A,N}(\mathbf{t})\right] \cdot \mathbf{A} - \left[\mathbf{E}_t^{B,N}(\mathbf{t}) \quad \mathbf{E}_t^{B,N}(\mathbf{t})\right] \cdot \mathbf{B} \tag{3.9a}$$

$$\Delta\mathbf{H}(\mathbf{t}) = \left[\mathbf{H}_t^{A,N}(\mathbf{t}) \quad -\mathbf{H}_t^{A,N}(\mathbf{t})\right] \cdot \mathbf{A} - \left[\mathbf{H}_t^{B,N}(\mathbf{t}) \quad -\mathbf{H}_t^{B,N}(\mathbf{t})\right] \cdot \mathbf{B} \tag{3.9b}$$

Therefore solving the CMMM deficiency can be equivalent to the optimization problem of:

$$\min_{\mathbf{T}} \left\|\Delta\mathbf{E}(\mathbf{t})\right\|_2^2 + \eta_0^2 \left\|\Delta\mathbf{H}(\mathbf{t})\right\|_2^2 \tag{3.10}$$

in which **T** is the variable to make the summation of two field error norm squares minimum. Here η_0 is the wave impedance in vacuum as $\eta_0 = \sqrt{\mu_0/\varepsilon_0}$, in which μ_0 and ε_0 are the permeability and permittivity in vacuum. Strictly speaking, the characteristic impedance of each mode should be included here to replace η_0 in Eq. (3.10). However, computation efforts are paid to find the characteristic impedance of corresponding modes. Fortunately, we found that the new algorism is not sensitive to modal characteristic impedance and the wave impedance in vacuum is a good approximation already. This can be explained by the fact that IMMM is based the optimization method and η just plays the

role to balance the electric- and magnetic- field in Eq. (3.10). The 2-norm square for a complex field is defined as $\left\|\Delta\mathbf{E}(\mathbf{t})\right\|_2^2 = \int_S \Delta\mathbf{E}(\mathbf{t})\cdot\Delta\mathbf{E}(\mathbf{t})^* dS$.

The MMM goals are: to derive the coefficient sets *A* and *B*, and to determine the electric/magnetic field distributions. In CMMM, we use the initial conditions and Eq. (3.7) above to reach those goals. Now, for IMMM we use instead the **T** obtained from Eq. (3.10) and the initial conditions. Eq. (3.10) can be rewritten as

$$\min_{\mathbf{T}} \left\| \begin{bmatrix} \mathbf{E}_t^{A,N}(\mathbf{t}) & \mathbf{E}_t^{A,N}(\mathbf{t}) \\ \eta_0\mathbf{H}_t^{A,N}(\mathbf{t}) & -\eta_0\mathbf{H}_t^{A,N}(\mathbf{t}) \end{bmatrix} \cdot \mathbf{A} - \begin{bmatrix} \mathbf{E}_t^{B,N}(\mathbf{t}) & \mathbf{E}_t^{B,N}(\mathbf{t}) \\ \eta_0\mathbf{H}_t^{B,N}(\mathbf{t}) & -\eta_0\mathbf{H}_t^{B,N}(\mathbf{t}) \end{bmatrix} \cdot \mathbf{B} \right\|_2^2 \tag{3.11}$$

Substituting $\mathbf{A} = \mathbf{T}\cdot\mathbf{B}$ into Eq. (3.11), then we have

$$\min_{\mathbf{T}} \left\| \begin{bmatrix} \mathbf{E}_t^{A,N}(\mathbf{t}) & \mathbf{E}_t^{A,N}(\mathbf{t}) \\ \eta_0\mathbf{H}_t^{A,N}(\mathbf{t}) & -\eta_0\mathbf{H}_t^{A,N}(\mathbf{t}) \end{bmatrix} \cdot \mathbf{T} - \begin{bmatrix} \mathbf{E}_t^{B,N}(\mathbf{t}) & \mathbf{E}_t^{B,N}(\mathbf{t}) \\ \eta_0\mathbf{H}_t^{B,N}(\mathbf{t}) & -\eta_0\mathbf{H}_t^{B,N}(\mathbf{t}) \end{bmatrix} \right\|_2^2 \tag{3.12}$$

The matrix 2-norm can be expressed as Eq. (2.3.2) in [86] as

$$\max_{\|\mathbf{x}\|_2=1} \left\| \left(\begin{bmatrix} \mathbf{E}_t^{A,N}(\mathbf{t}) & \mathbf{E}_t^{A,N}(\mathbf{t}) \\ \eta_0\mathbf{H}_t^{A,N}(\mathbf{t}) & -\eta_0\mathbf{H}_t^{A,N}(\mathbf{t}) \end{bmatrix} \cdot \mathbf{T} - \begin{bmatrix} \mathbf{E}_t^{B,N}(\mathbf{t}) & \mathbf{E}_t^{B,N}(\mathbf{t}) \\ \eta_0\mathbf{H}_t^{B,N}(\mathbf{t}) & -\eta_0\mathbf{H}_t^{B,N}(\mathbf{t}) \end{bmatrix} \right)\mathbf{x} \right\|_2^2 \tag{3.13}$$

where the vector **x** is a *N* by 1 arbitrary vector with unity 2-norm value. The targeting problem Eq. (3.12) can be re-written as

$$\min_{\mathbf{T}} \max_{\|\mathbf{x}\|_2=1} \left\| \left(\begin{bmatrix} \mathbf{E}_t^{A,N}(\mathbf{t}) & \mathbf{E}_t^{A,N}(\mathbf{t}) \\ \eta_0\mathbf{H}_t^{A,N}(\mathbf{t}) & -\eta_0\mathbf{H}_t^{A,N}(\mathbf{t}) \end{bmatrix} \cdot \mathbf{T}\mathbf{x} - \begin{bmatrix} \mathbf{E}_t^{B,N}(\mathbf{t}) & \mathbf{E}_t^{B,N}(\mathbf{t}) \\ \eta_0\mathbf{H}_t^{B,N}(\mathbf{t}) & -\eta_0\mathbf{H}_t^{B,N}(\mathbf{t}) \end{bmatrix} \mathbf{x} \right) \right\|_2^2 \tag{3.14}$$

Exchange the order of minimization and maximization, and let $\mathbf{y}=\mathbf{T}\cdot\mathbf{x}$, the above optimization problem can be equalized to the following form:

$$\max_{\|\mathbf{x}\|_2=1} \min_{\mathbf{y}} \left\| \left(\begin{bmatrix} \mathbf{E}_t^{A,N}(\mathbf{t}) & \mathbf{E}_t^{A,N}(\mathbf{t}) \\ \eta_0 \mathbf{H}_t^{A,N}(\mathbf{t}) & -\eta_0 \mathbf{H}_t^{A,N}(\mathbf{t}) \end{bmatrix} \mathbf{y} - \begin{bmatrix} \mathbf{E}_t^{B,N}(\mathbf{t}) & \mathbf{E}_t^{B,N}(\mathbf{t}) \\ \eta_0 \mathbf{H}_t^{B,N}(\mathbf{t}) & -\eta_0 \mathbf{H}_t^{B,N}(\mathbf{t}) \end{bmatrix} \mathbf{x} \right) \right\|_2^2 \tag{3.15}$$

We first focus on the minimization process, and in this step, the **x** can be treated as a constant. This formula is similar to the least square problem in linear system, and can be solved following chapter 5.3 in [86]. Consider the function $f(\mathbf{y})$ defined as

$$f(\mathbf{y}) = \left\| \begin{bmatrix} \mathbf{E}_t^{A,N}(\mathbf{t}) & \mathbf{E}_t^{A,N}(\mathbf{t}) \\ \eta_0 \mathbf{H}_t^{A,N}(\mathbf{t}) & -\eta_0 \mathbf{H}_t^{A,N}(\mathbf{t}) \end{bmatrix} \mathbf{y} - \begin{bmatrix} \mathbf{E}_t^{B,N}(\mathbf{t}) & \mathbf{E}_t^{B,N}(\mathbf{t}) \\ \eta_0 \mathbf{H}_t^{B,N}(\mathbf{t}) & -\eta_0 \mathbf{H}_t^{B,N}(\mathbf{t}) \end{bmatrix} \mathbf{x} \right\|_2^2 \tag{3.16}$$

$$= \mathbf{y}^H \cdot \iint_S \left(\begin{bmatrix} \mathbf{E}_t^{A,N}(\mathbf{t}) & \mathbf{E}_t^{A,N}(\mathbf{t}) \\ \eta_0 \mathbf{H}_t^{A,N}(\mathbf{t}) & -\eta_0 \mathbf{H}_t^{A,N}(\mathbf{t}) \end{bmatrix} \right)^H \cdot \begin{bmatrix} \mathbf{E}_t^{A,N}(\mathbf{t}) & \mathbf{E}_t^{A,N}(\mathbf{t}) \\ \eta_0 \mathbf{H}_t^{A,N}(\mathbf{t}) & -\eta_0 \mathbf{H}_t^{A,N}(\mathbf{t}) \end{bmatrix} dS \cdot \mathbf{y}$$

$$-\mathbf{x}^H \cdot \iint_S \left(\begin{bmatrix} \mathbf{E}_t^{B,N}(\mathbf{t}) & \mathbf{E}_t^{B,N}(\mathbf{t}) \\ \eta_0 \mathbf{H}_t^{B,N}(\mathbf{t}) & -\eta_0 \mathbf{H}_t^{B,N}(\mathbf{t}) \end{bmatrix} \right)^H \cdot \begin{bmatrix} \mathbf{E}_t^{A,N}(\mathbf{t}) & \mathbf{E}_t^{A,N}(\mathbf{t}) \\ \eta_0 \mathbf{H}_t^{A,N}(\mathbf{t}) & -\eta_0 \mathbf{H}_t^{A,N}(\mathbf{t}) \end{bmatrix} dS \cdot \mathbf{y}$$

$$-\mathbf{y}^H \cdot \iint_S \left(\begin{bmatrix} \mathbf{E}_t^{A,N}(\mathbf{t}) & \mathbf{E}_t^{A,N}(\mathbf{t}) \\ \eta_0 \mathbf{H}_t^{A,N}(\mathbf{t}) & -\eta_0 \mathbf{H}_t^{A,N}(\mathbf{t}) \end{bmatrix} \right)^H \cdot \begin{bmatrix} \mathbf{E}_t^{B,N}(\mathbf{t}) & \mathbf{E}_t^{B,N}(\mathbf{t}) \\ \eta_0 \mathbf{H}_t^{B,N}(\mathbf{t}) & -\eta_0 \mathbf{H}_t^{B,N}(\mathbf{t}) \end{bmatrix} dS \cdot \mathbf{x}$$

$$+\mathbf{x}^H \cdot \iint_S \left(\begin{bmatrix} \mathbf{E}_t^{B,N}(\mathbf{t}) & \mathbf{E}_t^{B,N}(\mathbf{t}) \\ \eta_0 \mathbf{H}_t^{B,N}(\mathbf{t}) & -\eta_0 \mathbf{H}_t^{B,N}(\mathbf{t}) \end{bmatrix} \right)^H \cdot \begin{bmatrix} \mathbf{E}_t^{B,N}(\mathbf{t}) & \mathbf{E}_t^{B,N}(\mathbf{t}) \\ \eta_0 \mathbf{H}_t^{B,N}(\mathbf{t}) & -\eta_0 \mathbf{H}_t^{B,N}(\mathbf{t}) \end{bmatrix} dS \cdot \mathbf{x}$$

The superscript "H" denotes the Hermitian operator.

Since the matrix $\iint_S \left(\begin{bmatrix} \mathbf{E}_t^{A,N}(\mathbf{t}) & \mathbf{E}_t^{A,N}(\mathbf{t}) \\ \eta_0 \mathbf{H}_t^{A,N}(\mathbf{t}) & -\eta_0 \mathbf{H}_t^{A,N}(\mathbf{t}) \end{bmatrix} \right)^H \cdot \begin{bmatrix} \mathbf{E}_t^{A,N}(\mathbf{t}) & \mathbf{E}_t^{A,N}(\mathbf{t}) \\ \eta_0 \mathbf{H}_t^{A,N}(\mathbf{t}) & -\eta_0 \mathbf{H}_t^{A,N}(\mathbf{t}) \end{bmatrix} dS$ is positive definite, the minimum appears when the derivative of the scalar function $f(\mathbf{y})$ in terms of **y** equals zero, i.e.,

$$\frac{df}{d\mathbf{y}} = 2\,\mathrm{Re}\{\iint_S (\begin{bmatrix} \mathbf{E}_t^{A,N}(\mathbf{t}) & \mathbf{E}_t^{A,N}(\mathbf{t}) \\ \eta_0 \mathbf{H}_t^{A,N}(\mathbf{t}) & -\eta_0 \mathbf{H}_t^{A,N}(\mathbf{t}) \end{bmatrix})^H \cdot \begin{bmatrix} \mathbf{E}_t^{A,N}(\mathbf{t}) & \mathbf{E}_t^{A,N}(\mathbf{t}) \\ \eta_0 \mathbf{H}_t^{A,N}(\mathbf{t}) & -\eta_0 \mathbf{H}_t^{A,N}(\mathbf{t}) \end{bmatrix} dS \cdot \mathbf{y} \tag{3.17}$$

$$-\iint_S (\begin{bmatrix} \mathbf{E}_t^{A,N}(\mathbf{t}) & \mathbf{E}_t^{A,N}(\mathbf{t}) \\ \eta_0 \mathbf{H}_t^{A,N}(\mathbf{t}) & -\eta_0 \mathbf{H}_t^{A,N}(\mathbf{t}) \end{bmatrix})^H \cdot \begin{bmatrix} \mathbf{E}_t^{B,N}(\mathbf{t}) & \mathbf{E}_t^{B,N}(\mathbf{t}) \\ \eta_0 \mathbf{H}_t^{B,N}(\mathbf{t}) & -\eta_0 \mathbf{H}_t^{B,N}(\mathbf{t}) \end{bmatrix} dS \cdot \mathbf{x}\} = 0$$

or

$$\{\iint_S (\begin{bmatrix} \mathbf{E}_t^{A,N}(\mathbf{t}) & \mathbf{E}_t^{A,N}(\mathbf{t}) \\ \eta_0 \mathbf{H}_t^{A,N}(\mathbf{t}) & -\eta_0 \mathbf{H}_t^{A,N}(\mathbf{t}) \end{bmatrix})^H \cdot \begin{bmatrix} \mathbf{E}_t^{A,N}(\mathbf{t}) & \mathbf{E}_t^{A,N}(\mathbf{t}) \\ \eta_0 \mathbf{H}_t^{A,N}(\mathbf{t}) & -\eta_0 \mathbf{H}_t^{A,N}(\mathbf{t}) \end{bmatrix} dS \cdot \mathbf{T} \tag{3.18}$$

$$-\iint_S (\begin{bmatrix} \mathbf{E}_t^{A,N}(\mathbf{t}) & \mathbf{E}_t^{A,N}(\mathbf{t}) \\ \eta_0 \mathbf{H}_t^{A,N}(\mathbf{t}) & -\eta_0 \mathbf{H}_t^{A,N}(\mathbf{t}) \end{bmatrix})^H \cdot \begin{bmatrix} \mathbf{E}_t^{B,N}(\mathbf{t}) & \mathbf{E}_t^{B,N}(\mathbf{t}) \\ \eta_0 \mathbf{H}_t^{B,N}(\mathbf{t}) & -\eta_0 \mathbf{H}_t^{B,N}(\mathbf{t}) \end{bmatrix} dS\} \cdot \mathbf{x} = 0$$

Hence the optimized **T** should be chosen as

$$\mathbf{T} = \left(\iint_S (\begin{bmatrix} \mathbf{E}_t^{A,N}(\mathbf{t}) & \mathbf{E}_t^{A,N}(\mathbf{t}) \\ \eta_0 \mathbf{H}_t^{A,N}(\mathbf{t}) & -\eta_0 \mathbf{H}_t^{A,N}(\mathbf{t}) \end{bmatrix})^H \cdot \begin{bmatrix} \mathbf{E}_t^{A,N}(\mathbf{t}) & \mathbf{E}_t^{A,N}(\mathbf{t}) \\ \eta_0 \mathbf{H}_t^{A,N}(\mathbf{t}) & -\eta_0 \mathbf{H}_t^{A,N}(\mathbf{t}) \end{bmatrix} dS \right)^{-1} \tag{3.19}$$

$$\cdot \left(\iint_S (\begin{bmatrix} \mathbf{E}_t^{A,N}(\mathbf{t}) & \mathbf{E}_t^{A,N}(\mathbf{t}) \\ \eta_0 \mathbf{H}_t^{A,N}(\mathbf{t}) & -\eta_0 \mathbf{H}_t^{A,N}(\mathbf{t}) \end{bmatrix})^H \cdot \begin{bmatrix} \mathbf{E}_t^{B,N}(\mathbf{t}) & \mathbf{E}_t^{B,N}(\mathbf{t}) \\ \eta_0 \mathbf{H}_t^{B,N}(\mathbf{t}) & -\eta_0 \mathbf{H}_t^{B,N}(\mathbf{t}) \end{bmatrix} dS \right)$$

Here one thing to mention is, the minimization process yields **T** irrelevant to variable **x**. And it should be noted that we do not have to utilize mode orthogonality.

After achieving the whole modal coefficients - vectors **A** and **B** - with **T** from MMM, the electric and magnetic fields (denoted as $\hat{\mathbf{E}}(\mathbf{t})$ and $\hat{\mathbf{H}}(\mathbf{t})$) at the interface in both structures *A* and *B* can be expressed as:

$$\hat{\mathbf{E}}_A(\mathbf{t}) = \begin{bmatrix} \mathbf{E}_t^{A,N}(\mathbf{t}) & \mathbf{E}_t^{A,N}(\mathbf{t}) \end{bmatrix} \cdot \mathbf{A} \tag{3.20a}$$

$$\hat{\mathbf{H}}_A(\mathbf{t}) = \begin{bmatrix} \mathbf{H}_t^{A,N}(\mathbf{t}) & -\mathbf{H}_t^{A,N}(\mathbf{t}) \end{bmatrix} \cdot \mathbf{A} \tag{3.20b}$$

$$\hat{\mathbf{E}}_B(\mathbf{t}) = \left[\mathbf{E}_t^{B,N}(\mathbf{t}) \quad \mathbf{E}_t^{B,N}(\mathbf{t})\right] \cdot \mathbf{B} \tag{3.21a}$$

$$\hat{\mathbf{H}}_B(\mathbf{t}) = \left[\mathbf{H}_t^{B,N}(\mathbf{t}) \quad -\mathbf{H}_t^{B,N}(\mathbf{t})\right] \cdot \mathbf{B} \tag{3.21b}$$

Then the field mismatch error $\Delta(F)$ can be defined as in Eq. (2.21) to judge the performance of different MMMs:

$$\Delta(F) = \frac{\iint_S \left|\hat{\mathbf{F}}_A - \hat{\mathbf{F}}_B\right| dS}{\iint_S \left|\hat{\mathbf{F}}_{in}\right| dS} \tag{3.22}$$

Here $\hat{\mathbf{F}}$ can either be the electric or magnetic field in Eq. (3.20) or in Eq. (3.21), and $\hat{\mathbf{F}}_{in}$ is the input excitation field. The mismatch error is calculated separately for the CMMM and IMMM cases. The difference between those cases is in the **T** that is from Eq. (3.7) for CMMM and derived from Eq. (3.19) for IMMM. After that, Eq. (3.20) gives the fields in structure *A* while Eq. (3.21) gives us fields in structure *B*. As the number of modes is limited, fields from the left and right are not the same and Eq. (3.22) gives us the mismatch.

3.4 Simulation for the truncated SOI channel waveguide

In this section, we apply the IMMM to simulate the scattering field of a SOI channel waveguide facet structure that is illustrated in Figure 3.2, we shall determine the accuracy of IMMM numerical results and shall compare the accuracy to that of CMMM. The height and width of the silicon channel are 220 nm by 500 nm. The refractive indices in

this simulation for SiO_2, Si and air are 1.44, 3.47 and 1.0, respectively and the operating wavelength is 1550 nm. Our computational goal is to calculate the field distribution at the Si/air interface when the fundamental mode in the Si channel is excited. Speaking generally, the field distribution can be calculated using modes—as presented here—or without modes using FDTD or BPM. In the present case, fields are determined by the modes' coefficients *A* and *B* as in Eq. (3.20) and Eq. (3.21). The modes are an intrinsic structure-property and the coefficients are determined by the excitation. In summary, the coefficient-calculation leads to the field distribution at the interface. Here we test both the 1D and 2D cases for such a structure, to justify the performance of IMMM for both 1D and 2D modes. When we apply the MMM simulation tool, such an open structure needs to be truncated by PML and PRB along the transverse directions.

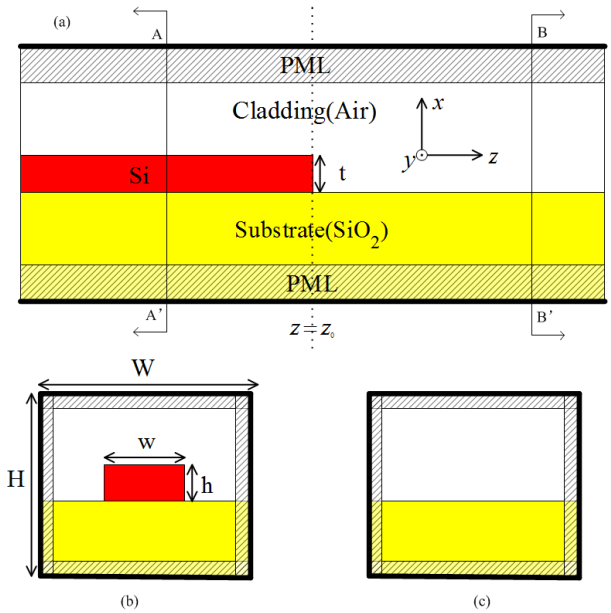

Figure 3.2 A SOI waveguide facet. The propagation direction is along +*z* and the SOI waveguide facet is located at $z=z_0$. The height and width of the Silicon slab is 220 nm by

500 nm. The refractive indices for SiO_2, Si and air are 1.44, 3.47 and 1.0, respectively. The structure is truncated by PML and PRB.

3.4.1. Simulation for 1D case

In the 1D case, we assume the width of Si channel is infinite other than 500 nm aforementioned. The thicknesses of the truncated area is 2.22 μm and PML is 2 μm. The complex modes are calculated by a finite-difference method with a fixed mesh size Δx=0.005μm [54], and the complex modes for both structures are solved and sorted by increasing loss. One hundred complex modes are calculated and are reliable in terms of their effective- index and field convergence.

We have assumed a parabolic absorption profile of the boundary reflectivity R_{PML} for PML in the SiO_2 substrate. As for PML in the cladding, we choose a different R_{PML} value to keep the WOPD identical in cladding and substrate, thus the high Berenger modes can be more symmetric and will benefit the efficiency of both CMMM and IMMM as we discussed in Chapter 2. R_{PML} takes a value from 0 to 1. When R_{PML}=1, there is no absorption from PML, and only PRB works as a box discretization. In that circumstance, modes are purely real or imagery, whilst R_{PML} approaching R_{PML}=0 represents PML with strong absorption wherein the modes become complex with considerable real and imagery parts at the same time.

In both IMMM and CMMM simulation, the forward fundamental TE/TM mode is launched, so the input excitation fields can be expanded with modal coefficients $a_1^+ = 1$ while all other a_i^+ and b_i^- take the value 0. (The initial condition is derived from

excitation and is fixed for both methods. The difference between CMMM and IMMM is in the **T** derivation mentioned above.)

Using the tangential electric/magnetic field for the TE/TM cases respectively in Eq. (3.22), we plot in Figure 3.3 the field mismatch error as a function of the number of modes in the mode matching, and the solid lines are fitting curves to clarify the convergence trends. From Figure 3.3, firstly it can be observed that mismatch errors decrease considerably when more modes are applied. Moreover, we observe that field mismatch error decreases faster in the IMMM case for both TE and TM fields, and the average convergence speeds for four cases in Figure 3.3 are -1, -0.76, -0.83, and -0.74 dB/mode respectively. For N=90, the error from CMMM is nearly twice that from IMMM for both TE and TM cases, while at the N=10 start in Figure 3.3, both methods share the same level of mismatch error. So for a given number of modes, IMMM shows a smaller error. Also, during computation, calculation of Si/air interface fields with IMMM offers a faster convergence speed than CMMM. From Figure 3.3, we observe the convergence trend of mode matching and we conclude that the IMMM surpasses CMMM for finite, limited N.

The field mismatch can directly affect the method accuracy as shown in Figure 3.4, in which field A in Eq. (3.20) is compared with a 2D-FDTD result. We also plot the fitting curves as solid lines to show the trends. The relative field error ΔF is defined in the same way as in Eq. (2.21). Here we only compare the field in non-PML region, because the FDTD and MMM may have different ways to construct PMLs. In Figure 3.4, again four curves show the declining trend which indicates that, with increasing N, the field

from MMM is converging to the FDTD results, thereby demonstrating the accuracy of MMM. In addition, each curve from IMMM has a faster rate of decline compared with its corresponding CMMM curve, and the convergence speeds on average for 4 cases in Figure 3.4 are -1.04, -0.82, -0.81, and -0.69dB/mode respectively. Starting from nearly the same level of error with 10 modes, when N increases to 90, the error from CMMM is about 10 times larger than the one from IMMM in the TE case, and is nearly 3 times larger in the TM case. Simulations in Figure 3.3 and Figure 3.4 demonstrate that IMMM is more accurate and efficient compared with CMMM, as predicted in our former formulation.

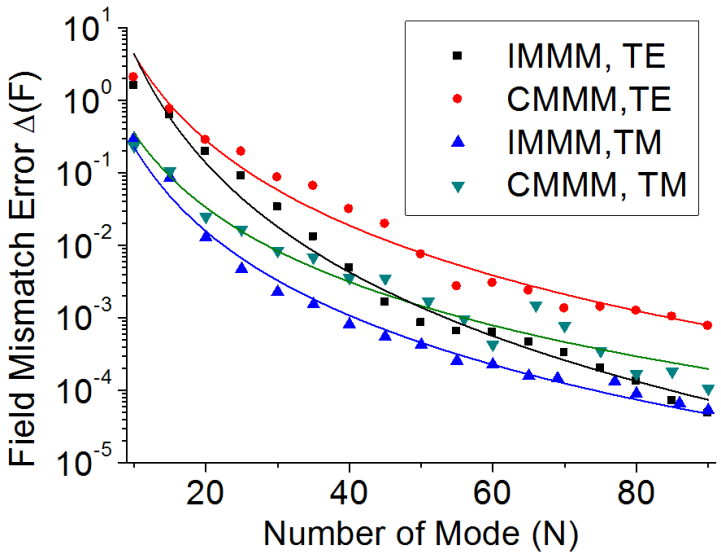

Figure 3.3 Field mismatch error as a function of the total number of modes involved for both TE and TM fields

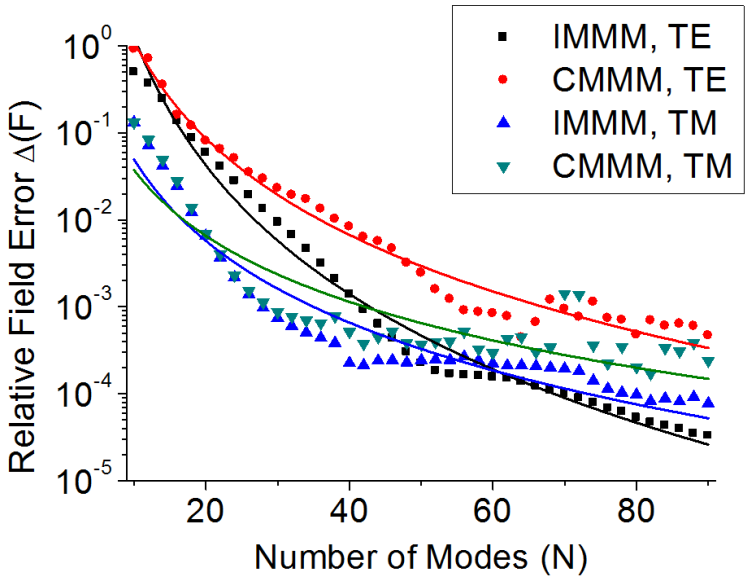

Figure 3.4 Relative field errors (with the FDTD result as the benchmark) as a function of the total number of modes involved for both TE and TM fields.

3.4.2. Simulation for 2D case

If we consider the width of the channel and conduct the full vector modal analysis, the pure TE/TM modes will change into quasi-TE/TM modes, and in our case, the quasi-TM mode is cut-off, which means the excited wave can only be the quasi-TE mode. Here the truncated area is 1.5μm by 1.22μm, and the thickness of PML is 200 nm in each side. The imagery part of PML thickness is 0.2μm and can be related to the refection of PML in former section as in Eq. (2.13). In complex mode solver based on FDM [49], the discretization mesh size is homogeneous along x and y direction, which is 5 nm.

Following the procedure in 1D case, we first test the two MMMs regarding field mismatch error at the interface, and then the relative error compared with 3D-FDTD result, and the results are shown in Figure 3.5 and Figure 3.6. For the IMMM case, a 10%

decrease can be observed for both cases. Compared with 1D case, this number is not fascinating, considering the extra computational resources consumed. The increase of computation effort can be generalized into the following aspects: 1) more modes are involved in the calculation (with 150 in 2D and 100 in 1D); 2) more mesh points induces larger matrix in eigen-value problem. In 1D, only 1244 values are taken to represent the field, making the eigen-problem sized 1244 x 1244 (the matrix for eigen-problem is sized as the square of the number of sample points in space), while in 2D, 324 x 244 points, which is 79056 points, making the eigen-problem even larger by 79056 x 79056. 3) In 1D simulation, only 2 transverse field components are involved, while in 2D case, 4 components are included as in the full vector modal analysis.

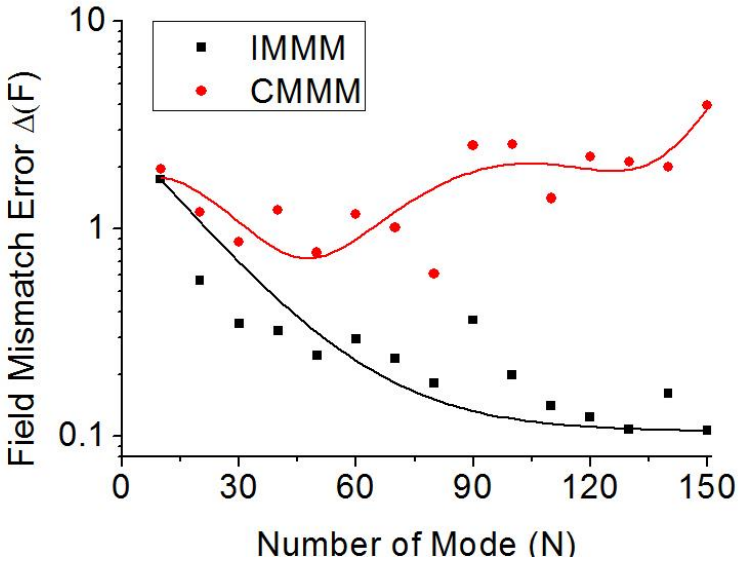

Figure 3.5 Field mismatch error as a function of the total number of modes involved for the fundamental mode.

The reason why we apply so much more effort in 2D case is to guarantee that the 1D and 2D simulations are utilizing the same mesh size. Even so, the performance in 2D is still not competent with 1D case. The reasons lay in the following aspects: 1) Even the mesh size keeps the same, the error from FDM algorithm is still larger in 2D case. This is because in 1D simulation, we can apply the difference operators with high order accuracy, while in 2D only central difference with 2nd order accuracy is adopted. High order boundary condition for 2D mode solver is still a challenge in prior art. 2) In 1D case, thicker PML with larger absorption coefficient are used, which means the reflection from boundaries is smaller. In 2D case, we apply much thinner PML considering the computation expense, and as a trade-off for modes' accuracy, smaller reflection is adopted. Consequently, more accurate result can be achieved in 1D modes.

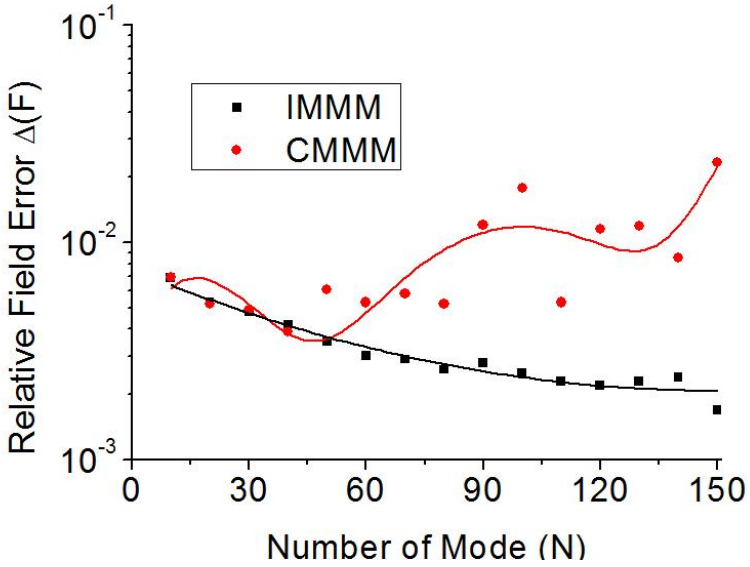

Figure 3.6 Relative field errors (with the FDTD result as the benchmark) as a function of the total number of modes involved for the fundamental mode.

Even though IMMM in 2D yields worse performance compared with 1D simulation, it still shows significant improvement over the CMMM. As shown in Figure 3.5 and Figure 3.6, the CMMM curve starts to blow up after about 40 modes, and finally cannot converged to zero in terms of mismatch error and relative error compared with FDTD. The reason is due to the inaccuracy of high order modes. Because the CMMM is using modal orthogonality, which is highly sensitive to the modes' accuracy, especially for higher order modes, the degeneration of modes may lead the failure of CMMM. Under the aforementioned simulation conditions, the modal orthogonality is checked for both SOI channel structure and the SiO2/air half space structure through the overlap integral of transverse electric-field and magnetic-field as in Eq. (3.4). Here we normalized the mode profiles by imposing N_i=1 for each mode. The results are shown in Figure 3.7. We can observe that only first 20 modes can hold decent orthogonality, i.e., the overlap integral follows the Dirac function distribution. Obviously, the CMMM cannot tolerate such a mess in orthogonality. Thus the IMMM is much more tolerable to this level of error from mode solver, and then much robust especially in the 2D case.

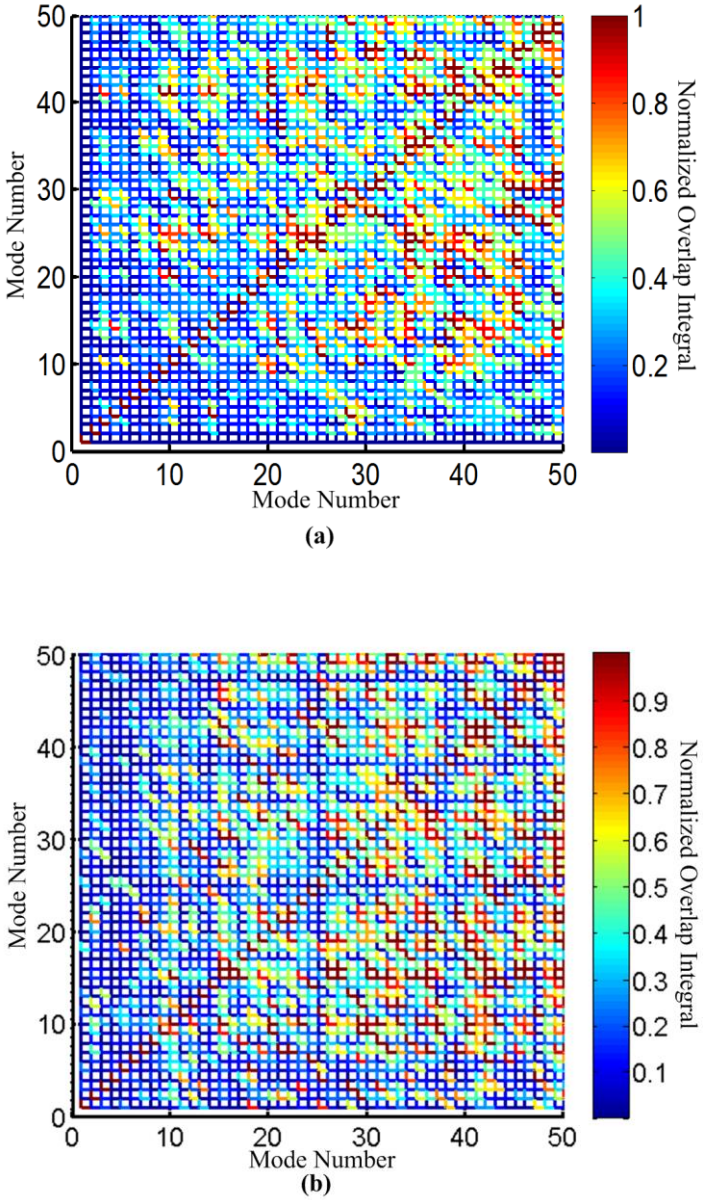

Figure 3.7 Normalized overlap integral for transverse electric-field and magnetic-field for (a) SOI channel waveguide and (b) SiO2/air half space waveguide.

As the modern development in computational technology , one may argue that the conventional method can be saved through updating the computers' capability, which is definitely true. However, as shown in 1D case, even when the CMMM is still working,

the IMMM can behave more efficient. Besides, the reason why we pursue the modal analysis or MMM is because of the higher time and space efficiency compared with FDTD simulator. Now with smaller mesh size and longer simulation time, we are sacrificing the advantage in modal analysis or MMM. Eventually, the simulation is not only needed for feasibility tests, but also used for optimization of devices. Any acceleration in basic algorithm may lead to huge improvement in optimization process.

Figure 3.8 shows the transverse magnetic field components from IMMM compared with FDTD results when 150 modes are used. Figure 3.8(a) and (b) are restored with SOI modes as in Eq. (3.20), (c) and (d) are with SiO2/air half space modes as in Eq. (3.21), and (e) and (f) are from 3D FDTD simulations. Each field component is normalized separately by the FDTD result, and the scaling color bar is shown at the bottom. Figure 3.8 shows the best situations in Figure 3.5 in terms of fields convergence at the interface, and in Figure 3.6 in terms of accuracy of converged field compared with the FDTD results.

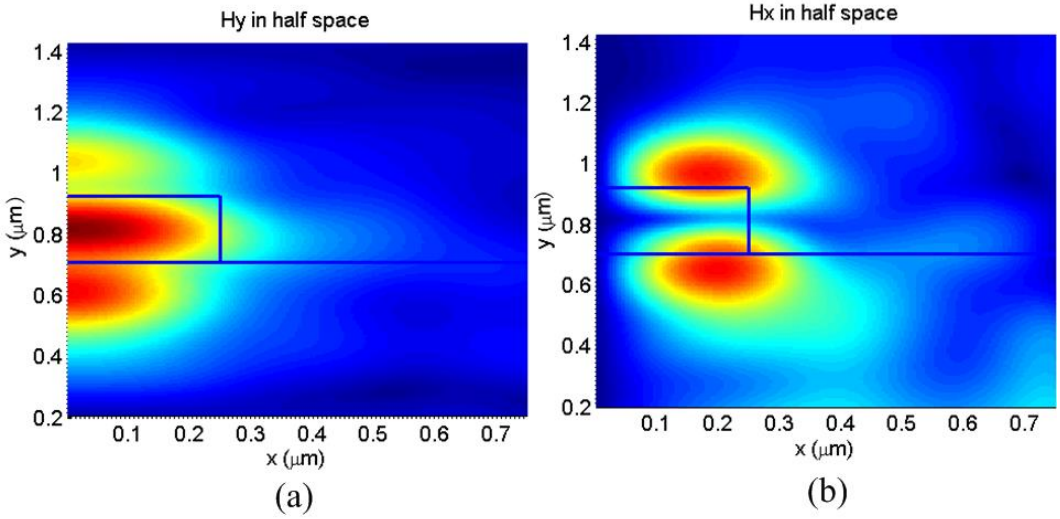

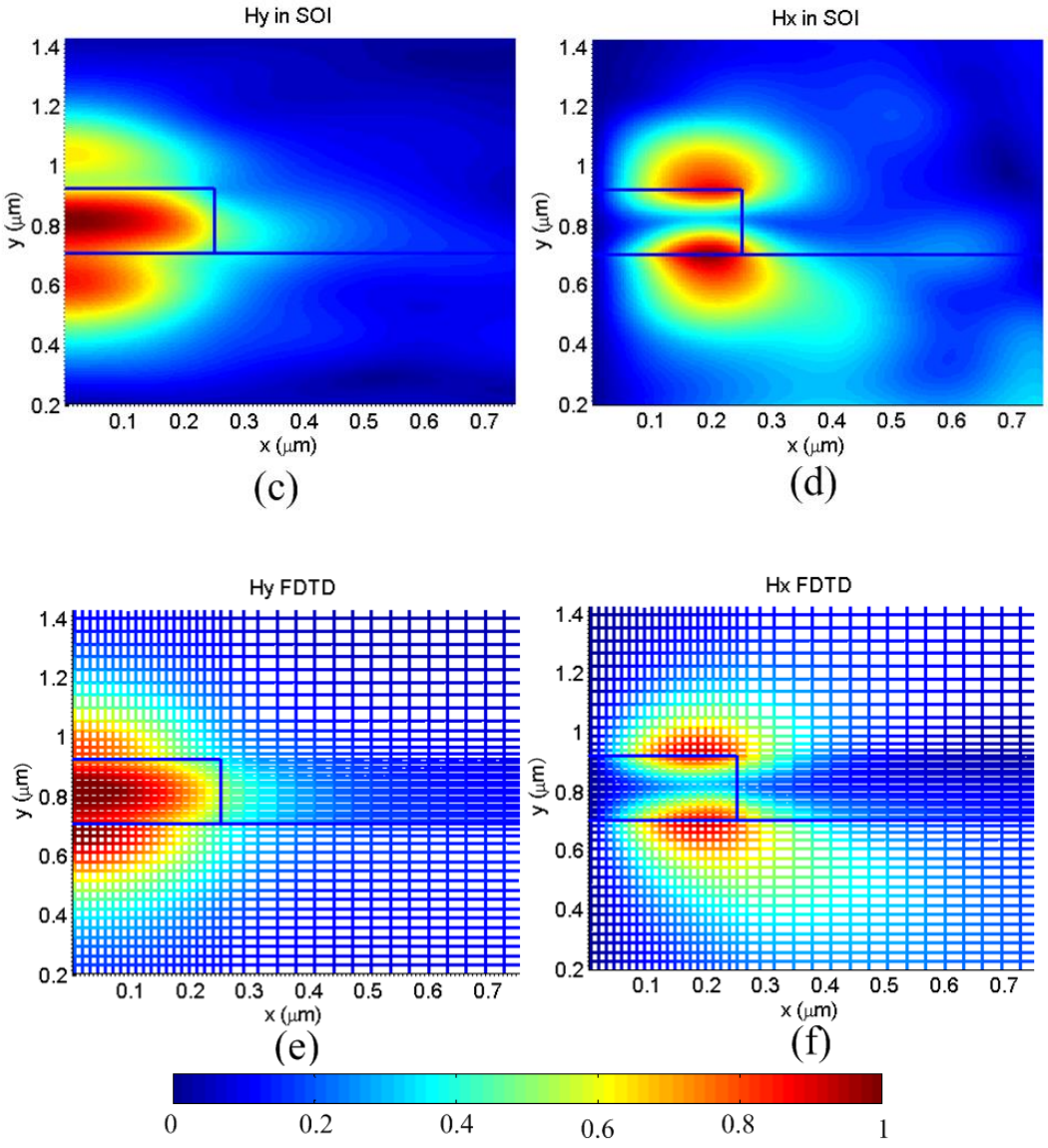

Figure 3.8 Transverse magnetic field components from IMMM (a) ~(d) and FDTD (e)~(f). The (a) and (b) are fields restored by modes in SOI channel waveguide. (c) and (d) are fields restored by modes in SiO2/air waveguide. Each component is normalized by corresponding FDTD results.

3.5 Roles of high order bending modes in optical wave coupling

Bending structures have been widely used in photonics designs of multimode interference devices, power splitters, Mach-Zander interferometers, directional couplers, and also interconnectors in integrated photonic circuits. A well-designed waveguide bend should have merits such as low transmission loss, low field distortion at the output, etc.[87]. For high density photonic integrated circuits applications, waveguide bending structures with smaller bending radii are widely employed, which results in an even more pronounced radiation effect[88].

Rigorous analysis of radiation coupling in bending waveguide structure is challenging. Analytical solutions based on guided modes and leaky modes are not accurate and only valid in two-dimensional approximations in which large structure aspect ratio is assumed[89]. A more generic method is employing the complex modes in the case that the computation window is truncated by PML and PRB conditions. By that, radiation effect can be approximated by a series of discretized complex modes, and at the same time the modal behavior of guided modes are disturbed in the non-PML region of the computation window[90]. With the complete and discrete complex mode set, the MMM can be implemented to simulate the transmission and reflection at the interface accurately[78].

In this sub-section, we investigated bending waveguide structures with very small bending radii. For those structures, high order bending modes contribute to the energy

transfer significantly. We first calculated the higher order modes and discussed their modal characteristics. IMMM and CMMM will again be compared in this case, after which IMMM will be used to explore the optical coupling. Finally, we presented a guideline of choosing high order bending modes in the optical coupling.

3.5.1. Derivation for complex bending modes

Consider a bending structure as shown in Figure 3.9(a). The bending radius is denoted as R, the thickness and refractive index of guiding waveguide as d and n_1, respectively. The refractive index of cladding is n_o, and r is the radial coordinate. PML and PRB are introduced as absorbing boundaries along radial direction. Under the scheme in Figure 3.9(a), the governing equations derived from modified Maxwell equations in the cylindrical coordinates are shown as Eq.(3.23):

$$\frac{1}{\alpha_r}\frac{r}{R}\frac{d}{dr}\frac{1}{\alpha_r}\frac{r}{R}\frac{de_y}{dr}+(k_0^2n^2\frac{r^2}{R^2}-\beta^2)e_y=0 \quad \text{(TE case)} \tag{3.23a}$$

$$\frac{1}{\alpha_r}\frac{r}{R}\frac{d}{dr}\frac{1}{\alpha_r}\frac{r}{R}\frac{dh_y}{dr}+(k_0^2n^2\frac{r^2}{R^2}-\beta^2)h_y=0 \quad \text{(TM case)} \tag{3.23b}$$

Here β is the propagation constant, e_y and h_y are the corresponding modal field distribution along radial direction, k_0 is the wave number in vacuum, n is the refractive index and the α_r is the stretching factor along radial direction determined by the reflection of PML[73]. Conformal transformation[91] is used to map the step-index bending structure into a straight planner structure with index profile as shown in Figure 3.9 (b). The coordinate and index transformations are descripted as

$$u = R\ln\frac{r}{R}, n_{eq}(u) = n(r)e^{\frac{u}{R}} \tag{3.24}$$

For the structure with PML and PRB, the complex coordinate is normally utilized:

$$\tilde{u} = \int \alpha_r(u)du \tag{3.25}$$

Here the stretching factor can be expressed with operating wavelength λ , thickness of PML d_{PML} , the distance to the PML boundary ρ and the reflection of PML R_{PML} as :

$$\alpha_r(u) = 1 - j\frac{\lambda}{4\pi}\frac{1}{\int_0^{d_{PML}} n_{eq}(u)\left(\frac{\rho}{d_{PML}}\right)^2 d\rho}\left(\frac{\rho}{d_{PML}}\right)^2 \ln\frac{1}{R_{PML}} \tag{3.26}$$

After the conformal and complex coordinate transformationS, the governing equations for bending modes in Eq.(3.23) will be simplified as in Eq (3.27), which are exactly the same as the ones for the straight waveguides without PML and can be easily solved with conventional mode solvers under changing index profile and complex coordinate. In our simulations, bending modes are calculated by the FDM with high order boundary condition we used for all the 1D simulation in this chapter[54].

$$\frac{de_y}{d\tilde{u}^2} + (k_0^2 n_{eq}{}^2(\tilde{u}) - \beta^2)e_y = 0 \quad \text{(TE case)} \tag{3.27a}$$

$$\frac{dh_y}{d\tilde{u}^2} + (k_0^2 n_{eq}{}^2(\tilde{u}) - \beta^2)h_y = 0 \quad \text{(TM case)} \tag{3.27b}$$

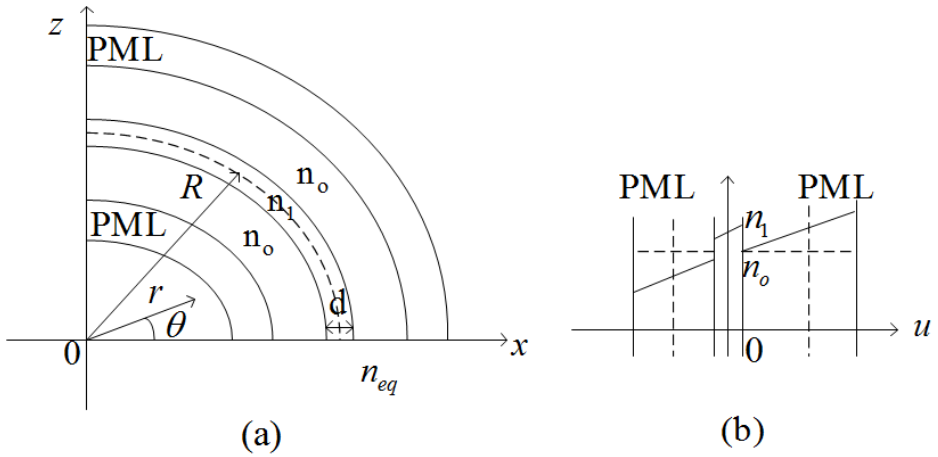

Figure 3.9 (a) a bending structure with PML and PRB. Refractive index and thickness of guiding waveguide are n_1 and d, respectively. Refractive index of cladding is n_o, and bending radius is R. (b) Refractive index profile of the corresponding straight waveguide for the bending structure after conformal transformation.

3.5.2. High order bending modes in light coupling

To investigate the roles of bending modes in light coupling, we take the 90^o bending structure with index $n_1 = 3.24$, $n_o = 3.18$ and d=3μm as an example[60]. In the simulation, we truncated the cladding region at 3μm away from the inner edge of the guiding waveguide with a 3μm PML, while at 5μm away from the outer edge with a 5μm PML. We use a small enough reflection of PML ($R_{PML} = 10^{-6}$) to make the leaky and guided modes converge. The operating wavelength is 1550nm and we focus on the TE case.

Figure 3.10 shows effective modal index of bending modes for R=100 μm, 50 μm, 25 μm, 20 μm, 15 μm, and 10 μm, respectively. We observe that, as the bending radius decreases to 25μm, there is no guided modes any more, and leaky modes become

pronounced. We tracked electric field intensity distributions of the first two modes. Figure 3.11 shows that, as radius decreases, light starts to leak out into the cladding area. Moreover, the Berenger modes split into two branches, which is due to the asymmetric index profile as shown in Figure 3.9(b). In Figure 3.10(b), modes revolution is shown when radius of bend gets even smaller. The two groups of modes are discerned clearly: the leaky modes (group A) and the Berenger modes (group B).

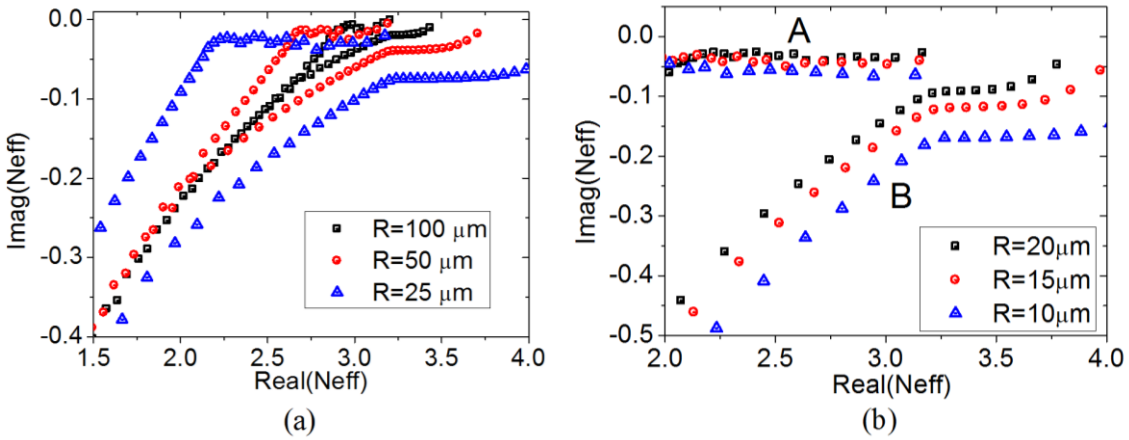

Figure 3.10 Mode spectrum under different bending radii. (a) Guided modes disappear while leaky modes generated as radius gets smaller (b) when radius diminishes seriously, bend modes can be classified into leaky modes (group A) and Berenger modes (group B)

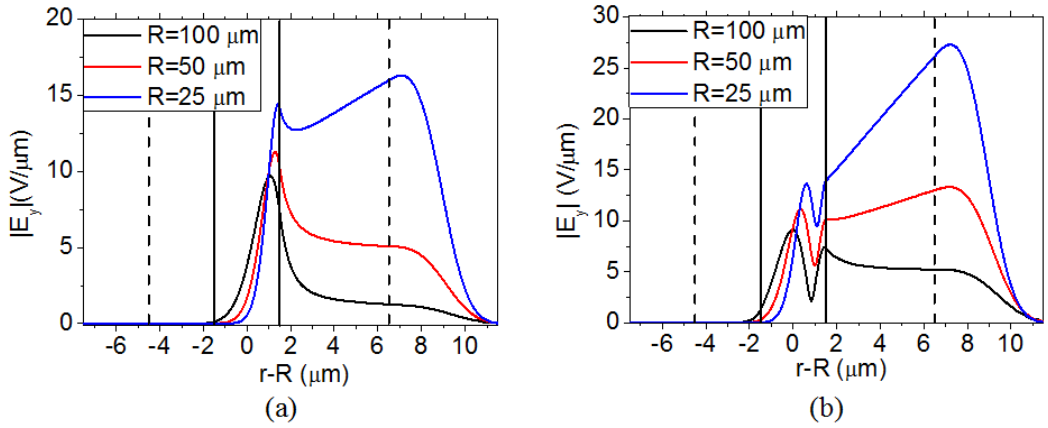

Figure 3.11 First two modes' electric field intensity distributions as radius reduces. Guided modes change into leaky modes

3.5.3. Light transmission simulation from MMM

As we can observe in Figure 3.10, the imaginary parts Berenger modes are quite large, which indicates that those modes have a very large propagation loss. However, those modes are critical in MMM to match the boundary conditions. we can implement a MMM to investigation the excitation problem in which the light is coupled from a straight waveguide to a waveguide bend structure. Figure 3.12 shows a straight-bend-straight waveguide structure consisting of two straight slabs connected by an aforementioned 90° bend with fixed radius 50 μm in this simulation. With two mode sets from the bending and the straight structures, respectively, the propagation mechanism in the straight-bend-straight structure can then be analyzed with MMM involving two interfaces (AA' and BB' in Figure 3.12.)

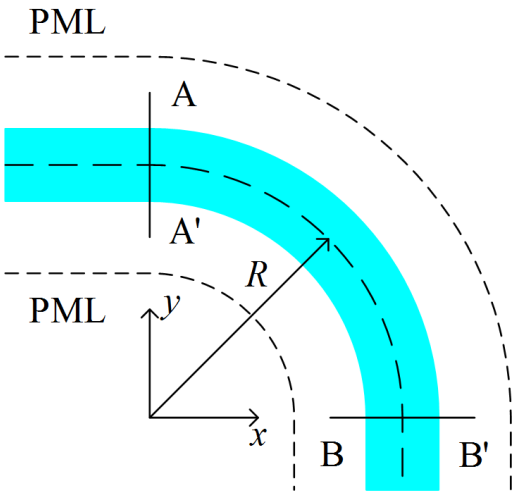

Figure 3.12 Straight-bend-straight geometry with PML. The radius of bending is 50 μm and the bending angle is 90 deg. TE fundamental mode is launched along +x direction in top straight waveguide.

We launch the TE fundamental mode operating at 1550 nm at the AA'-plane in the *x*-forward direction. The transmitted field is calculated at the BB'-plane. The field mismatch error has been calculated and is plotted in Figure 3.13. IMMM again shows a faster convergence speed than CMMM. In Figure 3.14, the converged transverse-electric field intensity distribution in the cross-section at the BB'-plane determined from CMMM and from IMMM when N=56 is compared with FDTD result. It shows that with 56 modes employed, both CMMM and IMMM represent the field distribution very precisely in both the guiding-layer region and the outer- cladding region. However the IMMM is more effective in representing the TE field distribution in the inner-cladding region.

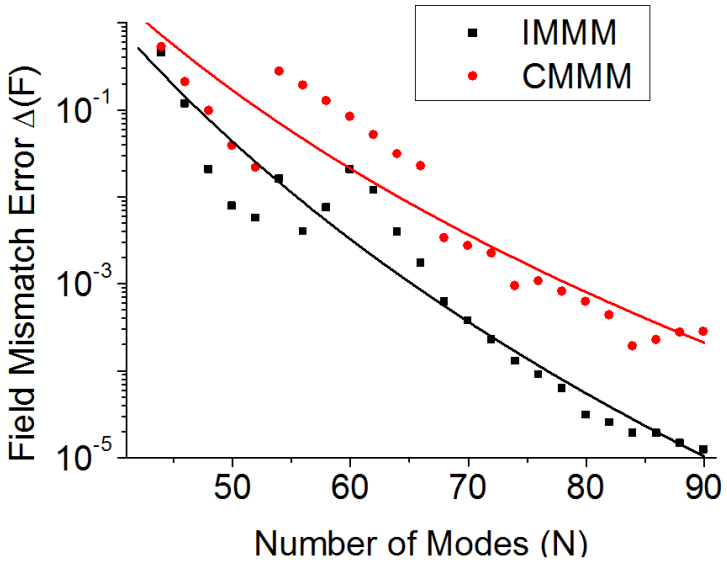

Figure 3.13 Field mismatch errors as a function of the total number of modes involved in MMM at the BB'-plane for both IMMM and CMMM.

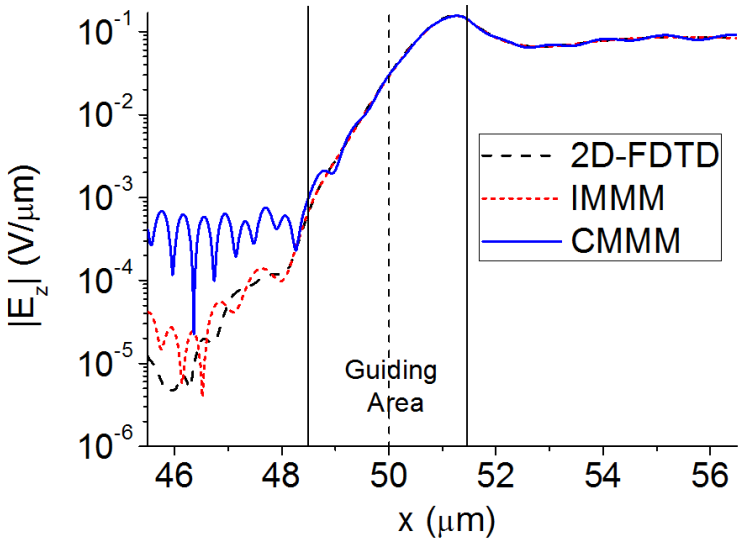

Figure 3.14 The converged transverse electric field intensity distribution in the cross section at BB'-plane from CMMM and IMMM with 56 modes is compared with FDTD

result. IMMM shows a better convergence than CMMM. Here *x* is the Figure 3.12 horizontal coordinate along BB' plane.

When different radii are applied in the simulation, the output modal coefficient excited at BB' plane by the single mode input at AA' plane is shown in Figure 3.15. It can be observed clearly that when the bending radius becomes smaller, high order leaky modes have been excited and this information can work as a guideline to choose how many modes should be included in the propagation problem, as the bending leaky modes are all with small absorption coefficients.

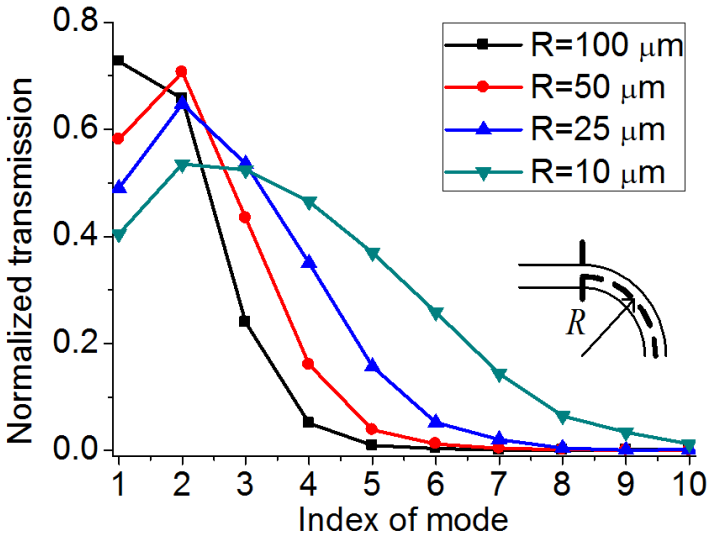

Figure 3.15 Transmission coefficients of excited bending modes with different radii. Higher order leaky modes are excited as radius reduces. Inset: Straight-bend structure. Forward fundamental TE mode in straight waveguide is launched to excite bending modes.

In general, for modes in bending waveguide structures with very small bending radii, as the radius reduces, guided modes disappear and high order leaky bending modes are generated. Through the complex MMM for the excitation problem in straight-bend structure, we find that with smaller bending radius, higher order leaky modes will be excited and contribute to the energy transfer significantly. The higher order Berenger modes are essential in the scattering field simulation at the interface, though they contribute little in the transmission problem.

3.6 IMMM with WOPD

In this section, two major progresses in complex MMM are reviewed and tested with a germanium photo-detector structure: reformulation of MMM without applying modal orthogonality, i.e., IMMM; weighed optical path distance method in complex mode calculation, i.e., WOPD. Figure 3.16 shows Ge-photo-detector integrated with SOI structure. The fundamental mode in SOI slab is excited and the energy will be led into the Ge layer. Here we want to simulate the field distribution at the interface. The refractive indies for Si, Ge, and silicon dioxide are 3.47, 4.1, and 1.44, respectively. The computation window before truncation is 1.22 μm including 220nm thick Si slab and 500 nm Ge substrate and 500nm SiO_2 substrate. The PML's thickness is 2μm, For the SOI part (z<0), the reflections of PMLs in substrate and cladding are both 0.01, while in the Ge-photo-detector region, if we use unadjusted optical path distance (UOPD), the PML reflections are the same as SOI, or in the weighted optical path distance (WOPD) case,

the reflection of PML in cladding keeps 0.01, and following Eq.(2.20), the one in substrate should be 0.198.

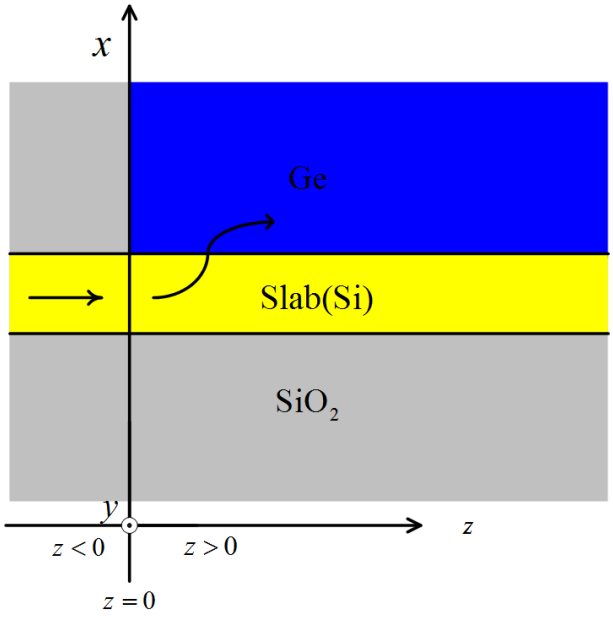

Figure 3.16 Germanium photo-detector integrated with SOI structure. The TE light is launched from a silicon slab waveguide along +z direction and is coupled into a germanium photo-detector.

The field mismatch error as a function of number of modes in MMM, *N*, is plotted in Figure 3.17 for 4 cases – CMMM or IMMM with UOPD or WOPD. With more modes, mismatch error should converge to 0, which is observed for 4 cases in Figure 3.17. Besides, compared with the CMMM under UOPD case, through no matter applying the IMMM formulation, or modifying the PML as WOPD, the curves shows faster convergence speed, and at *N*=100, the mismatch error diminishes as about tenth for both CMMM with WOPD and IMMM with UOPD. One interesting phenomenon is in this case, IMMM and WOPD seemingly bring same level improvement for MMM, which

however is just a coincidence. Though the two techniques can both improve the convergence speed of field mismatch error against *N*, the effectiveness may vary with the structures. Further, in the case with both IMMM and WOPD, the mismatch decreases fastest as expected. In addition from Figure 3.17, with the same MMM formulation, WOPD's data are better aligned with the fitting line, while in the UOPD case data fluctuates seriously, especially for CMMM. This is because in UOPD case, two kinds of high order complex Berenger modes coexist and two matching trends are mixed together. Through simulations in Figure 3.17, we can conclude that IMMM and WOPD can both yield smaller field mismatch error at fixed number of mode, which means improvement with higher computational efficiency.

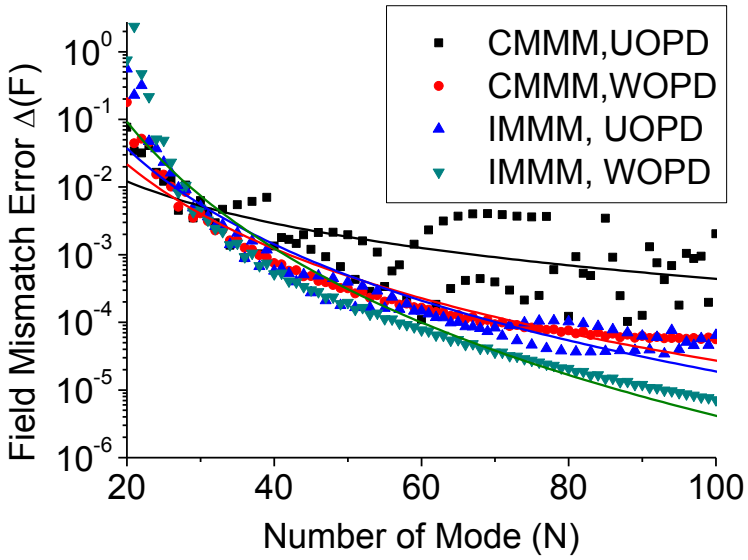

Figure 3.17 Field mismatch errors as function of total number of modes for CMMM/IMMM with UOPD/WOPD

To illustrate the accuracy of the new MMM simulation techniques, we compare the field at the interface from MMM with the one from 2D-FDTD results as in Figure 3.18. In 4 cases, the MMM results converged to FDTD ones as more modes are applied. Similar conclusions for Figure 3.17 can also be drawn for Figure 3.18. Figure 3.18 not only proves the accuracy for MMM with WOPD or IMMM, but also shows that with fixed number of modes, WOPD and IMMM can improve the simulation efficiency.

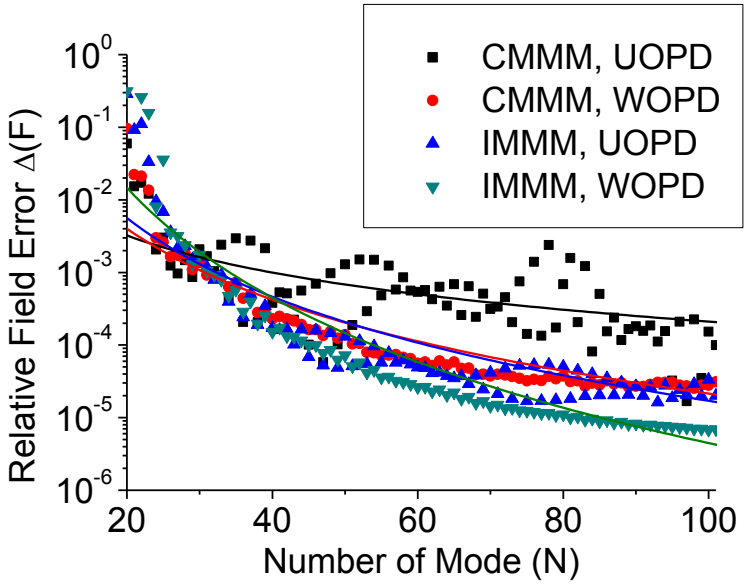

Figure 3.18 Field errors compared with FDTD results as benchmark as function of total number of modes for CMMM/IMMM with UOPD/WOPD

3.7 Conclusion

In this chapter, we revisited the MMM and proposed an improved implementation which yields a faster convergence speed and smaller field mismatch error. With a fixed computation effort including a truncation window along with PML thickness,

discretization step and mode number, our proposed method shows a significantly smaller field mismatch error and is insensitive to the PML's reflectivity. For structures with strong radiation effects where strong-absorption PMLs are utilized, the IMMM shows distinct advantages over CMMM in terms of accuracy and efficiency. With detailed numerical studies, we have validated this improved method through three simple examples: propagation through an SOI waveguide facet, propagation around an 90^{o} waveguide bend and wave propagation in germanium photo-detector structure. For all these reasons, this new method shows great promise in photonic integrated circuit simulation and analysis. With the assistance of improved MMM, the roles of high order bending modes are studied, after a profound investigation on mode transition under different bending radii, concluding that leaky modes emerges as radius reduces, and play key role in transmission, while high order Berenger modes are of significance in field expansion and radiation field representation. The Ge photo-detector example shows the possibility of cooperation of IMMM and WPOD, forming the most efficient simulation method for MMM algorithm.

Chapter 4.

Hybrid Plasmonic-Photonic Nano-Ribbon Waveguide Design

4.1 Introduction

Silicon channel waveguides are widely used in the on-chip light routing, and are one of the basic structures in silicon photonics circuit. Through doping, depositing and bonding processes to combine heterogeneous materials or structures with the simple silicon channel waveguides, various special waveguides can be realized for customized utilizations. Through modal analysis, we can find out the propagation constant, indicating the propagation velocity, and the loss coefficient, as well as the field distributions showing power concentration or confinement. In this chapter, a special waveguide – hybrid plasmonic-photonic nano-ribbon waveguide, also called hybrid photonic slot/surface-plasmon-polariton (HSSPP) waveguide is investigated, and the fundamental

mode, TMo mode, is achieved with an FEM based complex mode solver under the frame with PML and PRB. Though for the guided mode itself, mode solver with PRB without PML seems sufficient, we still apply the complex modal analysis with PML, and the reason is as the size of waveguide shrinks, the guided mode will approach the cut-off condition and then become very leaky. In such cases, electro-magnetic field will tend to expand in a large space area, and then the reflection from simple PRB box discretization will lead to reflections interfering with original fields. With the PML, we can handle those modes with a relative small simulation window, enhancing the simulation accuracy and efficiency.

The hybrid plasmonic-photonic nano-ribbon waveguide is actually a marriage of "Gap plasmon" waveguide, and the dielectric slot waveguide. "Gap plasmon" waveguides emerged a decade ago[92] referring to surface plasmon polariton (SPP) propagation in a metal-insulator-metal channel waveguide – also called conductor-gap-conductor or CGC waveguide. Two metal strips were separated by a nano-scale gap filled or partly filled with dielectric, giving strong SPP localization in the direction perpendicular to the gap. Later, the definition of "gap plasmon" became broadened to include asymmetric structures of conductor-gap-dielectric (CGD) in which only one metal strip is present and where the "gap" G is a low-index dielectric layer, while "dielectric" D is a higher-index intrinsic semiconductor such as Si or Ge [93]. In CGD, the TM-polarized SPP propagates at the boundary between the conductor and the low-index dielectric [93]. This SPP mode guidance does not employ internal reflection at the

low/high dielectric interface. The literature reports several examples of strip-shaped metal-gap-silicon CGD waveguides [94]~[96].

As early as 2007, a symmetric five-layer slab waveguide, similar in a generic way to the strip waveguides presented in this chapter, was introduced by Adato and Guo [97] for the purpose of ultra-long-range SPP propagation. Their 5-layer had metal buried at mid-plane and their stack is characterized exactly as DGCGD where the long-range mode is symmetric with respect to the metal. There are two equivalent ways to describe the 5-layer SPP waveguide. One way is talk about the two plasmonic gaps that are present in the structure, and the other way is to describe the "metalized photonic slot" in the structure. There are two metal/low-dielectric interfaces in their 5-layer and hence two gaps, each having a 1.48 index [97]. The metal was an Au or Ag or Cu film with 20 nm minimum thickness. Dispersion curves and SPP mode cutoff conditions were presented there. The Si-based dual-gap waveguide was updated and optimized in the paper by Bian and Gong [98] who examined both horizontal and vertical geometries at $\lambda = 1.55$ μm. In lieu of gap terminology, they chose to describe the structures as a hybridized photonic slot –specifically a low-loss "silicon nano-slot-based symmetric hybrid plasmonic waveguide." This hybrid category [99] has become an important research and development area [100][101].

The silicon photonic slot waveguide was discovered about a decade ago [102]. That structure has a low-index nano-scale dielectric slot between Si strips, a slot containing air or SiO2 or polymer. The TM mode polarization was required for modal field enhancement in the slot, just as required in our design. In fact, we have modified this

slot-in-Si. We have chosen to insert a thin metal ribbon in the mid-plane of this slot. The TMo mode is a hybrid combination of plasmonic and photonic guidance.

For the 1.55-μm hybrid channel waveguides of [98], propagation lengths of ~ 1 mm were predicted for certain choices of "half slot" thickness and metal ribbon thickness. We have made significant extensions of the prior work by: (1) investigating wavelengths of operation well into the mid infrared, from 1.55 μm out to 8 μm, (2) changing the waveguide body layers to germanium after analyzing silicon, (3) changing the SiO2 gap material to silicon nitride which has a wider MIR transparency range, and (4) studying partial cladding of the waveguide core by air and comparing that performance to the results of all-around nitride cladding. In the prior Bian-Gong work [98] it was found that the thickness of the metal ribbon must be extremely small for good results on propagation length. That choice was carried through in this paper. We selected a copper ribbon thickness of 10 nm which is the minimum value that preserves electrical conductivity and avoids holes in the metal film. Copper is said to be compatible with CMOS processing, although there are some issues with Cu diffusion, and aluminum is perhaps a less controversial choice. The undoped intrinsic semiconductor body layers are termed "dielectrics" in the language of plasmonics, although N and P doping is surely feasible to transform the waveguide into an active electro-optical device.

This chapter is organized as follows. Using the FEM as the electro-magnetic mode solver, the fundamental TM-mode of Si and Ge nano-wire-ribbon waveguides is investigated over 1.55-8.0 μm. A systematic study of gap thickness and wire cross-section was performed and some unexpectedly long propagation lengths of several centimeters

were found at mid infrared (MIR), unprecedented in the prior plasmonic art. Semiconductor "wires" of width W and overall thickness H were studied. Specifically, we predicted well-confined low-loss wires with cross-section W x H around 0.7λ/n x 0.7λ/n, with most mode energy in a $\lambda^2/400$ area. By shrinking W and H further, very low loss was attained at the expense of considerable mode fringing into the cladding. As mentioned, the present mode is believed to be a new kind of hybrid mode [99] related to the photonic mode that propagates in a low-index nano-slot placed within an intrinsic semiconductor strip. The present mode combines metal-related surface-plasmon-polariton (SPP) guiding with photonic-slot concentration. The present hybrid slot/SPP waveguide (HSSPP) had lowest propagation loss when it was clad all-around by Si3N4, indicating that an "embedded wire" approach is best. Thus a "nano-circuit" network would be embedded. Examination of the Ge wire case indicated that the propagation lengths are "long" by SPP standards but are less than those in hybrid Si wires.

4.2 Results of numerical simulations on hybrid slot /SPP waveguides

Figure 4.1(a) and (b) illustrate perspective views of the silicon-based infrared channel waveguide: the air-clad silicon-on-nitride channel and the channel embedded completely in Si3N4. Both are expected to be compatible with CMOS processing. Figure 4.2 shows a cross-section view of the two structures investigated here, where the thickness of the "buried" metal ribbon is fixed at 10 nm, regardless of the wavelength chosen, meaning that this film thickness goes from λ/155 to λ/800 as the wavelength increases from 1.55 to

8.0 μm. There are two Si3N4 layers or "gaps" of thickness t that surround the Cu film. If we were to remove the metal, we would have a t + t photonic "slot". There are two equivalent ways to describe the Figure 4.2 waveguide: (1) a buried-ribbon dual-gap plasmonic waveguide, (2) a hybrid slot/surface-plasmon-polariton (HSSPP). The HSSPP descriptor is selected here.

In the following simulations, Si3N4 is used for the gap layers, for the Si substrate "cover" and for the cladding. Its refractive index is constant at 1.98 over the wavelength range. We assume that the refractive index of the polycrystalline form is the same as that of the crystalline form for both Si and Ge. The refractive indices for crystalline silicon and germanium channel structures—including the λ-dispersion—are given in [103]. For the metal layer, the index of Cu can be expressed as $n_{Cu} = n_{Cu}^{r} + in_{Cu}^{i}$ and both the real and the imaginary parts can be found in [104].

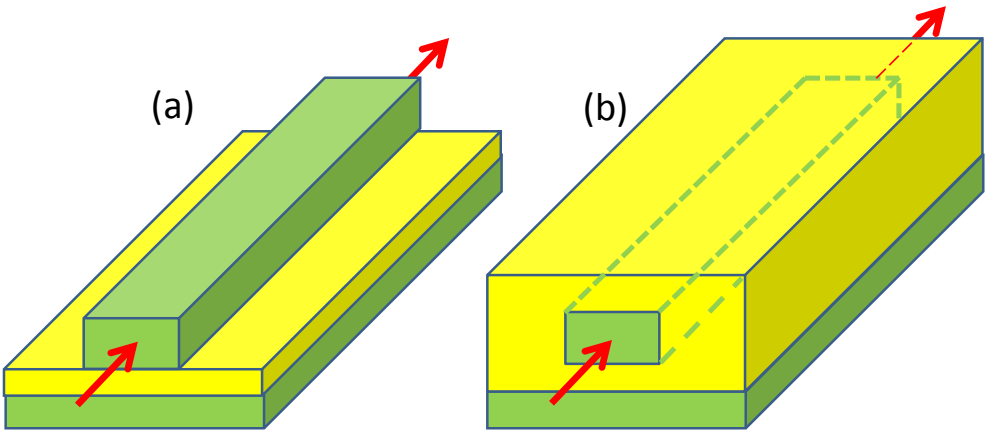

Figure 4.1 Two approaches to infrared channel waveguides built upon a "silicon-on-nitride" chip: left drawing (a) has the Si channel clad by air above the nitride layer; right

drawing (b) has the channel embedded completely or clad-all-around by Si3N4. Here green represents silicon and yellow denotes Si3N4.

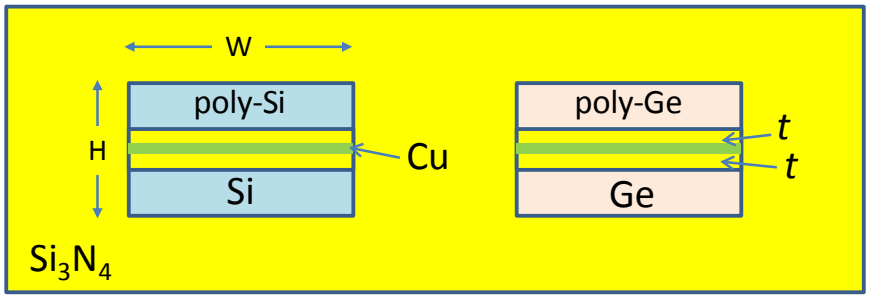

Figure 4.2 Cross-section view of the hybrid slot/surface-plasmon-polariton (HSSPP) waveguide built within a Si channel (structure at left) and in a Ge channel (structure at right). The thickness of the buried metal ribbon is fixed at 10 nm. There are two Si_3N_4 layers or "gaps" of thickness t that surround the Cu film. We can think of t as the "half slot" thickness.

4.2.1. Effect of waveguide cladding materials and location

A realistic approach to understanding the effect of wavelength change is to scale both dimensions W and H with λ: in particular, we took from the silicon telecoms practice W = 0.4λ and H = 0.2λ for initial simulations. Then the TMo effective index n + i k of the Si hybrid channel was determined at λ= 3 μm for the following four cases: (1) the Si3N4/Si substrate of Figure 4.1(a) with air cladding, (2) the all-around Si3N4 cladding of Figure 4.1(b), (3) air cladding all around, and (4) SiO2 cladding all around. The results for cases (1) and (2) are presented in the simulation results of Figure 4.3(a) and (b), respectively, for t = 20 nm and 10-nm Cu. Summarizing our four results, we found in four cases the following effective real indexes: (1) 2.27, (2) 2.47 (3) 2.04, and (4) 2.22. The imaginary

effective index (the k extinction) was also determined and this can be expressed as the propagation loss in dB/cm as $4.34x10^4$ $(4\pi/\lambda)k$ as follows for our four cases: (1)1062, (2)29.0, (3)44.6, and (4)37.5 dB/cm. A rather dramatic difference was found. The explanation for this comparative loss response is traced to the geometric symmetry of the waveguide cross-section structure. The symmetric structures of cases (2), (3) and (4) ensure low loss [97], whereas the "broken symmetry" of case (1) leads to high loss. In subsequent simulations, because of favorable symmetry, we limited ourselves to the Figure 4.3(b) scenario. The metal thickness is 10 nm throughout the paper.

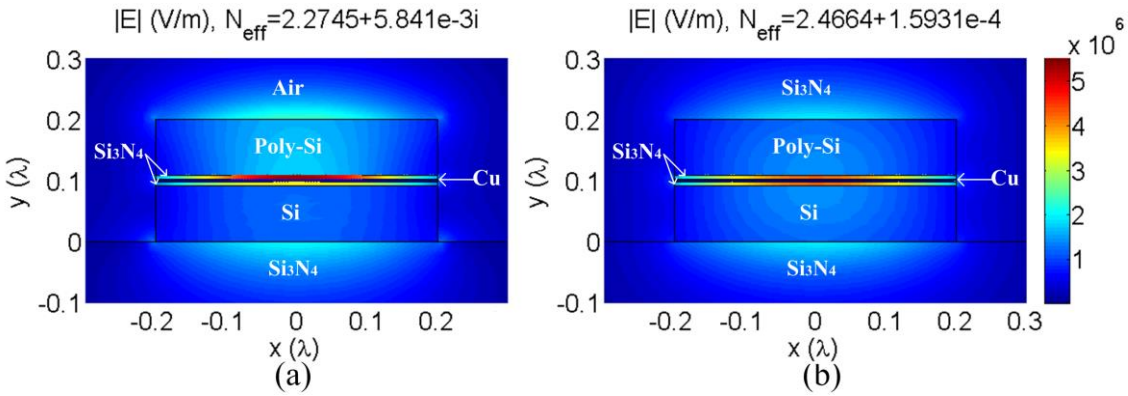

Figure 4.3 Electric field distributions for HSSPP modes in Si channels with (a) air cladding and (b) all-around Si3N4 cladding. W x H = 0.4λ x 0.2λ, with λ = 3 μm, t = 20 nm, and Cu = 10 nm. The complex effective index is listed at the top. Field strength is shown in false color; the width dimension is x, and the height dimension is y

4.2.2. Relevant physics background for modeling

We can set the stage for simulations by examining some waveguide physics that applies here. Waveguide physics results for the five-layer HSSPP slab system have been

presented [97] and offer us guidelines for attaining long-range SPP propagation—the main features that we should "expect in advance" for the channel case. First, the waveguide layering must be symmetric in the vertical direction. Second, the half-slot dimension t must be on the nano scale. Third, there is an upper limit on t that must be avoided because at that dielectric height the mode "loses its attachment" to the metal. Specifically, when the TM mode attenuation is plotted against the "gap" thickness t (at a given gap index), then there is a definite critical thickness t_{cut} defined as the t-value at which the long-range SPP mode becomes cutoff. The interesting feature (see Figure 3 of [97]) is that the attenuation becomes dramatically weaker (and the 1/e-intensity propagation length L becomes much longer) as t approaches t_{cut}. This behavior is seen clearly in our simulations in section 4.2.4 below. What happens physically with increasing t is that the mode volume expands along y with a greater portion of its energy in the dielectric, producing lower loss. A second aspect of the cutoff thickness is its dependence upon the index contrast between the high- and low-index regions (between semiconductor and insulator) with [97] showing that the larger that index difference, the smaller is t_{cut}, and thus with a fixed t, the attenuation will be smaller due to smaller t_{cut} - t. We have verified the importance of this physics guideline in section 4.2.5

Another relevant-physics aspect of the hybrid mode is related to the metal because mode loss is strongly linked to the metal. There are two aspects: the mode penetration into the metal and the wavelength dependence of the metal's permittivity $\varepsilon_1(\lambda) + i\varepsilon_2(\lambda)$. Plasmonic theory shows generally that mode loss is proportional to $\varepsilon_2 / (\varepsilon_1)^2$. The physical $\varepsilon_1(\lambda)$ and $\varepsilon_2(\lambda)$ properties of Cu in the mid infrared predict a decreasing loss with

increasing wavelength, and this is what we find. To be specific, we calculated the dispersion of mode loss for the structure with W=0.4λ and H=0.2λ at fixed t=20nm and we found that the attenuation decreased from 0.02 dB/μm at 1.55 μm to 0.001 dB/μm at 8 μm. Therefore the known metal-linked dispersion relation supports our HSSPP mode. Tight confinement of light at/near the metal also produces here the expected penetration-linked effect as detailed below.

4.2.3. Effects of W and H upon L

Keeping t again constant at 20 nm, we examined the effect of widening the channel W when keeping H fixed at a particular value. Both W and H were expressed in terms of λ. Results for L at λ= 3μm and λ= 6μm are presented in Figure 4.4 for the silicon case. As shown in Figure 4.4 the propagation length drops as W increases because the propagation loss is proportional to the width of metal "exposed" to the light field. Also, the L-decrease slows down with the increase of W because the modal field width will not increase linearly with the increasing waveguide width. A somewhat surprising Figure 4.4 result is that the predicted L became several centimeters when both W and H were chosen in the sub-wavelength range of 0.1 to 0.2λ. The interpretation of these results is given in section 4.2.7 below. The next simulation was to hold W fixed and to vary H for the same devices, and the results are shown in Figure 4.5 for both the λ = 3μm and λ = 6μm situations. Once again, the same dramatic increase of L when H moves below 0.2λ is found, with L rising into multiple-cm lengths.

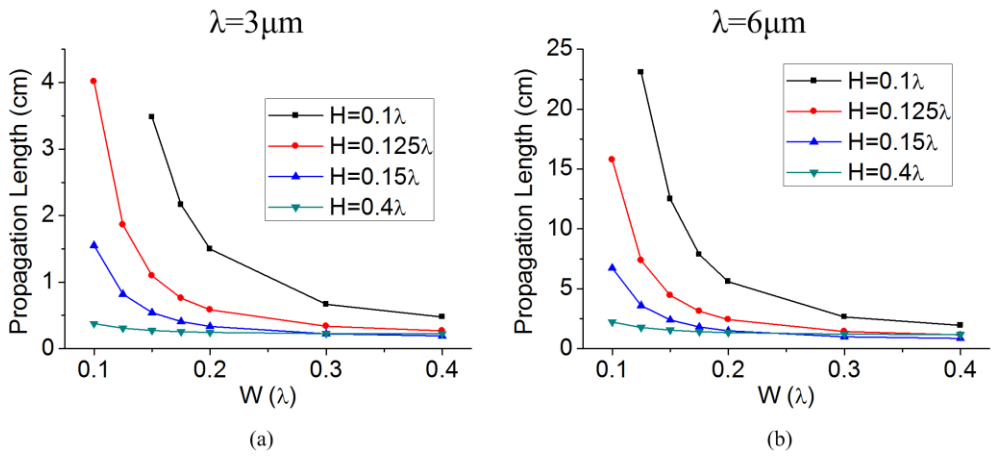

Figure 4.4 L versus W of the Si channel with different fixed heights at the wavelength of: (a) 3μm, (b) 6μm using t = 20nm.

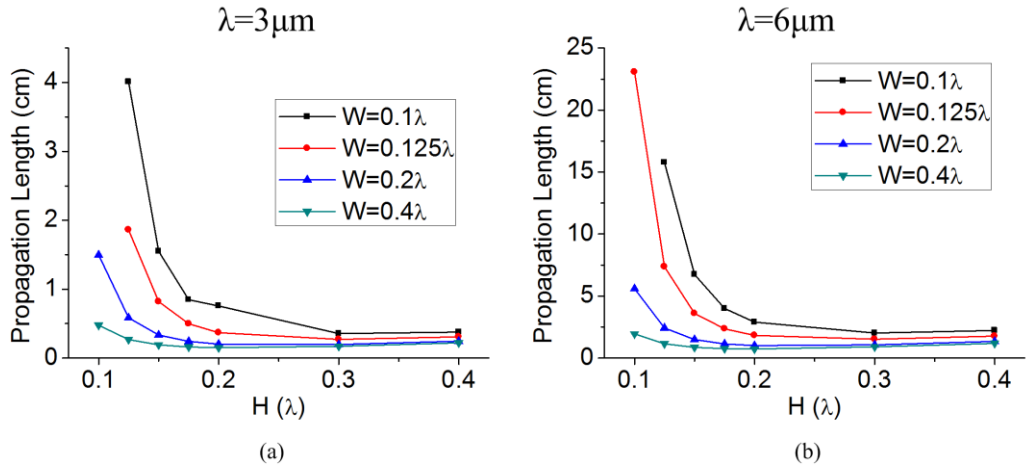

Figure 4.5 L versus H for the Si channel with different fixed widths at (a) λ=3μm, (b) λ=6μm using t = 20nm.

4.2.4. Influence of the gap-layer thickness upon L

We studied this t-dependence by choosing the 3 μm wavelength for the Si channel with W = 0.10λ and H = 0.15λ. The results are shown in Figure 4.6 where it is found that an increased gap distance produces lower propagation loss. The propagation length increases

12x at t = 50 nm. As discussed in section 4.2.2, the increasing t in Figure 4.6 brings t close to t_{cut}; consequently the mode loss decreases with t increase. However, at the larger t values in Figure 4.6, the mode becomes easier to cut off for a given size of channel.

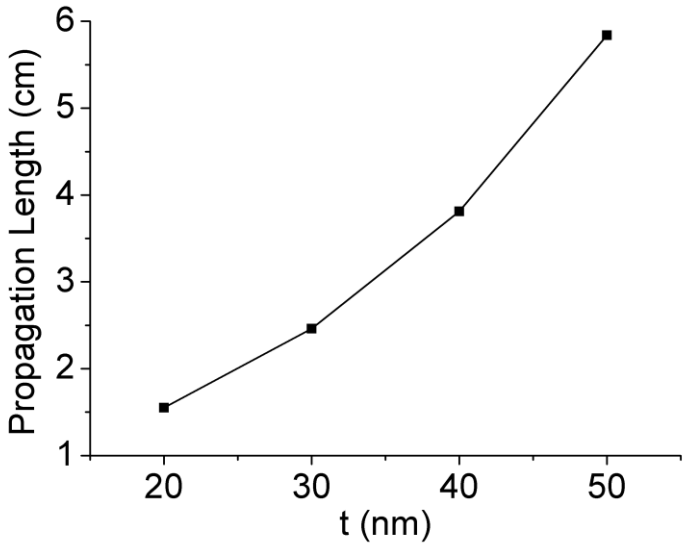

Figure 4.6 L versus t in a silicon HSSPP structure with W = 0.1λ and H = 0.15λ at λ = 3 μm.

4.2.5. Influence of the gap material's refractive index upon L

Silicon-on-insulator, silicon-on-sapphire and silicon-on-nitride are three "mainstream" MIR photonic waveguides with relevance to plasmonics. That's why we investigated the use of SiO2, Al2O3 and Si3N4 as gap materials in the HSSPP structure. Again using λ=3 μm as a test case, we took for Si the gap t = 30 nm with W = 0.1λ and H = 0.2λ, and we compared the resulting propagation length in the three cases. As shown in Figure 4.7, we found that the lower the gap refractive index, the larger the L. The physical explanation for this result is given in section 4.4.2.

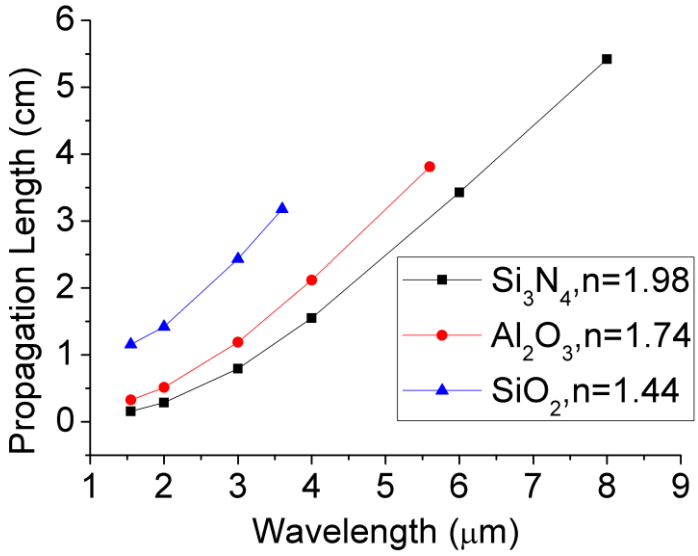

Figure 4.7 L versus λ for Si HSSPP structures having different gap materials: SiO2, Al2O3 and Si3N4. We used λ = 3 μm, t = 30 nm, with W = 0.1λ and H = 0.2λ.

4.2.6. Simulations of the Germanium HSSPP waveguide

In order to connect the predicted behavior of a germanium HSSPP channel with the previously derived silicon results, we selected geometric conditions for Ge that were the same as those used in Figure 4.4 and Figure 4.5 above, namely: λ = 3 μm, t = 20 nm, with Si3N4 for both gaps and cladding. First H was fixed and the variation of W was looked at as shown in Figure 4.8(a). Next W was fixed with H variable as presented in Figure 4.8(b). For those cases, the calculated Ge propagation lengths are presented. As in silicon, when W is taken below 0.2λ, approaching 0.1λ in Figure 4.8(a), and when H goes below 0.2λ towards 0.1λ in Figure 4.8(b), then L rises evidently, even into the centimeter range. (The high-L interpretation of Figure 4.8 is also offered in section 4.2.7.) Generally, the silicon L is about 50% larger than the germanium L. Because of Ge's higher index,

the semiconductor dielectric trapping is stronger in the Ge case of Figure 4.8 than in the Figure 4.3(b) Si case. In Ge waveguide, the slot has a greater percentage of the mode, which explains the lower-than-Si L.

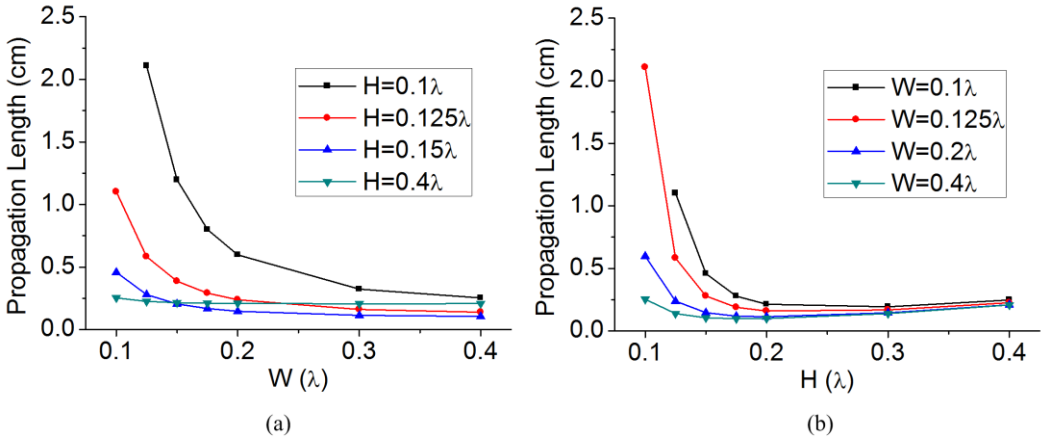

Figure 4.8 L versus (a) W of the Ge channel with different fixed H; (b) H of the Ge channel with different W at λ = 3μm with t = 20nm.

4.2.7. Mode profile as a function of the W, H geometry

In this section, we interpret the long range HSSPP results revealed in Figure 4.4， Figure 4.5， and Figure 4.8 and we highlight the tradeoff that long-range operation requires. Figure 4.4， Figure 4.5， and Figure 4.8 also show results of HSSPP propagation at millimeter lengths and those waveguide geometries of W and H are believed to be practical; they do not require much tradeoff. We begin by looking at the mode profile illustrated above in Figure 4.3(b), and we consider the y direction. The y-distributed mode found in Figure 4.3(b) is an eigen-solution of Maxwell's equations with an associated eigenvalue (the mode effective index). It is not the superposition of three distinct modes.

It is one mode with light "accumulated" in several regions. The mode has energy in the upper nitride cladding, the upper semiconductor strip, the double-gap, the lower semiconductor strip and the lower nitride cladding. When L is greater than 1 cm in Figure 4.4，Figure 4.5，and Figure 4.8, we want to know what percentage of the mode power is present in each of the five regions. To answer the question, we performed several simulations, two of which are presented below.

A qualitative answer to the question is that the mode expands into the nitride cladding, when W and/or H approaches 0.10λ, which means the mode power in the double-gap is relatively small. This signals that the mode is approaching cutoff in the cm-L cases. For applications, it is usually not good to have the optical field fringing into the cladding and going outside of the semiconductor strips. For that reason, the cm-propagation may have limited utility. However, the mm-L structures discussed are found to be well-confined in the semiconductor channel like the result seen in Figure 4.3 (b). Figure 4.9 (a) presents the mode profile under the same conditions as for Figure 4.3 (b) except that the height has been reduced from 0.2λ to 0.l25λ and the width was reduced from 0.4 λ to 0.1λ. Here we see that about 60% of the mode energy has been "forced" into the upper and lower "low loss" nitride claddings, with a resulting L of 4 cm. There is also some trapping in the upper and lower Si strips, but less energy resides there than in the claddings and double-gap area. While the propagation loss is very low in Figure 4.9(a), most of the "fringy" mode resides away from the plasmonic region. In other words, the large L arrives at the expense of a large mode. Looking now at Figure 4.4，Figure 4.5，and Figure 4.8, if we select W and/or H to be in the vicinity of 0.2λ rather than 0.1λ, then

L is typically millimeters and here the mode has very little cladding component as in Figure 4.3(b). Therefore, we judge those ~ 0.7λ/n choices of channel geometry to be practical. Generally L increases strongly with λ in Figure 4.4，Figure 4.5，Figure 4.7, and Figure 4.8

It is interesting to learn what happens in the high-aspect cases where H >> W. To illustrate this, we examined a "blade-shaped" channel waveguide, the Si channel with W = 0.05λ and H = 0.8λ at λ = 3μm having t = 20nm. The resulting mode is presented in Figure 4.9 (b). Once again, as in Figure 4.9(a), the mode in Figure 4.9(b) has expanded considerably into the surrounding nitride cladding, but now going in the lateral x-direction, and that mode enlargement is linked to the large L of 1.5 cm. The lateral fringing seen here may have value in the evanescent-wave side coupling of adjacent blade waveguides for directional coupling.

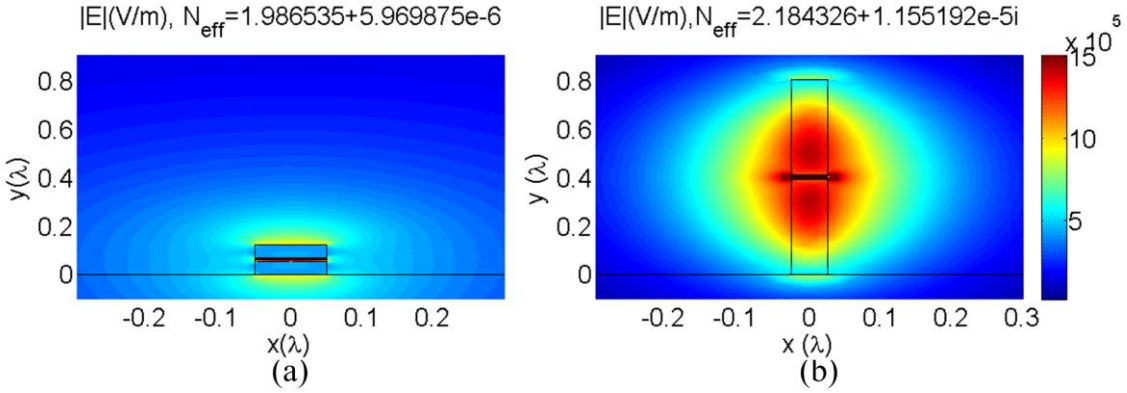

Figure 4.9 Mode distribution in Si channel at λ = 3μm, t = 20 nm with: (a) W = 0.1λ and H = 0.125λ; (b) W = 0.05λ and H = 0.8λ. In both cases, the five layers are: poly-Si, Si3N4, Cu, Si3N4 and Si.

4.2.8. Effect of ribbon width in a wide gap

A question not answered thus far is whether the hybrid mode clings closely to the metal ribbon, or instead fills both gaps irrespective of ribbon size. To illuminate this issue, we returned to the Si waveguide at the 3μm wavelength, and fixed the W at 0.4λ with H at 0.2λ and t = 20 nm. The TMo mode profile was derived for two cases of interest: one in which the ribbon width filled only 50% of the waveguide width, and the other with ribbon width of 0.25 W. These mode modeling results are given in Figure 4.10 and can be contrasted with Figure 4.3(b). It is found that the majority of mode energy does cling to the ribbon. However, there is noticeable leakage or fringing of light outside the ribbon "domain" and therefore an adjacent ribbon within the same gaps would experience some evanescent-wave side coupling.

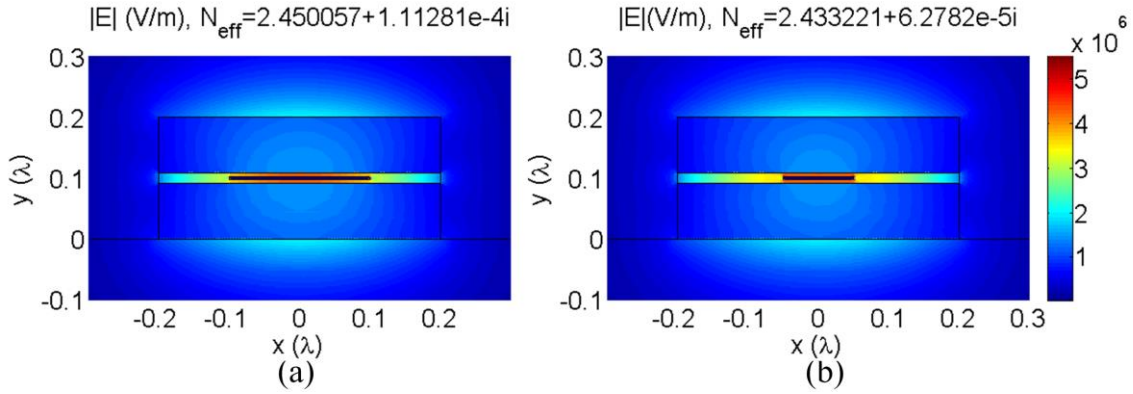

Figure 4.10 Electric field distributions for HSSPP modes in Si channels having different widths of the Cu ribbon: (a) 0.5W ribbon (b) 0.25W ribbon. Here W = 0.4λ, H = 0.2λ, t = 20 nm and λ = 3μm. The 10-nm ribbon is embedded in a 50-nm Si3N4 slot.

4.3 Discussion and summary

The plasmonic literature indicates that the mid-infrared region is a favorable spectrum for plasmonics because generally the SPP waveguide losses decrease there with increasing wavelength. The work in this paper confirms this theme and indicates a strong, consistent increase in HSSPP propagation length as wavelength increases from 1.55 to 8 μm while the waveguide cross-section is also scaled up. For the hybrid slot/SPP TMo mode, the 1/e mode-power propagation length L rises up into the multi-centimeter range when the Si or Ge channel width and/or the channel height is reduced down to the 0.3 to 0.4 λ/n range, where n is the semiconductor refractive index. This projected performance is really based upon the assumption of an ultra-thin metal film or "ribbon" buried within a low-index "gap" material of Si3N4 or Al2O3 or SiO2, and it is found that the lower the gap index, the larger are the values of L attained. The metal thickness was set at 10 nm as the lowest feasible value for electrical conduction (continuity) and void-free integrity of that film. It was also essential for the HSSPP channel to be clad all around by a rather thick, multi-micron coating of dielectric such as Si3N4. When an air cladding covered the top three surfaces instead of this dielectric, the propagation length became significantly shorter. Each of two gaps had a thickness in the 20 nm range, and an increase of gap thickness to 50 nm gave longer HSSPP propagation lengths. The estimated values of L for Ge were slightly smaller than those for Si. If the width of the channel waveguide is set at a value of λ/n, for example, it is possible to reduce the width of the buried ribbon to λ/4n and thereby to have a majority of the mode energy cling to the localized ribbon, while the

minority of energy resides in the metalless portion. In other words the ribbon is a local light-wire in the overall gap, although there exists infrared leakage around the ribbon that side-couples the narrow ribbon to nearby narrow ribbons.

The TMo mode in Figure 4.4， Figure 4.5, and Figure 4.8 closely approaches cutoff when the W, H dimensions of the Si or Ge waveguide are shrunk down to around 0.10 to 0.15 λ. The resulting expansion of the mode into the surrounding low-loss dielectric cladding thereby enables the propagation length to increase into the multi-cm domain. However, that mode size violates the "spirit" of mode confinement within the semiconductor channel. Hence the "smallest" waveguides may not be a good choice. Fortunately, there is a good compromise available. By selecting somewhat larger Si or Ge strip dimensions, W and/or H with values of 0.20 to 0.25 λ, the channel is expected to have good confinement (low fringing) as well as propagation at millimeter lengths. The W/H ratio influences the mode propagation loss and the ratio 0.5 has lower loss than the 2.0 ratio because the mode interacts with a smaller area of metal in the larger-H case. However, the aspect ratio alone does not determine reduction of the mode loss. That loss depends upon a combination of W and H values

Chapter 5.

Silicon-on-insulator Channel Waveguide with a $Ge_2Sb_2Te_5$ Self-holding Layer

5.1 Introduction

In this chapter, we embed a layer of phase changing material – $Ge_2Sb_2Te_5$ into the silicon channel waveguide to realize phase and loss modulation. We apply the complex mode solver to simulate the major guided modes to gain some guidelines for device designs. The phase-change material $Ge_2Sb_2Te_5$, commonly known as GST, is reported to have optical response superior to that of the other electro-optically interesting phase-change material vanadium dioxide (VO2) [24]. New applications are emerging in electrically controlled GST film for free-space optical filters and in GST film-loaded optical waveguides controlled optically by an external 700-nm light beam [105]~[107]. We, however, consider electrical control to be more suitable for practical applications than the

optical actuation. The thrust of this work is to combine electrical control with optical waveguiding by embedding a thin GST film between doped silicon waveguide strips in order to provide two useful transmission states for the channel waveguide. Those two self-sustaining states correspond to the amorphous and crystalline phases of GST. The resulting electro-optical devices are analyzed to predict the responses of the fundamental TE and TM guided modes in the near- and mid-infrared wavelength bands. The 10^{18} cm^{-3} P- or N-type doping proposed here provides adequate electrical contact to the film for Joule-heated phase change but does not decrease significantly the optical transparency of the waveguide.

The organization of this chapter is as follows. Electro-optical structures for 2 x 2 spatial routing (switching) and 1 x 1 modulations are proposed. The complex refractive indexes n + i k for both the amorphous and crystalline phases of GST in the 1000 to 2400-nm wavelength range are compiled via an extensive literature survey. Reliable index values are found for estimating switch and loss-modulator performance in several silicon-based structures wherein a localized "ribbon segment" of GST buried in Si or Ge serves as the active length of the modulator or switch. The substrate is assumed to be CMOS-compatible silicon-on-insulator (SOI). We also examined a photonic slot in the channel comprised of 1.96-index indium-tin oxide (ITO) and we considered the effect of two GST layers. The TE and TM behaviors are simulated and from that we determined spectral regions for switching and for step-wise modulation.

5.2 GST embedded waveguides

The recent experiments of Hosseini et al [108] presented a convincing demonstration of electrically induced phase change in a 7-nm film of $Ge_2Sb_2Te_5$. This layer was contacted above and below by doped ITO layers that provided electrical connection to the terminals of a voltage source. That source drove current pulses through the "resistive" phase change material. The resulting Joule heating of GST transformed its phase as desired for optical applications: in fact, the ITO was optically transparent at the wavelengths of interest as desired for electro-optical uses. In this chapter, we assumed that: (1) doped semiconductor layers or doped ITO layers contact the upper and lower surfaces of the GST film, (2) voltage across those layers is able to induce the desired thermal phase change via Joule heating current, and (3) the doped waveguiding materials are adequately transparent in the near/mid infrared for high transmission through the waveguide. What is proposed here is lightwave propagation in the plane of the GST layer as opposed to the normal-incidence transmission through the film used by Hosseini et al [108]. Because of multi-micron travel in the film plane, the guided mode here "senses" the GST complex index and responds to changes in index.

Experiments in the literature [105],[106] have placed GST upon an exposed surface of a waveguide where this GST layer acts as optical cladding so as to effect the relatively weak "fringing field" of the guided mode [109],[110]. Those papers demonstrated modulation and switching by means of a "pumping" light beam incident upon the cladding. The design presented here is new in two ways: (1) the thin film is placed

midway in the body of the waveguide where it has a much stronger effect upon the mode indices; (2) the phase change—rather than being optically triggered—is electrically induced. We are not aware of any prior art on electro-optical GST-core waveguides. A third new aspect of the present work is that we utilize both the electro-refraction and the electro-absorption component of the induced phase change. Another innovation here—in the context of electro-optical waveguides—is the "latching" or self-holding feature. Regarding prior electrical drive, there was a report of sandwiching VO_2 within a metallic "plasmonic" slot [109]. Also, a multi-micron length of VO_2 cladding was resistance-heated [110]. However, we are not aware of any electro-optical prior art in a phase change material photonic-waveguide core.

Our specific proposal for constructing the electro-optical waveguide is illustrated in Figure 5.1 where an active GST waveguide "segment" is end-fire coupled into and out of a uniform undoped channel waveguide. The SOI approach is selected in order to make this structure manufacturable and compatible with the silicon "CMOS photonics" industry. This device could also be germanium-on-insulator for wavelengths longer than 1.8μm. The Figure 5.1 insets, the cross sections, show the smooth transition between the undoped passive-channel sections and the doped active section. Insertion of the electro-optical region in this manner is expected to offer low insertion loss (IL), which will be calculated quantitatively at the end of section 5.8, yielding a 1dB IL at most.

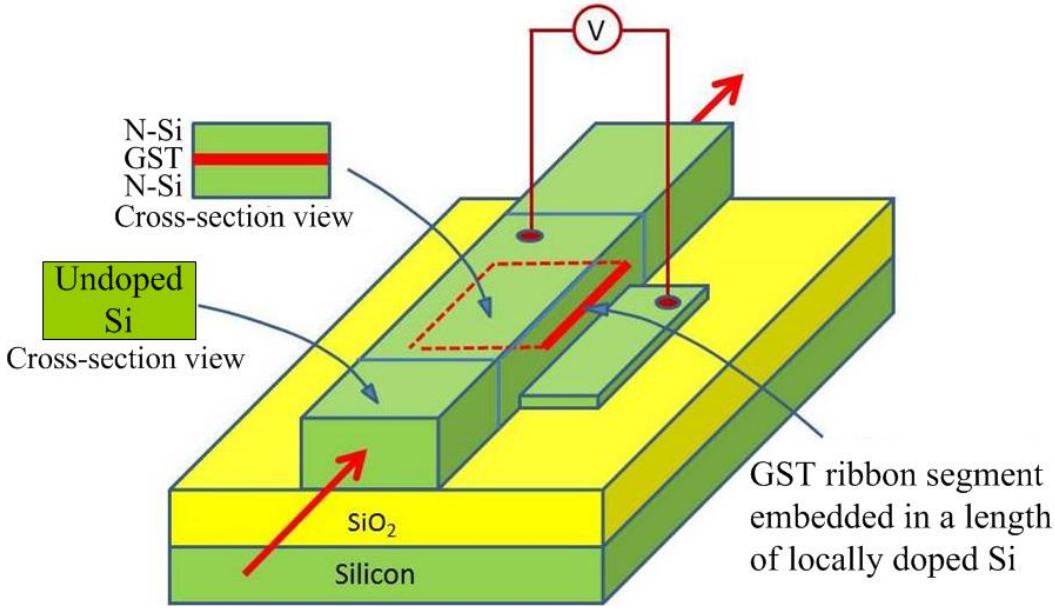

Figure 5.1 Perspective view of proposed 1 x 1 SOI electro-optical channel waveguide modulator employing a wavelength-scale segment of "buried" GST ultrathin ribbon

We investigated four approaches to layering thin-film GST within the channel as illustrated in the cross-sectional views of Figure 5.2. In the simplest case, GST is inserted at the mid-plane of the channel (Figure 5.2(a)). Here the GST would be sputter-deposited in the amorphous phase on a half-channel crystalline strip of doped silicon, after which a second half-channel strip of dense polycrystalline silicon, suitably doped, would be grown upon the GST. A bonded nano-membrane approach is an alternative fabrication technique. In Figure 5.2(a), the channel rests on the SiO_2-coated Si substrate with three sides of the channel exposed to air, whereas in Figure 5.2 (c) this channel is clad all-around by SiO2. A second electro-optical method is a five-layer technique: the GST is sandwiched between two very thin layers of doped ITO where this ITO/GST/ITO is located at mid channel, and the ITO/GST/ITO is sandwiched between doped silicon

layers to form Si/ITO/GST/ITO/Si (Figure 5.2 (b)). In effect, this produces two photonic slots related to the hybrid plasmonic slot explored in Chapter or in [19],[111]. A third way is a two-GST approach for making the electro-optical waveguide (Figure 5.2 (d)) wherein a single photonic slot is created. Electrically, the Figure 5.2 multilayers amount to several "resistors" connected in series, a path that brings current to the resistive GST. The electrical equivalent circuits in the above examples are either three resistors or five resistors. Layer thicknesses must be chosen for good optical performance. All four versions can be incorporated in Figure 5.1

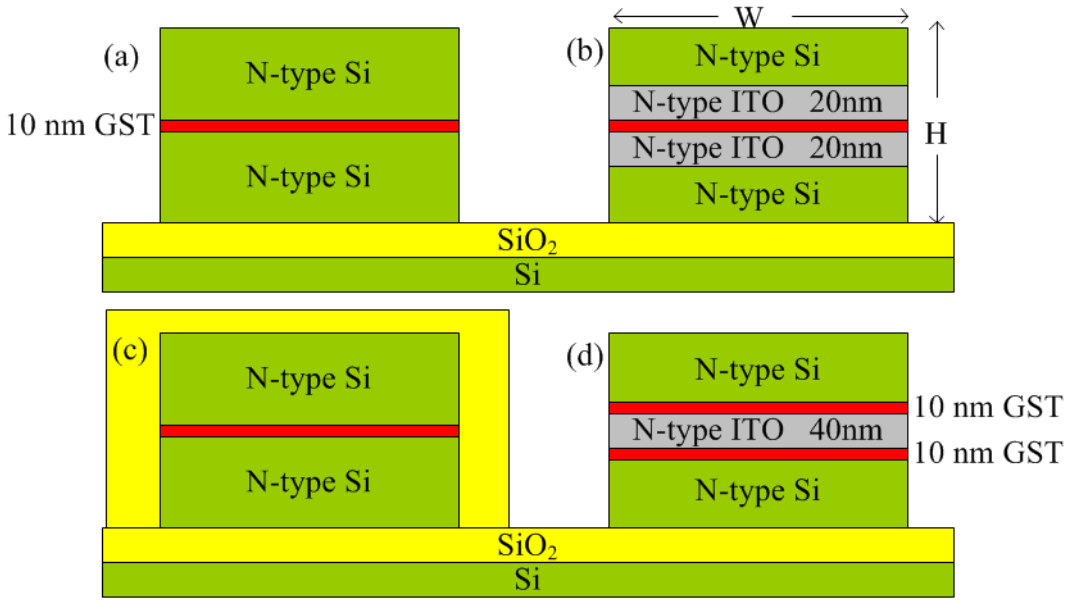

Figure 5.2 Cross-section view of four SOI electro-optical waveguide structures investigated.

5.3 Electrically induced phase change

In this section, we shall prove from a theoretical standpoint that the proposed structures can work properly. We considered the SiO2-embedded Si/GST/Si waveguide for the 2.1μm wavelength (10-nm GST, 205-nm doped-Si stripes). There are two related thermal procedures: re-crystallization from the amorphous phase to the crystalline phase, and the reverse – from the crystalline phase to the amorphous phase. In detail, the recrystallization requires an applied set voltage pulse of 100-ns duration as in [112] that induces temperature rise above 413K [113] but below 819 K (the melting point) [114]. The conductivity of GST in an initial amorphous state is small (0.1 S/m [115]), and without "stimulation" it is impossible to launch enough current to heat the layer to melting. However, when the electric field component of the applied voltage pulse is larger than a "threshold value", then the GST becomes conductive with no phase change [115]. To simulate re-crystallization, we assume that the applied field is above threshold, that the material starts to recrystallize, and that the GST conductivity has an average value of 1000 S/m during the 100-ns set time [112]. The actual process is more complex because the conductivity increases during "set" and the heating process is accelerated. Using COMSOL^{TM} software, we simulated the temperature rise induced by a 5V set pulse applied for 100 ns (E = 50 V/μm). Taking into account the thermal and electrical resistance circuits and the resulting current and electric power dissipation, the modeling yields the spatial distribution and time dependence of temperature rise. Here we found

that the current density finally reached 2.17 A/m^2 and the GST temperature rose to 420K in average during this time interval as required for recrystallization.

As for the changing process from crystalline to amorphous state, a shorter reset voltage pulse of typically 1 to 10 ns duration is employed, and there the GST film temperature must be raised above the melting point and then quenched rapidly by the pulse falling to zero in < 1 ns. This required annealing of the film is discussed in [116]. In our simulation, a 15V pulse was applied for 2 ns to the waveguided crystal GST having 2770 S/m conductivity [117], and here the result was a current density of 6.7 A/m^2 induced in GST. This produced a very strong temperature rise ~980K in the film (above the 891K as desired). In reality, after this "brief" melting, the latent heat of molten GST (1.37×105J/kg [115]) will consume most of the input power, pinning the temperature to the melting point and protecting the contact material. In summary, the electrically switched waveguide is indicated to work properly. The voltages that we applied in both simulations might be considered as "relatively high"; however, this is a trade-off we are willing to make to achieve optimum optical performances in the coming sections.

5.4 GST refractive indices versus wavelength

Before simulations can be started, it is necessary to have reliable values of the complex indices n + ik of GST. Partially crystallized or "fractional" intermediate states are not considered; only the amorphous and the rocksalt-structured crystal phases are examined. The four indices n_{am}, k_{am}, n_{cr}, k_{cr} have been plotted in various literature reports as a function of wavelength or of photon energy [121]~ [128]. We elected to use the

extrapolation from Shportko data for consistency [127]. The real part of refractive index and the extinction coefficients in our simulations are plotted over 1000nm to 2500nm as in Figure 5.3 and Figure 5.4.

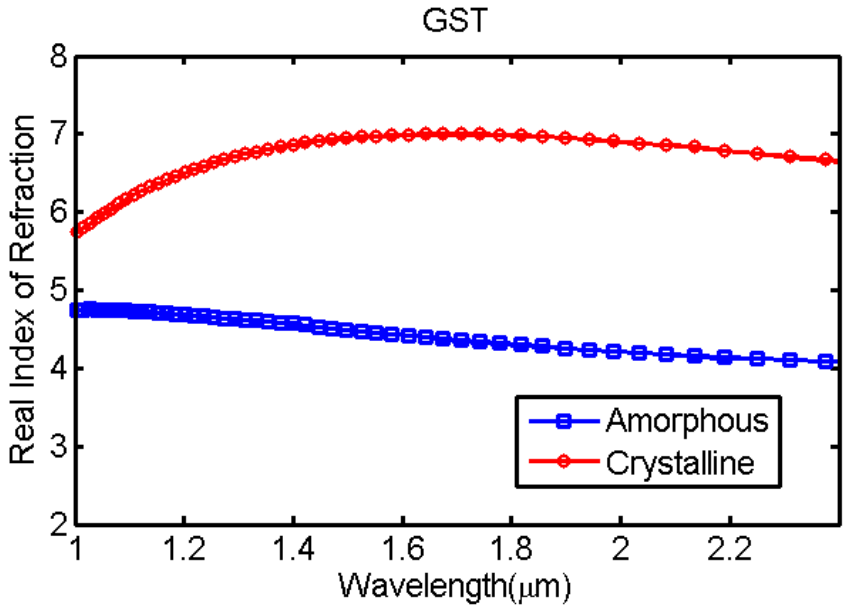

Figure 5.3 Wavelength dependence of the real refractive index components of GST.

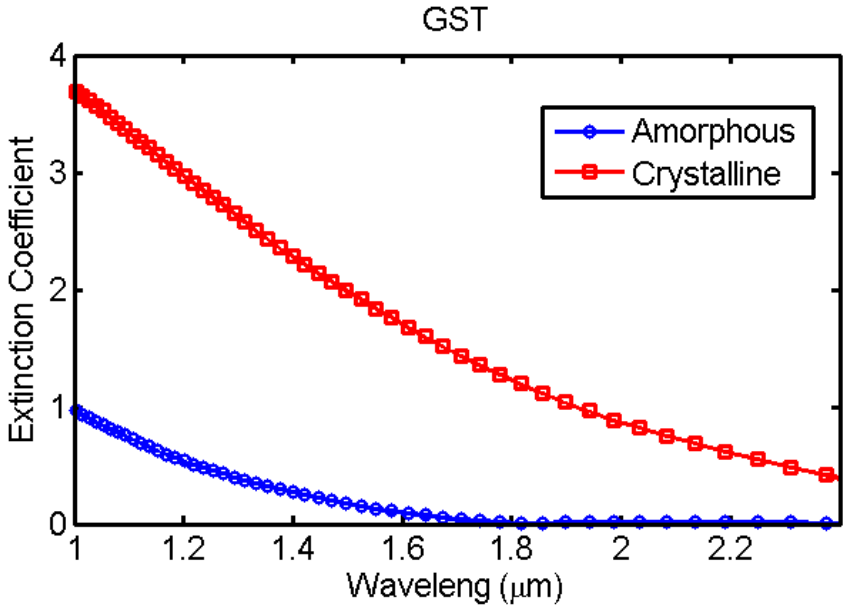

Figure 5.4 Wavelength dependence of the extinction-coefficient of GST

There is special interest in switching near 2000 nm because a new generation of hollow-core photonic bandgap fibers is being developed for operation in the 1900 to 2100 nm wavelength band [129] and such fiber transmission is central to increasing the information capacity of global fiber-optic networks. For applying electro-optical switching in this communications context, we considered the GST loss in Figure 5.4 in the 2000-nm region where k_{am} is decreasing rapidly. We selected λ=2100nm as being a compromise between missing the fiber-loss valley and attaining the lowest k_{am}.

The index values for doped ITO, Si, and Ge were estimated as follows. The N-doping of Si at 1 x 10^{18} cm^{-3} density produces k values in the 1 to 3 x 10^{-4} range according to [130]. For N-type ITO, a doping level of 5 x 10^{18} cm^{-3} was assumed. Then the size of both n and k in the 1.31-2.1 μm range was determined by scaling the 10^{19} cm^{-3} N-ITO index data presented in Huang et al [95]. All of the index values used in the simulations are tabulated in Table 1

Table 1 Values of the n and k indices that were utilized in the present simulations

Material	λ=1310nm		λ=1550nm		λ=2100nm	
	n	k	n	k	n	k
GST amorphous	4.68	0.33	4.60	0.12	4.05	0.006
GST crystalline	7.51	2.38	7.45	1.49	6.80	0.40
N-Silicon $10^{18}cm^{-3}$	3.50	0.0001	3.48	0.0002	3.45	0.0003
N-Germanium $10^{18}cm^{-3}$	---	---	----	----	4.09	0.0003
N-ITO $5x10^{18}cm^{-3}$	0.96	0.002	1.94	0.002	1.92	0.003

Silicon Dioxide	1.45	0.0	1.44	0.0	1.44	0.0

5.5 Performance guidelines for 2 x 2 switches and 1 x 1 loss modulators

Figure 5.5 shows the layout of two proposed 2 x 2 switches with the GST electro-optical segment shaded in orange where its active length is L. Each device has self-holding "cross" and "bar" states, states 1 and 2 that correspond to the two phases of GST. In each of its phases, the GST has a complex index of refraction, and the optical waveguide performance is linked to a change in both the real and imaginary indices. We can quantify optical performance using some definitions of indices and absorption. The GST indices are written for the amorphous phase $n_{am} + i\, k_{am} = n_1 + i\, k_1$, and for the crystalline phase $n_{cr} + i\, k_{cr} = n_2 + i\, k_2$, while the channel waveguide has a mode effective index in each state written as $n_{1e} + i\, k_{1e}$ and $n_{2e} + i\, k_{2e}$. Looking at the extinction coefficient k, let us denote α as the absorption loss of the waveguide in dB/μm in each state, $\alpha = 4.34(4\pi k/\lambda)$. The insertion loss of an amorphous active waveguide of length L is proportional to the product αL, that is IL (dB) = $4.34(4\pi k_{1e} L/\lambda)$ and the crystalline-phase loss is $4.34(4\pi k_{2e} L/\lambda)$. The extinction ratio of a loss modulator discussed below is then ER (dB) = $(k_{2e}-k_{1e})(4.34)(4\pi L/\lambda)$. The Figure 5.1 waveguide combines strong n_{2e}-n_{1e} electro-refraction with strong k_{2e}-k_{1e} electro-absorption because there are significant swings in both real and imaginary GST indices induced by change of phase. By choosing the wavelength of operation appropriately, either the electro-refraction or electro-absorption component can be emphasized. Loss modulation utilizes electro-absorption, while electro-refraction is

mostly neglected: 2 x 2 switching relies upon electro-refraction, with additional requirements that: (1) electro-refraction is much stronger than electro-absorption, and (2) absorption loss in the initial cross state is low. For spatial routing switches, electro-absorption and initial loss are "side effects" that must be worked with to keep high performance.

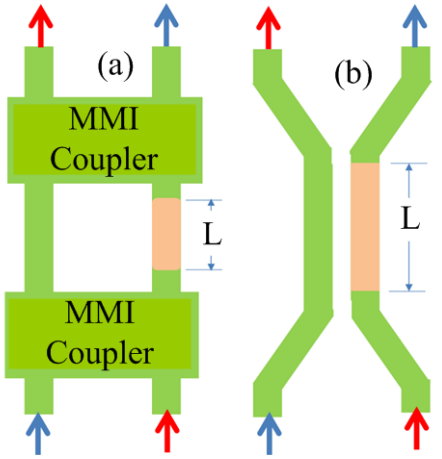

Figure 5.5 Top view of proposed non-resonant 2 x 2 SOI electro-optical channel waveguide spatial routing switches: (a) Mach-Zehnder interferometer, (b) two-waveguide directional coupler. The orange-shaded region indicates an embedded electrically addressed GST ribbon segment.

In switches, it is the product of the phase factor $\Delta\beta$ with L, that affects the transfer of light from the input guide to the output guide, where $\Delta\beta = (2\pi/\lambda)(n_{2e}-n_{1e})$. Different values of $\Delta\beta L$ are required, depending upon the switch geometry [118] and upon whether the device is resonant or non-resonant. Specifically, in Figure 5.5, the Mach-Zehnder interferometer (MZI) requires $\Delta\beta L = \pi$ radians, while the two-waveguide directional coupler needs $\Delta\beta L = 5.4$ rad. It should be addressed that these numbers are empirically

chosen under weakly coupling condition, and the directional coupler is changing from the total power transfer state (cross) to zero coupling state (bar) with the GST transition from amorphous to crystalline state. To minimize IL and crosstalk (CT) in both switching states, we generally desire $n_{2e} - n_{1e} >> k_{2e} - k_{1e}$ with the ratio $\rho = (n_{2e} - n_{1e})/(k_{2e} - k_{1e})$ being as high as possible. Because the IL of the initial switch state is proportional to the $k_{1e}L$ product, a "moderate" value of k_{1e} can present a loss problem when $L > 50\ \lambda$. Since k_{1e} is λ-dependent, then λ must be chosen to give minimization of k_{1e} together with maximization of $n_{2e}-n_{1e}$. This happens at longer wavelengths.

5.6 Simulations for GST embedded SOI Channel waveguide

In all simulations, we have taken the GST thickness as 10 nm for good electrical and optical performance. ITO thickness is given in Figure 5.2. We calculated the complex effective index of the fundamental TE or TM mode at the wavelengths 1310, 1550 and 2100 nm using a FEM based complex mode solver. We used $W = 0.4\lambda$ and $H = 0.2\lambda$ throughout the rest of the simulations reported here for the reason of strong confinement of light.

Results for the first group of simulations performed for Figure 5.2(a) are tabulated in Table 2, where we list the changes in effective index, the ratio ρ, and the effective-index loss in dB/μm for both the first and the second states. The term SGS is used to denote Si/GST/Si.

Table 2 Simulation results for the Figure 5.2(a) waveguide

	Claddings	Wavelength (nm)	WxH (nm)	Mode	Δn_e	Δk_e	ρ	α_{1e} (dB/ μm)	α_{2e} (dB/μm)	α_{2e}-α_{1e} (dB/μm)
SGS	3 air 1 oxide	1310	524x262	TE	0.248	0.355	0.700	1.166	15.92	14.757
				TM	0.039	0.006	6.704	0.314	0.555	0.240
		1550	620x310	TE	0.255	0.190	1.341	0.302	6.990	6.687
				TM	0.031	0.005	5.906	0.090	0.274	0.183
		2100	840x420	TE	0.172	0.033	5.179	0.015	0.879	0.864
				TM	0.027	0.002	15.31	0.012	0.058	0.045

The detailed mode profile over the X-Y cross-section was determined and representative results at the 2100 nm wavelength are given in Figure 5.6. The mode patterns for 1310 nm and 1550 nm (not shown) are quite similar to the 2100-nm pattern.

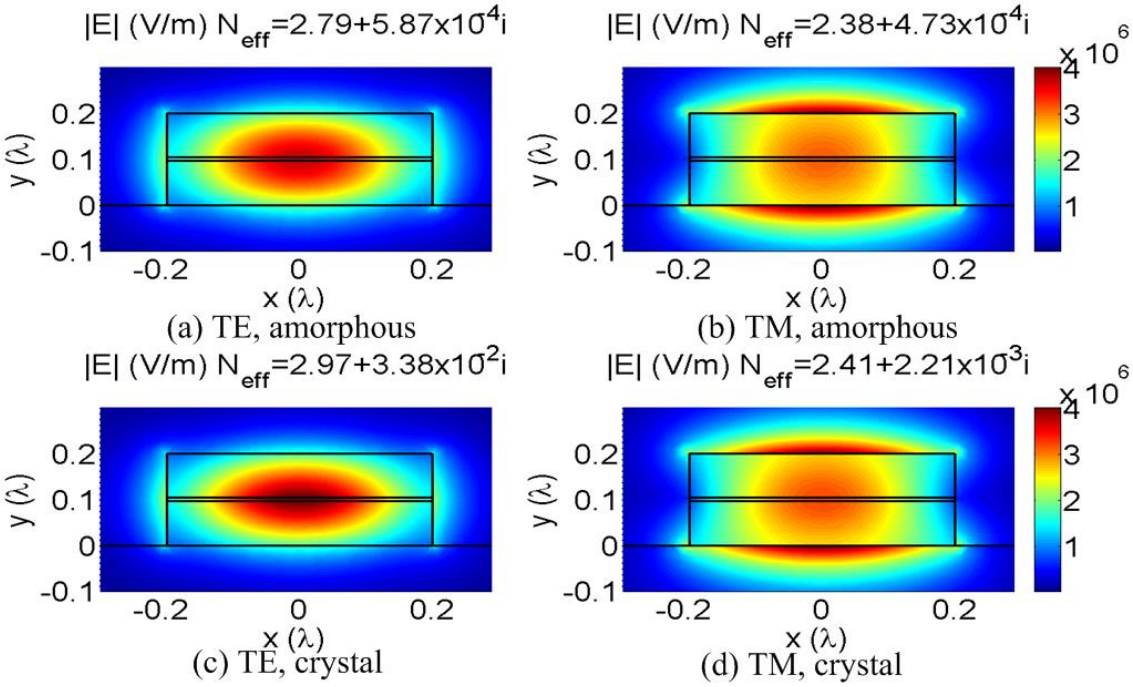

Figure 5.6 Mode distribution for SGS waveguide at λ=2100 nm

The next group of simulations was for the slotted-GST waveguides of Figure 5.2(b), where SIGIS denotes Si/ITO/GST/ITO/Si. Here we present the complete results in Table 3. Representing graphically the Table 3 results at 2100 nm, the TE and TM mode profiles shown in Figure 5.7 indicate that the TM mode is now bunching in the slot, concentrating more at mid-region than in Figure 5.6, while the induced index changes in Table 3 are not much different than those found in Table 2.

Table 3 Simulation results for the Figure 5.2 (b) waveguide

	Claddings	Wavelength (nm)	WxH (nm)	Mode	Δn_e	Δk_e	ρ	α_{1e} (dB/ μm)	α_{2e} (dB/μm)	α_{2e}-α_{1e} (dB/μm)
SIGIS	3 air 1 oxide	1310	524x262	TE	0.212	0.317	0.667	1.024	14.24	13.212
				TM	0.015	0.005	3.336	0.176	0.365	0.189
		1550	620x310	TE	0.225	0.171	1.315	0.273	6.287	6.015
				TM	0.014	0.005	3.020	0.074	0.233	0.159
		2100	840x420	TE	0.155	0.030	5.147	0.020	0.803	0.783
				TM	0.015	0.001	11.72	0.037	0.070	0.033

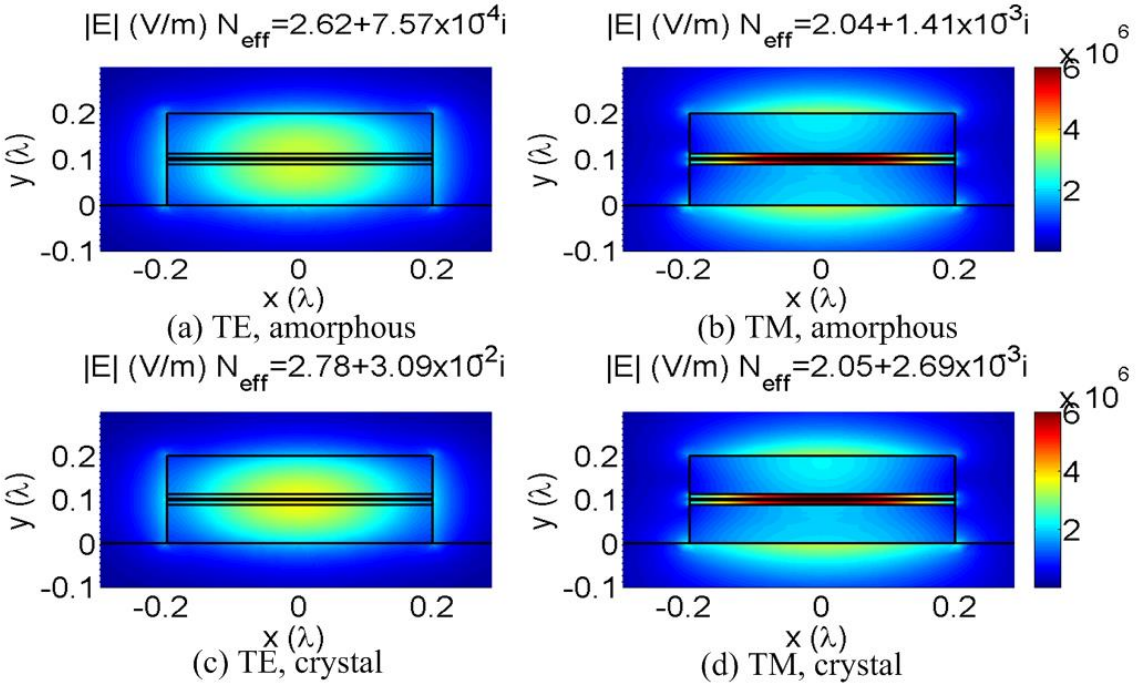

Figure 5.7 Mode distribution for the Figure 5.2 (b) SIGIS waveguide at λ=2100 nm

The final group of results pertains to Figure 5.2(c) and Figure 5.2 (d) where we examine an all-around symmetric cladding and a double-GST electro-optical layer that sandwiches an ITO photonic slot, while the GST/ITO/GST is sandwiched in Si. This Si/GST/ITO/GST/Si layering is termed SGIGS. A final simulation looked at substituting Ge for Si in Figure 5.2(a). Results for these cases are summarized in Table 4. The mode profiles for the double-GST-with-slot and for the Ge waveguide case are presented in Figure 5.8 and Figure 5.9. The TE and TM profiles for the all-around oxide cladding are not shown because they exhibit little change in mode distribution compared to that of air-clad.

Table 4 Simulation results for the Figure 5.2 (c) and Figure 5.2 (d) waveguides as well as germanium in Figure 5.2 (a)

	Claddings	Wavelength (nm)	WxH (nm)	Mode	Δn_e	Δk_e	ρ	α_{1e} (dB/μm)	α_{2e} (dB/μm)	α_{2e}-α_{1e} (dB/ μm)
SGS	4 oxide	2100	840x 420	TE	0.167	0.032	5.160	0.015	0.856	0.841
				TM	0.025	0.002	16.038	0.012	0.053	0.041
SGIGS	3 air 1 oxide			TE	0.317	0.062	5.136	0.026	1.631	1.605
				TM	0.029	0.007	4.202	0.039	0.219	0.180
GeGGe	3 air 1 oxide			TE	0.147	0.028	5.178	0.014	0.751	0.736
				TM	0.052	0.002	15.878	0.015	0.100	0.085

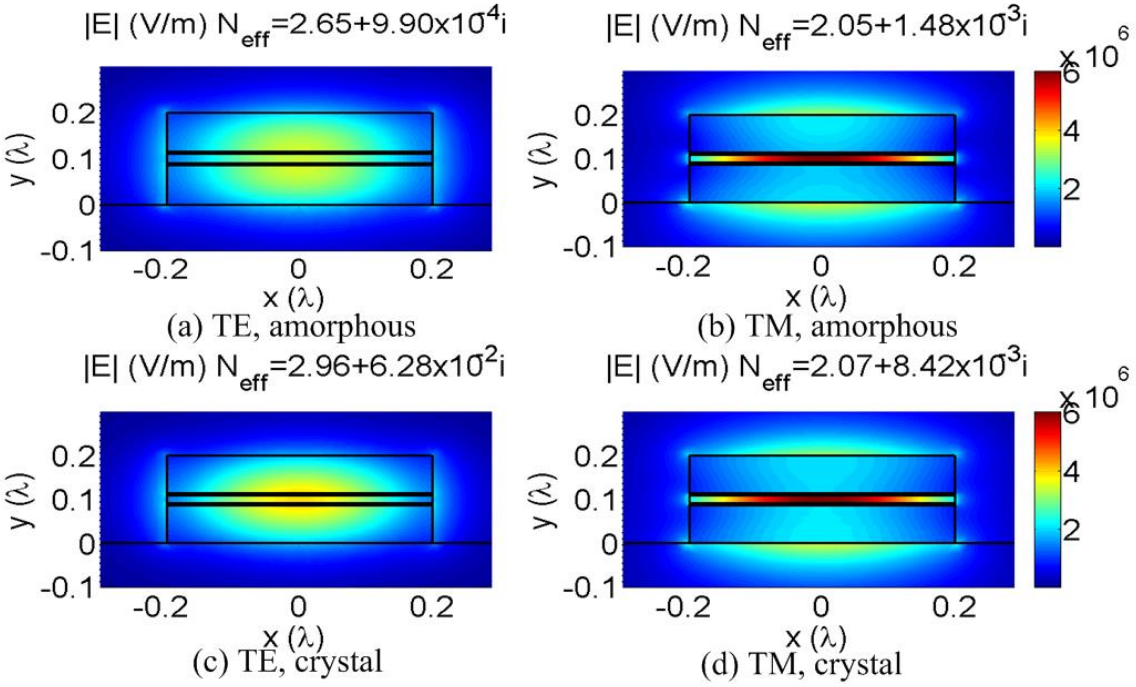

Figure 5.8 Mode distribution for the SGIGS waveguides at λ=2100 nm.

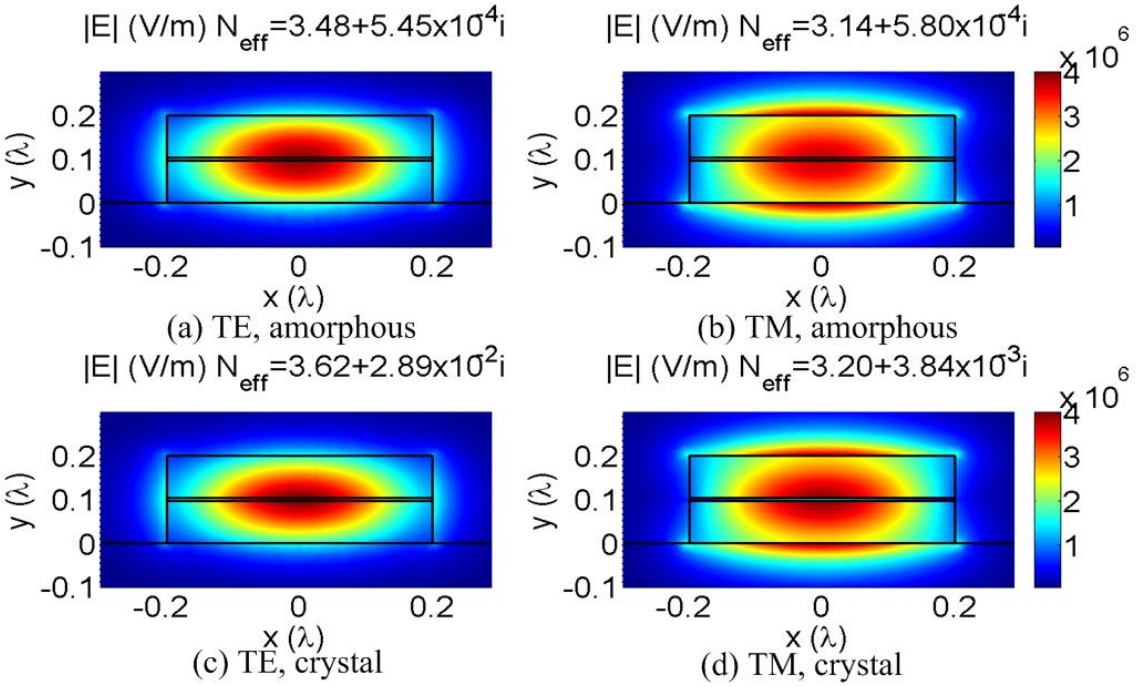

Figure 5.9 Mode distribution for the Ge/GST/Ge waveguides at λ=2100 nm.

5.7 Predicted 2 X 2 switching performance

As per Table 3 and Table 4, the introduction of multiple layers does not elevate significantly the Δn and Δk performance found in Table 2, and so we shall use the TM SGS results (TM has larger ρ than TE cases) in Table 2 to estimate switching performance at 1550 and 2100 nm for the devices of Figure 5.3(a) and Figure 5.3(b), with the ΔβL of 3.14 and 5.4 rad, respectively, in the bar state. These Δβ conditions allow us to find L in the bar state, a length that also becomes the cross-coupling length L. After that we can estimate the initial cross state IL as α_{1e}L. For the MZI, we turn to Fig. 2 of [118] to determine IL and CT in the bar state. Then for the two-waveguide coupler, we utilize

Fig. 8 of [118] in order to estimate IL and CT in the bar state. The complete results are summarized in Table 5 where 2WGDC is the two-waveguide directional coupler.

Table 5 Estimated and simulated performances of 2 X 2 switches using the TM-polarized active SGS segment

λ(nm)	MZI L (μm)	MZI Cross IL (am) dB	MZI Bar IL (cr) dB	MIZ Bar CT (cr) dB	2WG DC L (μm)	2WG DC Cross IL (am) dB	2WG DC Bar IL (cr) dB	2WG DC Bar CT (cr) dB
1550	25	2.3	3.4	-9.9	43	3.9	1.0	-17
2100	38	0.5	1.1	-16	67	0.8	0.4	-22

Looking at these Table 5 estimates, the TM performance generally is very good at 2100 nm as discussed below, but is problematic for GST at 1550 nm because of the rather high IL in the MZI cross and bar states and in the 2WGDC cross state.

Returning to Table 5, we can compare the expected performance of GST-enabled switches to state-of-the art 2 x 2 electro-optical devices in the SOI silicon photonics art. Starting with the 2WGDC, we searched the literature but were not able to locate any experimental coupler examples, recent or early, in the electro-optic SOI art. However, the theory of [95] indicates that an SOI PIN-injected 2WGDC at λ=2100 nm would have an active length of 614μm as compared to the L=67 μm in Table 5. There are many experimental 2 x 2 MZI reference switch examples in the recent 1550-nm SOI electro-optic literature.

Regarding speed, there are “set” and “reset” times needed for “electrical” phase transition. The largest time is around 100 ns according to [108] which would limit the modulation speed in a digital return-to-zero (RZ) format to around 0.5 Mbps if we assume

that the bit duration is 10 times longer than a 100-ns transition time. This modulation rate is slightly faster than that available in thermo-optic effect modulators, but is surely much slower than that in free-carrier-effect modulators. Regarding energy, we have not attempted here to quantify the energy consumption of the modulator. However, we see that energy is consumed only during the state transitions, and no energy is consumed to maintain a state. Message switching is often used in N x N routing switches, and there the <100 ns re-configuration would usually be adequate.

5.8 Predicted 1 X 1 modulator and VOA performance

The principal devices are illustrated in Figure 5.10. It's evident from an inspection of Table 2, Table 3 and Table 4 that the TE mode offers very strong and practical electro-absorption over the entire 1.31-2.1 μm range. TM has some electro-absorption utility but at a lower on/off attenuation ratio. The designer of the 1 x 1 loss-modulated device has a variety of parameters from which to choose. Along with the wavelength, the mode polarization, the cladding geometry and the materials layering can be chosen. Those selections lead to a particular α_{1e} determined in the relevant Table above. Then the active length L can be chosen to provide a desired "low" value of loss $\alpha_{1e}L$ in state 1. For state 2, the same row in the particular Table gives an increase α_{2e}-α_{1e} of waveguide propagation loss, generally a "large" increase as desired. Different waveguide geometries in the Tables offer flexibility in the magnitude of α_{2e}-α_{1e}. The length L can be on the wavelength-scale if wanted. For the variable optical attenuator, there is a set of electrically independent, separately addressed GST segments as shown. The electrical

drive circuit can turn on some or all of the loss-inducing segments, producing an attenuation that is variable in steps. Speed and power were discussed above。

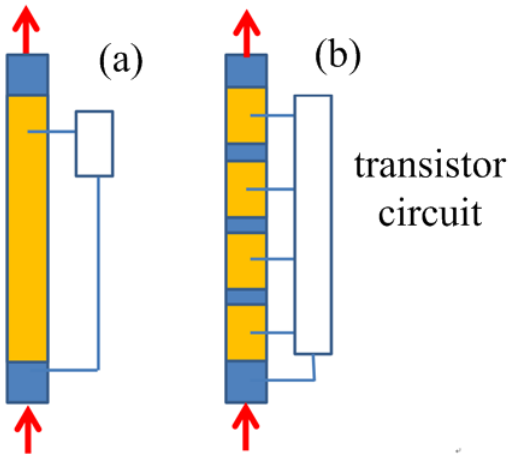

Figure 5.10 Top view, schematic, of 1 x 1 electro-optical waveguide (a) loss modulator, (b) VOA with discretized control.

To give a specific example, the TE mode at 1.55 μm in Table 2 offers 0.6 dB of initial loss (the amorphous phase) in an active length of only 2μm, and when waveguide length is switched to the crystal phase an attenuation of 14 dB is induced. This expected performance may be compared to a state-of-the-art VOA in SOI silicon photonic devices where 1.55-μm experiments [131] were conducted on a PIN carrier-injected silicon ridge waveguide having W x H of 600 nm x 200 nm. There it was found that a 1000-μm active length of waveguide produced a nominal zero of attenuation at zero injection, increasing to 30 dB of attenuation at full injection. Comparing the VOA control power in these two cases, the power is expected to be less in our L = 2 μm self-latching VOA

Regarding the segmented VOA in Figure 5.10(b), there is a question about possible optical losses incurred by unwanted optical reflections at the interfaces between

the active and passive waveguide zones. The loss generally is smaller in the amorphous phase where the Si/GST index mismatch is relatively small. The 1 x 1 of Figure 5.10(a) illustrates the basic reflection losses that are then multiplied in Figure 5.10(b). Figure 5.10(a) is in essence the same as Figure 5.1, and there we see the "nominally smooth" end-fire coupling from Si to SGS to Si which actually has interface losses that can be quantified. We performed an complex MMM calculation of the unwanted reflection loss in Figure 5.1 between a uniform Si channel and the doped SGS channel with its abruptly appearing GST layer in that active segment. Also, a similar complex MMM simulation gave us the reflection IL when light entered the output Si channel from the SGS channel. This work was carried out for the amorphous phase. Then calculations were made for the crystalline phase. We turned to Table 4 for the SGS parameters at λ=2100 nm with W x H = 840 nm x 420 nm and SiO2 cladding all around. The results of our simulations are as follows IL(TE, am) = 0.075 dB, IL(TM, am) = 0.12 dB, IL (TE, cr) = 1.19 dB and IL(TM, cr) = 0.17 dB. Each loss just cited is the sum of input and output loss to one GST segment.

5.9 Summary

TEo and TMo simulations indicate that an ultrathin layer (or layers) of GST embedded in a Si or Ge channel waveguide is viable for SOI-based electro-optical device applications in the near and mid infrared, particularly in spatial routing switches, variable optical attenuators, and modulators. Proposals are made for embedding an active electro-optical GST segment within a passive channel waveguide that forms part of a 2 x 2 or 1 x 1

device. Simulation results on electro-refraction and electro-absorption were employed to estimate IL and CT in 2 x 2 MZIs and 2WGDCs. At λ=2100 nm, excellent performance is projected for both types of broadband, non-resonant switches. However, at λ=1550 nm, the IL was "too large"- in the range of 2.3 to 3.9 dB. For both TE and TM, loss modulation over 1.3 to 2.1 μm looks feasible with good IL and ER, although the modulator is "binary" with speeds limited to ~ 1 Mb/s. The VOA is an ideal application for the 1 x 1 waveguide. By employing independent active regions, a staircase profile of attenuation would be attained as a function of control voltage.

Chapter 6.

Electro-optical Phase-change 2 x 2 Switching using Three- and Four-Waveguide Directional Couplers

6.1 Introduction

This chapter presents modeling and numerical simulations on optical directional couplers comprised of three or four parallel channel waveguides that have a sub-wavelength spacing between each pair of waveguides, a gap filled with low index dielectric. These 2 x 2 devices are utilizing the SOI channel-waveguide with a phase changing material self-holding layer introduced in Chapter 5, and simulated with the full vector improved MMM in Chapter 3. They are labeled here as 3W (three parallel waveguides) and 4W (four parallel waveguides) respectively, and both are based upon evanescent-wave side

coupling. The outer two waveguides are passive and homogeneous in their construction, while the central waveguide or waveguides are active.

Similar to the switching devices in Chapter 5, the major new feature in this study is also the deployment of a thin layer of phase-change material (phase change material) embedded at midlevel in each active channel so that the effective index of the fundamental mode is controlled by an applied electrical signal. This phase change material offers two self-sustained states for the waveguide effective index. Electric power is needed only to transition the material from its amorphous phase (device state 1) to its crystalline phase (device state 2), or to attain the reverse transition from crystal to amorphous. Therefore, each phase change material waveguide is "self-holding" or latching in each of its phases without power applied. Besides, as very large change in waveguide index that is offered by the phase change material, one of the largest electro-optical effects on record as demonstrated in Chapter 5, it is possible to couple waveguides closely and to switch light over small device lengths, a strategy that mitigates insertion loss of the device. The hitherto unexplored "strong coupling limit" is a new contribution in this work.

6.2 Comparison with the prior art

The prior art consists of 1 x 1 modulators and 2 x 2 switches. A general theme in that art is that the phase change material is deposited as an optical cladding upon an exposed top surface of a waveguide core. As a result, only a small overlap is attained there between the fundamental mode profile and the off-core optical index-change region. Our

approach, by contrast, provides a strong advantage because the optical-change region is sited exactly at the peak of the mode profile. So we get a larger overlap integral. Our approach also is a broadband non-resonant technique. The wavelength of operation can be changed by several nanometers without injuring the electro-optical switching. This improves upon some resonant prior art[133] where a racetrack resonator had phase change material cladding perturbation. Most of the prior art uses optical control, which means that a "shortwave" optical pump was shined upon the phase change material cladding to trigger switching. We feel that such optical control is not practical, and that our electrical actuation is much preferred.

There is one recent example of a 1 x 1 waveguide device in which lateral P and N electrodes allowed electrical control of a VO_2 optical cladding [134]. Although the control reported there is desirable, the cladding location is not.

Chapter 5 [25] has dealt with a single layer of phase change material embedded at the central plane of a silicon channel waveguide; however the active devices examined previously were different from the devices investigated here. The prior work in chapter 5 simulated variable optical attenuators and 2 x 2 electro-optical switches comprised of either a Mach-Zender interferometer or a directional coupler made from two waveguides. What is new here is the directional coupler made from three or four parallel waveguides. The present 3,4 waveguide switches have an advantage over the previous 2-waveguide (2W) structure because the active and potentially lossy phase-change regions are not located in waveguides connected to the on-chip network (they are isolated "islands" here),

whereas in the prior 2W the active region is situated directly on-axis in a network waveguide, leading to added loss and switch asymmetry.

6.3 Theory and design method

Figure 6.1 shows the schematic top-view of our proposed optical switches based on phase change material . The 3W switch refers to the structure with one phase change material embedded waveguide in the center, while 4W switch refers to the structure with two phase change material -embedded central waveguides. The two insets in Figure 6.1 indicate that the in/output silicon channel waveguides are surrounded by silicon dioxide; while the SiO_2-clad centered waveguides are n-doped silicon channel halves with a 10-nm thick phase change material layer embedded between them. The total length for phase change material layer in Figure 6.1 is labeled "L_{am}". "L_{cr}" is the length of active region where the external voltage will be applied to change the phase of phase change material . The vertical gap (edge to edge) in coupling region between adjacent waveguides is labeled as "G". Each active waveguide is truncated at a length L_{am} and takes the amorphous state 1, as default, and when voltage is applied, the active region with a length L_{cr} will be transferred to crystalline state 2. The two outer waveguides (the means for 2 x 2 routing) join smoothly the integrated photonic waveguide network that resides on-chip.

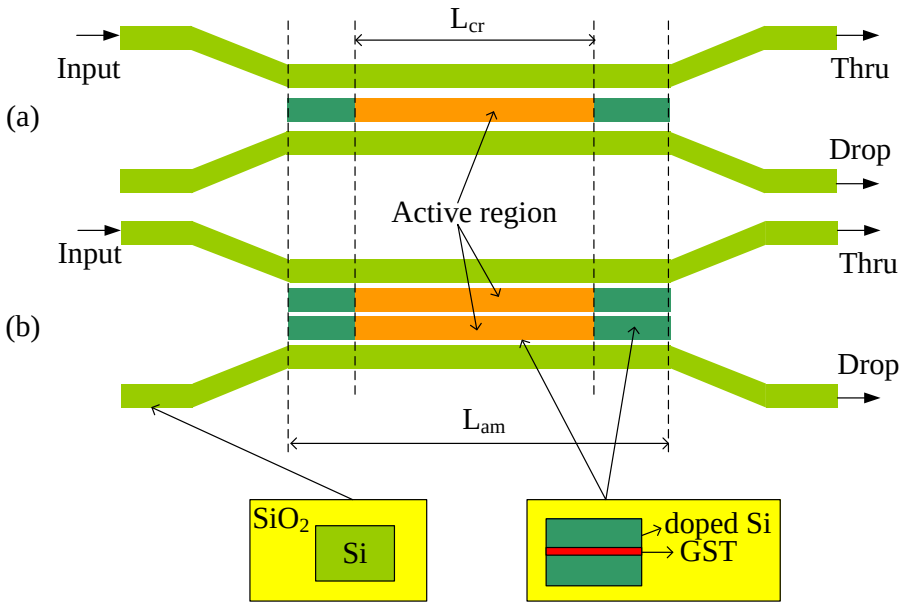

Figure 6.1 electro-optical 2 x 2 switch in the amorphous_and crystalline states using Si and doped-Si/GST/doped-Si waveguides (a) for 3W (b) for 4W.

When the active waveguides are in state 1, at small L_{am}, light entering the outer waveguides travels through them, but as L_{am} is increased the light becomes "completely" exchanged between the two waveguides. These "through" and "exchange" conditions are called the "bar" and "cross" states, respectively. As L_{am} increases, the device reaches, in sequence, the first bar, the first cross, the second bar, the second cross, etc. Then, turning the active region into state 2, the side coupling weakens as the refractive index difference between the outside and centered waveguides increases. With careful design for the active region's length L_{cr}, we can change bar to cross or vice versa. An unexpected finding in this research is that the second bar for state 1 gives better performance than the first cross for state 1. An invention in the present work is arranging different active lengths for state 2 ($L_{cr} \leqq L_{am}$) to provide adjustment of the optical retardation $\Delta\beta L$ offered by the phase

change material in state 2. Here we focus on the aforementioned phase change material GST[108][135], which is reported to have electro-optical properties superior to those of aforementioned vanadium dioxide [24][134]. Other than GST, several alternative phase change material s can also be applied in the implementations in this work [129][136][138].

Prior work in chapter 5 on the active waveguide in Figure 6.1 [25] was performed at the 2100 nm wavelength which is adopted throughout this work. As mentioned in Chapter 5, this operation was chosen for on-chip applications in the newly emerging ~2μm fiber-optic communications band. Rather than 2000 nm, the wavelength 2100 nm is selected because the optical extinction coefficient here, k_{am} = 0.006, is smaller than the 0.009 extinction at 2000 nm. To begin analyzing Figure 6.1, we need the refractive indices of the materials in Figure 6.1. For the SiO_2 all-around cladding, n = 1.44. The outer two waveguides have n= 3.45, while the N-type Si in the middle waveguide has index 3.45 + i 0.0003 at its doping density of 1 x 10^{18} cm^{-3}. The complex index of the GST film in each phase as follows: n_{am} + i k_{am} = 4.05 + i 0.006; n_{cr} + i k_{cr} = 6.80 + i 0.40, which is consistent with the simulation in Chapter 5.

The switching analysis here is based upon knowledge of the fundamental mode effective index variation from the earlier study at 2100 nm investigating a Si/GST/Si channel with W x H cross section of 840 nm x 420 nm including 10 nm of GST and 840 nm x 205 nm doped-Si strips as in Chapter 5 or [25]. To simulate such a structure, we conduct the 3D simulation with IMMM as described in Chapter 5 for the coupling section in Figure 6.1 which is more computationally friendly compared with other competitors, such as FDTD and BPM, as the propagation length of interest varies within a large range

that goes up to 1000 microns. The complex modes applied are from a finite-element method-based solver under the frame of perfect matching layers (PML) and perfectly reflecting boundaries (PRB) as mentioned in Chapter 1.

6.4 Simulation results

We tested two configurations: (1) the second bar for the amorphous state (state 1) and the first cross for crystalline state (state 2), (2) the first cross for the amorphous state and the first bar for the crystalline state. Choosing a narrow gap G and launching polarized light into one input, we calculated for the amorphous state the normalized optical power emerging from the through-port and from the drop-port as a function of coupling length L_{am}. Those power curves exhibited a rippled sinusoid behavior. There are two factors that determine the optical transmission versus length, the closeness of optical phase matching between waveguides and the material absorption loss. The ripples on the transmission curves that are found here are due to the combination of those two effects. The oscillations occur as the waveguides go in and out of matching.

Fixing L_{am} at the value giving peak transmission, we then put the switch into its crystalline state and plotted the through- and drop-powers versus L_{cr}. Having made those two plots, we determined the optical insertion loss (IL) and optical crosstalk (CT) of the 2 x 2. We then repeated this procedure for other trial values of G, thereby converging upon the best results. Figure 6.2 ~ Figure 6.5 present two representative cases of interest, both for the TE mode. Figure 6.2 and Figure 6.3 show the 3W response when the device is at second bar in the amorphous state, while Figure 6.4 and Figure 6.5 show the calculated

behavior when the first cross is used for amorphous state. Similarly, we show the 4W response when the device is at the second bar in the amorphous state in Figure 6.6, and show the 4W response when the first cross is used for amorphous state in Figure 6.7. Figure 6.8 illustrates the spectrally flat switching behavior found for a representative 3W switch (assumed there is that the refractive index for silicon, for silicon dioxide, and for phase change material are not changed over the wavelength range of 2090nm to 2110nm.) This demonstrates the desired broadband switching nature.

One interesting phenomenon observed in Figure 6.3(b) and Figure 6.6(b) is the strong transmission from the input port to the drop port with almost no field in the central waveguides in their crystalline state. This happens because the optical phase is truly matched among the 3 or 4 waveguides. In those cases, almost all the input light is coupled from the input waveguide to the output waveguide, and so there is a negligible portion in the intervening waveguides.

Going into more detail, we have quantified the switching performance for four 3W devices as well as for four 4W switches, with these simulation results presented in Table 6 and Table 7 where we show the mode, the gap, the active lengths, the IL and the CT in both amorphous (am) and crystalline (cr) states. The 3W results are advantageous because of low IL-and-CT as well as device lengths that are short by comparison to the active lengths projected for free-carrier injection switches [139]. Although the 4W offers superior crosstalk performance, the 4W response is generally less favorable than that of 3W because of the fairly high losses and long lengths found in 4W.

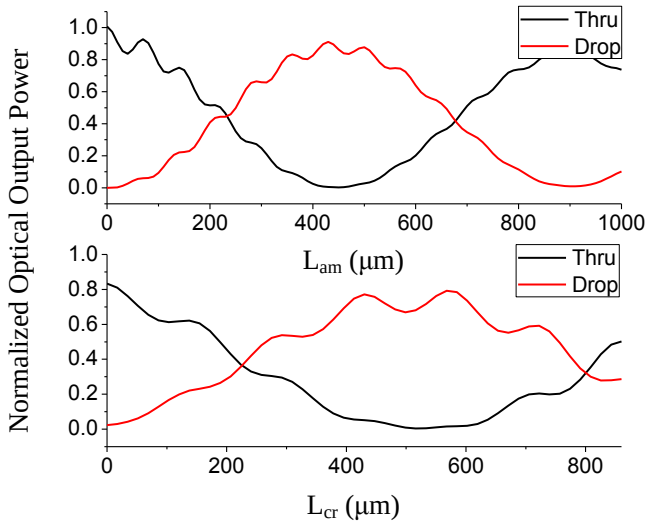

Figure 6.2 Two output powers of 3W device with TE mode and G=200 nm. Shown are power versus L_{am} in state 1 (upper) and power versus L_{cr} in state 2 (lower), when L_{am} is fixed at 860 μm.

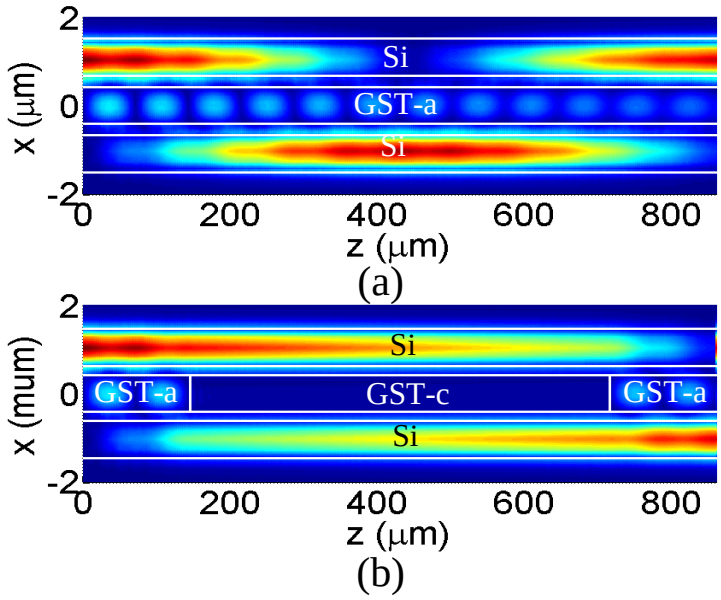

Figure 6.3 Field distribution of 3W device (top view) with TE mode and G=200 nm, taking L_{am} = 860μm and L_{cr} = 568μm: (a) amorphous, (b) crystalline.

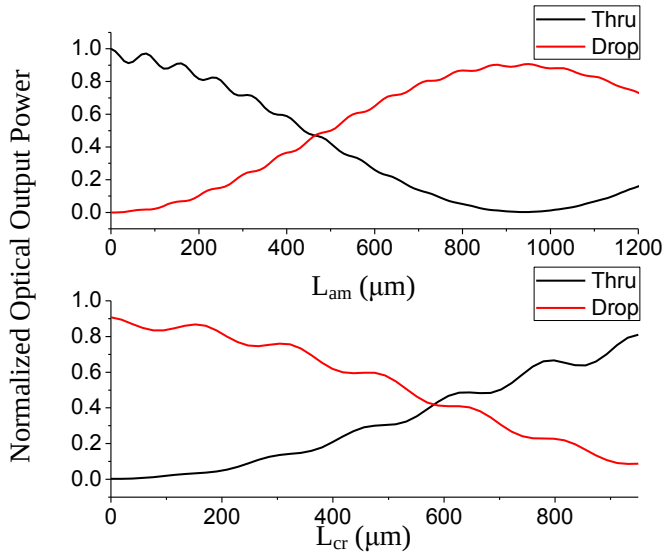

Figure 6.4 Two output powers of 3W device with TE mode and G=250 nm. Shown are power verus L_{am} in state 1 (upper) and power versus L_{cr} in state 2 (lower), when L_{am} is fixed at 950 μm.

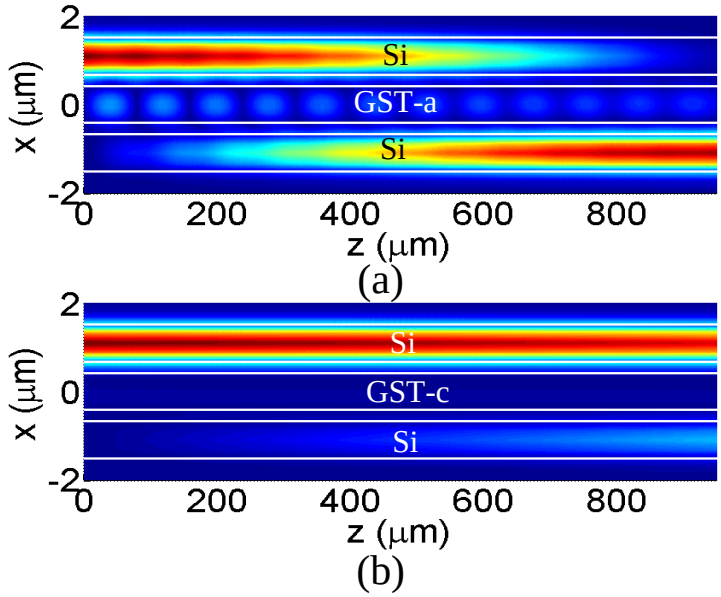

Figure 6.5 Field distribution of 3W device (top view) with TE mode and G=250 nm, taking L_{am} = 950μm and L_{cr} = 950μm: (a) amorphous, (b) crystalline.

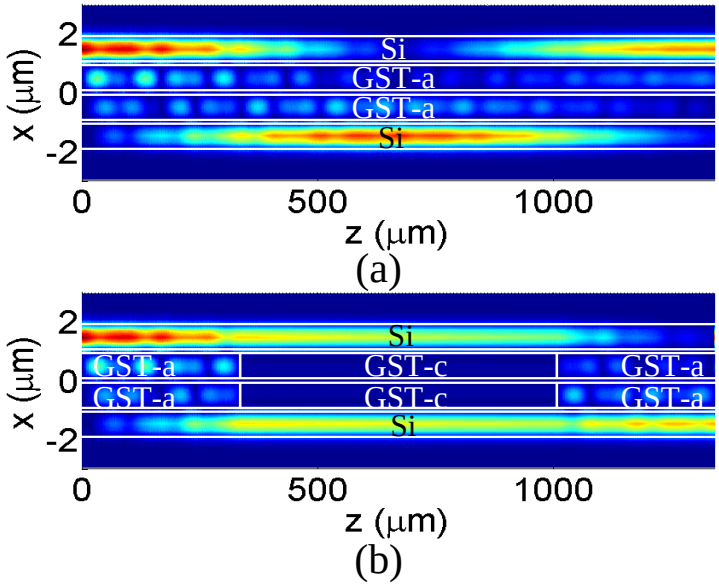

Figure 6.6 Field distribution of 4W device (top view) with TE mode and G=150 nm taking L_{am} = 1340μm and $L_{c.r}$= 670μm: (a) amorphous, (b) crystalline.

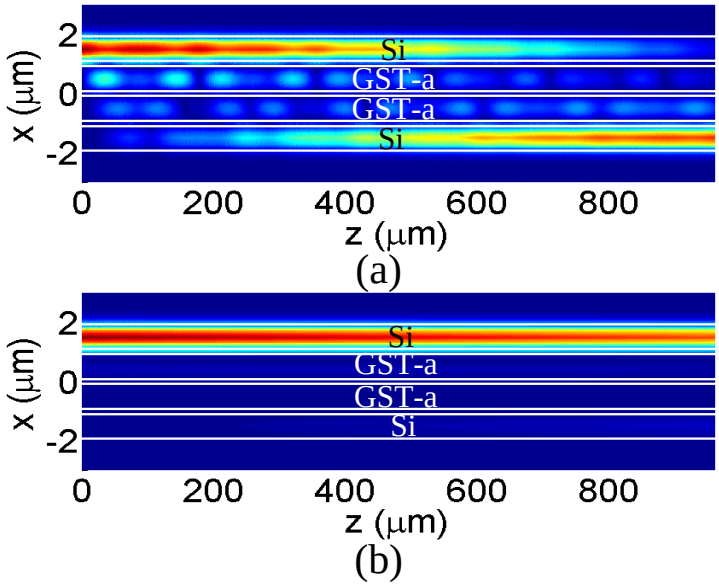

Figure 6.7 Field distribution of 4W device (top view) with TE mode and G=170 nm taking L_{am} = 960μm and L_{cr} = 960μm: (a) amorphous, (b) crystalline.

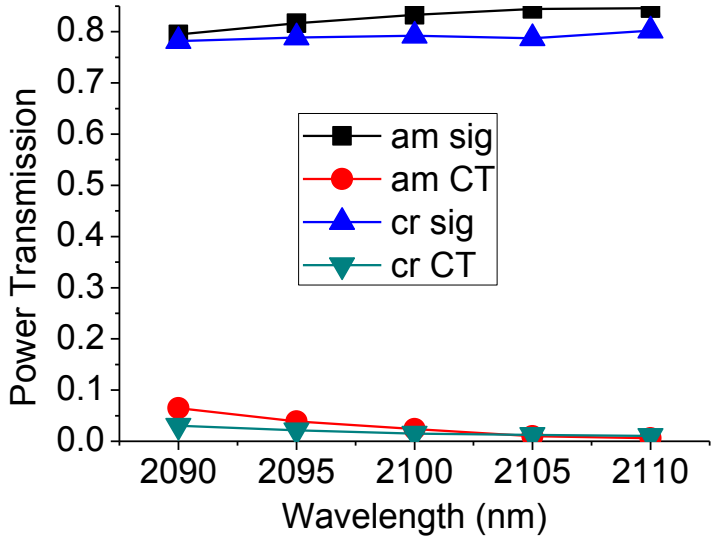

Figure 6.8 Optical signal and crosstalk versus wavelength for 3W 2 x 2 switch with TE mode and G=200nm taking L_{am} = 860µm and L_{cr} = 568µm. Results for the am and cr states are shown.

Table 6 Infrared transmission (signal and noise) of several 3W 2 x 2 devices in both states.

Mode	Gap	Am	Cr	L_{am}	IL_{am} (dB)	CT_{am} (dB)	L_{cr}	IL_{cr} (dB)	CT_{cr} (dB)
TE	200nm	2 bar	1 cross	860µm	0.8	-16.2	568µm	1.0	-18.2
TM	400nm	2 bar	1 cross	550µm	0.7	-23.0	550µm	0.6	-30.0
TE	250nm	1 cross	1 bar	950µm	0.4	-27.0	950µm	09	-10.6
TM	500nm	1 cross	1 bar	640µm	1.3	-9.1	640µm	1.5	-6.5

Table 7 Infrared transmission (signal and noise) of several 4W 2 x 2 devices in both states.

Mode	Gap	Am	Cr	L_{am}	IL_{am}	CT_{am}	L_{cr}	IL_{cr}	CT_{cr}

					(dB)	(dB)		(dB)	(dB)
TE	150nm	2 bar	1 cross	1340μm	2.4	-19.2	670μm	3.1	-24.0
TM	350nm	2 bar	1 cross	670μm	1.8	-30.0	456μm	2.2	-30.0
TE	170nm	1 cross	1 bar	960μm	1.6	-20.0	960μm	1.8	-25.2
TM	390nm	1 cross	1 bar	640μm	1.6	-18.9	510μm	1.3	-10.3

6.5 Comparison and conclusion

To place Table 6 and Table 7 in context, let's compare these results with the present art of directional coupler switches for the near infrared and mid infrared. A prime competitor to GST is the 3W and 4W utilizing free-carrier injection that produces electro-refraction and electro-absorption during forward bias. At injection-off, the switch's insertion loss is quite low over 1.3 to 8.0 μm. The GST state-1 competes here for low loss. The free-carrier devices need a holding-on current for state 2, but the GST has the advantage here; no such current is required. The free-carrier injection-on state has been modeled [118]at the so-called reasonable 5 x 10^{17} cm^{-3} level of electron-and-hole injection and there the active lengths at 2.1 μm were L(3W) = 3100 μm and L(4W) = 1500 μm, giving the compactness advantage to GST. The electro-absorption in state 2 of both free-carrier and GST increases the insertion loss by about the same amount.

A second competitor to GST is the dc-poled second-order electro-optical polymer that can be embedded in the central waveguides of 3W and 4W, for example organic polymer that fills a horizontal slot between doped-silicon "halves" of a strip channel

waveguide. This silicon-organic hybrid uses the electro-optical Pockels effect that offers much lower loss than GST in state 2, and slightly lower loss than GST in state 1. However, there is a length issue, and even if we consider the most advanced polymers [140][141] we estimate that the active length at 2.1 μm is approximately 2000 μm. Hence GST is considerably more compact. The polymer needs a holding-on voltage.

The thermo-optical (TO) effect, which is quite slow, can be employed in 3W and 4W switches using resistance heaters on the central waveguides, but then the switching device would be a few millimeters long because the TO- induced index change would be small [118] by comparison to the index-shift from phase change. Again, the GST switch has the compactness advantage.

Looking at the lower-right inset in Figure 6.1, electro-optical switching will certainly be feasible when phase change materials other than GST are substituted in the waveguide for GST. The main issue for an alternative phase change material is its extinction factors k_{am} and k_{cr} because we have found generally that the IL and CT are determined by those phase change material loss factors at the wavelength of interest. Operation of GST at the 1550 nm telecom wavelength is problematic because of its factors. Those factors are lower at telecom for the phase change materials of GeTe, $Ge_2Sb_1Te_4$ and GeSe. Hence those "new phase change material " 2 x 2 devices are expected to be more successful at telecom.

Chapter 7.

Conclusions and Future Work

7.1 Conclusions

This thesis covers a series of theory improvements and applications of the complex mode theory and complex modal analysis for the silicon photonics devices. The complex mode theory is derived for the simulation model truncated by PML and PRB, generating complex modes which can expands both guided wave and radiation wave in a unified form. Both the guided wave oriented waveguide designs and the radiation field dominant scattering problems are addressed here.

The major contributions of this thesis are summarized as follows:

In Chapter 2, we present a simple and efficient approach for higher order complex Berenger modes computation. We establish the physical mapping between radiation modes and complex Berenger modes, and theoretically prove that the higher order substrate Berenger modes and the cladding Berenger modes can converge to a cluster of

complex modes with the same phase angle. This model can be explained by weighted optical path distance in both cladding and substrate, and can be implemented by adjusting parameters of PMLs. An example of germanium photo-detector has been utilized to evaluate the merits of this method in terms of robustness, efficiency, and accuracy.

In Chapter 3, two fundamental principles of the MMM−mode orthogonality and tangential field continuity conditions−have been revisited in depth. With a finite number of modes employed in the conventional method, the tangential field continuity condition at the waveguide-discontinuity interface fails, leading to a field mismatch error. We propose an alternate, superior mode matching method−implemented by reconstruction of the auxiliary coefficient matrix, rather than by applying the above-mentioned continuity and orthogonality. Detailed transfer-matrix equations have been derived for the finite-mode-number case. We showed that the IMMM yields a smaller field mismatch error under equal computational effort. Examples of bending and faceted waveguide structure have been investigated and the numerical simulation results demonstrated that the newly proposed method has the merits of simple implementation, high accuracy and high computational efficiency for application in high-index-contrast photonic integrated circuits. Besides, insights of radiation coupling and energy transfer by way of high order bending modes have been discussed.

In Chapter 4, we have investigated a hybrid plasmonic-photonic mode in Si and Ge channel waveguides over the 1.55-8.0 μm wavelength range. A 10-nm Cu ribbon was buried midway within a Si_3N_4 “photonic slot” centered in the semiconductor strip. For the TM_o mode, propagation lengths L of several millimeters are predicted for a waveguide

cross-section of about 0.7λ/n x 0.7λ/n which offers optical confinement mainly within the ~λ^2/400-area slot. The L increased strongly with λ. For 0.4λ/n x 0.4λ/n channels, we found multi-centimeter propagation, but there ~60% of the propagating energy had leaked out into the thick, all-around Si_3N_4 cladding.

Chapter 5 reports theoretical designs and simulations of electro-optical 2 x 2 switches and 1 x 1 loss modulators based upon GST-embedded SOI channel waveguides. It is assumed that the amorphous and crystalline phases of GST can be triggered electrically by Joule-heating current applied to a 10-nm GST film sandwiched between doped-Si waveguide strips. TE_o and TM_o mode effective indices are calculated over 1.3 to 2.1μm wavelength range. For 2 x 2 Mach-Zander and directional-coupler switches, low insertion loss, low crosstalk, and short device lengths are predicted for 2.1μm, although a decreased performance is projected for 1.55μm. For 1.3-2.1 μm, the 1 x 1 electro-optical waveguide has application as a variable optical attenuator and as a digital modulator, albeit with 100ns state-transition time. Because the active material has two "stable" phases, the device holds itself in either state, and voltage need be applied only during transition.

In Chapter 6, theoretical modeling and numerical simulation have been performed at λ = 2100 nm on SOI channel-waveguide directional couplers in which the outer two Si waveguides are passive and the central waveguide(s) are electro-optical "islands." The electro-optical channel(s) utilize a 10-nm layer of GST phase-change-material sited at midlevel of a doped Si channel. A voltage-driven phase change produces a large change in the effective index of the TE_o and TM_o modes, thereby inducing cross-bar 2 x 2

switching. IMMM is employed to estimate electro-optical switching performance in the limit of strong inter-guide coupling. Low-loss switching is predicted both for cross-to-bar and bar-to-cross coupling lengths. These "self-holding" switches had active lengths of 500 to 1000 μm which are shorter than those in couplers relying upon free carrier injection. The four-waveguide devices had lower crosstalk but higher loss than the three-waveguide devices. For the crystalline phase, we sometimes used an active length that was smaller than that for the amorphous phase.

7.2 Future work

In this thesis, we have already talked about the improvements of complex mode theory and the applications of complex modal analysis in the waveguide design, scattering filed simulation, and the leaky structure modeling. Several topics are related and remained for further investigation, which are listed as follows:

The mode solvers, as the first step and basic tools in modal analysis, can be improved, especially in the 2D case. The high order accuracy boundary conditions are needed to be realized for 2D mode solvers. It will be a great improvement for the applications and algorithms using high order complex Berenger modes, which are less accurate in the prior mode solvers.

In Chapter 2, we successfully modify the modes to make the field distributions of high order Berenger modes more symmetric, and the various kinds of Berenger modes degenerate into only one bunch of modes finally, through adjustment in PML design. All the derivation and simulation in that chapter is merely in 1D situation. The extension of

this work into 2D case is also promising. Actually, it is already applied in the 2D waveguide facet simulation later in Chapter 3, but the rigorous derivation and proof are still necessary.

In Chapter 3, we investigated the bending modes and their roles in transmission and radiation effect. The waveguide we are chosen is actually not from silicon platform, and is a weakly guided one. As the silicon photonics is featured by high confinement and strong guiding property, a specific investigation will be necessary and practical.

In Chapter 4, we introduce a kind of "blade waveguide", which is when the channel waveguide embedded with metallic film has an extremely large height-width ratio. For this waveguide, lot of lights are leaking into the lateral area. It is very promising to use such a waveguide for evanescent coupling, like in the directional coupler, or bus-ring resonator.

Chapter 5 and chapter 6 are dealing with silicon channel waveguide embedded with GST layer for electro-optical modulation or switching. I only focus on the non-resonance devices, while this waveguide is definitely suitable for resonant structures. Besides, with the merits like power self-sustenance and huge phase and loss change, the spatial light modulator is also a promising application.

Bibliography

[1] B. Jalali, S. Yegnanarayanan, T. Yoon, T. Yoshimoto, I. Rendina, and F. Coppinger, "Advances in silicon-on-insulator optoelectronics," *IEEE J. Sel. Topics Quantum Electron.* 4(6), 938–947 (1998).

[2] R. Nagarajan, C. H. Joyner, R. P. Schneider, Jr, J. S. Bostak, T. Butrie, A. G. Dentai, V. G. Dominic, P. W. Evans, M. Kato, and M. Kauffman, "Large-scale photonic integrated circuits," *IEEE J. Sel. Topics Quantum Electron.* 11(1), 50–65, (2005).

[3] A. Mekis, S. Gloeckner, G. Masini, A. Narasimha, T. Pinguet, S. Sahni, and P. De Dobbelaere, "A grating-coupler-enabled CMOS photonics platform," *IEEE J. Sel. Top. Quantum Electro.* 17(3), 597-608(2011).

[4] M. Hochberg, and T. Baehr-Jones, "Towards fabless silicon photonics," *Nat. Photonics* 4 (8), 492-494 (2010).

[5] P. Dumon, W. Bogaerts, V. Wiaux, J. Wouters, S. Beckx, J. Van Campenhout, D. Tailaert, B. Luyssaert, P. Bienstman, D. Van Thourhout, and R. Baets, "Low-loss SOI

photonic wires and ring resonators fabricated with deep UV lithography," *IEEE Photonics Technol. Lett.* 16(5), 1328-1330 (2004)

[6] W. Bogaerts, R. Baets, P. Dumon, V. Wiaux, S. Beckx, D. Taillaert, B. Luyssaert, J. Van Campenhout, P. Bienstman, and D. Van Thourhout, "Nanophotonic waveguides in silicon-on-insulator fabricated with CMOS technology," *J. Lightwave Technol.* 23(1), 401–412, (2005).

[7] U. Fischer, T. Zinke, J. R. Kropp, F. Arndt, and K. Petermann, "0.1dB/cm waveguide losses in single-mode SOI rib waveguides," *IEEE Photonics Technol. Lett.* 8 (5), 647 – 648 (1996).

[8] Y. A. Vlasov, and S. J. McNab, "Losses in single-mode silicon-on-insulator strip waveguides and bends," *Opt. Express* 12(8), 1622-1631 (2004).

[9] A. Koster, E. Cassan, S. Laval, L. Vivien, and D. Pascal, "Ultracompact splitter for submicrometer silicon-on-insulator rib waveguides," *J. Opt. Soc. Am. A* 21(11), 2180-2185 (2004).

[10] H. Z. Wei, J. Z. Yu, Z. L. Liu, X. F. Zhang, W. Shi, and C. S. Fang, "Silicon-on-insulator based 2 x 2 multimode interference coupler with large tolerance," *Chin. Phys. Lett.* 18(2), 245 (2001).

[11] I. Kiyat, A. Aydinli, and N. Dagli, " A compact silicon-on-insulator polarization splitter," *IEEE Photonics Technol. Lett.* 17(1), 100-102 (2005).

[12] W. Bogaerts, P. Dumon, D. Van Thourhout, and R. Baets, "Low-loss low-cross-talk crossings for silicon-on-insulator nanophotonic waveguides," *Opt. Lett.* 32(19), 2801-2803 (2007).

[13] W. M. Green, M. J. Rooks, L. Sekaric, and Y. A. Vlasov, "Ultra-compact, low RF power, 10 Gb/s silicon Mach–Zehnder modulator," *Opt. Exp.* 15(25), 17106–17113, (2007).

[14] L. Liao, D. Samara-Rubio, M. Morse, A. Liu, D. Hodge, D. Rubin, U. D. Keil, and T. Franck, "High speed silicon Mach–Zehnder modulator," *Opt. Exp.* 13(18), 3129–3135, (2005).

[15] M. A. Gullen-Torres, E. Cretu, N. A. F. Jaeger, and L. Chrostowski, "Ring resonator optical gyroscopes – parameter optimization and robustness analysis," *J. Lightwave Technol.* 30(12), 1802-1817 (2012).

[16] X. Wang, W. Shi, H. Yun, S. Grist, N. A. F. Jaeger, and L. Chrostowski, "Narrow-band waveguide Bragg gratings on SOI wafers with CMOS-compatible fabrication process," *Opt. Express* 20 (14), 15547 – 15558 (2012).

[17] P. Dumon, W. Bogaerts, D. Van Thourthout, D. Taillaert, R. Baets, J. Wouters, S. Beckx, and P. Jaenen, "Compact wavelength router based on a silicon-on-insulator arrayed waveguide grating pigtailed to a fiber array," *Opt. Express* 14(2), 664-669 (2006).

[18] N. Na, H. Frish, I. W. Hsieh, O. Harel, R. George, A. Barkai, and H. Rong, "Efficient broadband silicon-on-insulator grating coupler with low backreflection, " 36 (11), 2101-2103 (2011).

[19] H. Liang, R. Soref, J. Mu, X. Li, W. P. Huang, "Long range mid-infrared propagation in Si and Ge hybrid plasmonic-photonic nano-ribbon waveguides", *Opt. Express* 22 (23), 28489-28499 (2014).

[20] D. J. Thomson, F. Y. Gardes, J. M. Fedeli, S. Zlatanovic, Y. Hu, B. P. P. Kuo, E. Myslivets, N. Alic, S. Radic, G. Z. Mashanovich, and G. T. Reed, "50-Gb/s silicon optical modulator," *IEEE Photonics Technol. Lett.* 24(4), 234-236 (2012).

[21] N. Rouger, L. Chrostowski, and R. Vafaei, "Temperature Effects On Silicon-On-Insulator (SOI) Racetrack Resonators: a Coupled Analytic and 2D Finite Difference Approach, " *J. Lightwave Technol.* 28(9), 1380-1391(2010).

[22] R. A. Norwood, "Organic electro-optic materials and devices: molecular engineering driving device performance and technology innovation," paper SM2M.1 presented at the Conference on Lasers and Electro-Optics, San Jose, CA, 8 June 2014

[23] C. Ye, Z. Li, R. Soref, and V. J. Sorger, "Strong ITO index modulation for switching devices," paper JM3B.1 presented at the OSA Photonics in Switching Topical Meeting, San Diego, CA, 13 July 2014

[24] H. T. Kim, B. J. Kim, S. Choi, B. G. Chae, Y. W. Lee, T. Driscoll, M. M. Qazilbash, and D. N. Basov, "Electrical oscillations induced by the metal-insulator transition in VO2," *J. Appl. Phys.*107(2), 023702 (2010).

[25] H. Liang, R. Soref, J. Mu, A. Majumdar, X. Li, and W. P. Huang "Simulation of Silicon-on-insulator Channel-waveguide Electro-optical 2 x 2 Switches and 1 x 1 Modulators Using a Ge2Sb2Te5 Self-holding Layer", *J. Lightwave Technol.* 33 (9), 1805-1813 (2015).

[26] L. Nagel and R. Rohrer, "Computer analysis of nonlinear circuits, excluding radiation (CANCER)," *IEEE J. Solid-State Circuits* 6(4), 166–182 (1971).

[27] L. W. Nagel and D. O. Pederson, "Simulation Program with Integrated Circuit Emphasis (SPICE)," Univ. California, Berkeley, CA, Tech. Rep. ERL-M382, Apr. 1973.

[28] A. Taflove and S. C. Hagness, "Computational Electrodynamics : the finite-difference time-domain method," Boston: Artech House, 2005.

[29] K. S. Yee, "Numerical solution of initial boundary value problems involving Maxwell's equations in isotropic media," *IEEE Trans. Antennas Propag.* 16(3), 302-307 (1966).

[30] J. Gerdes and R. Pregla, "Beam-Propagation Algorithm Based on the Method of Lines," *J. Opt. Soc. Am. B* 8(2), 389-394 (1991).

[31] G. R. Hadley, "Wide-Angle Beam Propagation Using Pade Approximant Operators," *Opt. Lett*. 17(20), 1426-1428 (1992).

[32] K. Q. Le, "Complex Pade Approximant Operators for Wide-Angle Beam Propagation," *Opt. Commun.* 282(7), 1252-1254 (2009).

[33] T. E. Rozzi, “Rigorous analysis of step discontinuity in a planar dielectric waveguide,” *IEEE Trans. Microwave Theory Tech*. 26(10), 738-746 (1978)

[34] H. Derudder, D. De Zutter, and F. Olyslager, "Analysis of waveguide discontinuities using perfectly matched layers," *Electron. Lett.* 34(22), 2138-2140 (1998).

[35] A. Yariv, “Coupled-mode theory for guided-wave optics,” *IEEE J Quantum Electron*. 9, (9), 919-933 (1973).

[36] H. A. Haus, W. P. Huang, S. Kawakami, and N. A. Whitaker, “Coupled-mode theory of optical wave-guides,” *J. Lightwave Technol*. 5(1), 16-23 (1987).

[37] W. P. Huang, L. Hang, and J. Mu, “A rigorous circuit model for simulation of large-scale photonic integrated circuits”, *IEEE Photonics J.* 4(5), 1622-1639 (2012)

[38] D. Marcuse, “Theory of dielectric optical waveguides,” Academic, New York, 1991.

[39] A. W. Snyder and J. D. Love, “Optical Waveguide Theory,” Chapman and Hall, New York, 1983.

[40] R. Sammut and A. W. Snyder, "Leaky modes on a dielectric waveguide: Orthogonality and excitation," *Appl. Opt.* 15(4), 1040-1044(1976).

[41] A. K. Ghatak. "Leaky modes in optical waveguides," *Opt. Quant. Electro.* 17(5) 311-321 (1985).

[42] S. L. Lee, Y. C. Chung, L. A. Coldren, and N. Dagli, "On leaky mode approximations for modal expansion in multilayer open waveguides," *IEEE J. Quantum Electron*. 31(10), 1790-1802 (1995).

[43] J. Zhu and Y. Y. Lu. "Leaky modes of slab waveguides—Asymptotic solutions," *J. Lightwave Technol.* 24(3), 1619 (2006).

[44] S. T. Peng, and A. A. Oliner, "Guidance and Leakage Properties of a Class of Open Dielectric Waveguides: Part I – Mathematical Formulations," *IEEE Trans. Microwave Theory Tech.* MTT-29 (9), 843-855 (1981).

[45] J. P. Berenger, "A perfectly matched layer for the absorption of electromagnetic-waves," *J. Comput. Phys.*144 (2), 185-200 (1993)

[46] W. C. Chew, J. M. Jin, and E. Michielssen, "Complex coordinate stretching as a generalized absorbing boundary condition," *Microwave Opt. Technol. Lett.*15 (6), 363-369 (1997)

[47] C.L. Xu, W.P. Huang, M.S. Stern, and S. K. Chaudhuri, "Full-vectorial mode calculations by finite difference method", *IEE Proc. Optoelectron.* 142 (5), 281-286 (1994).

[48] C. Vassallo, "Improvement of finite difference method for step-index optical waveguides," *Inst. Elect. Eng. Proc.-J.* 139(2), 137-142(1992).

[49] A. B. Fallahkhair, K. S. Li, and T. E. Murphy, "Vector finite difference modesolver for anisotropic dielectric waveguides," *J. Lightwave Technol.* 26(11), 1423-1431 (2008).

[50] B.M.A Rahman, J.B. Davies, "Finite-element analysis of optical and microwave waveguide problems," *IEEE Trans. Microwave Theory Tech.* 32(1), 20-28 (1984).

[51] M. Koshiba, K. Inoue, “Simple and efficient finite-element analysis of microwave and optical waveguides”, *IEEE Microwave Theory Tech.* 40(2), 371-377 (1992).

[52] A. Khalatpour, J. Mu, K. Moussakhani, and W. P. Huang. "Modified Smooth Transition Method for Determination of Complex Modes in Multilayer Waveguide Structures," *J. Lightwave Technol.* 28 (19), 2851-2855 (2010).

[53] Y. P. Chiou and C. H. Du, “Arbitrary-order full-vectorial interface conditions and higher-order finite-difference analysis of optical waveguides,” *J. Lightwave Technol.* 29(22), 3445-3452(2011).

[54] Y. P. Chiou and C. H. Du, “Arbitrary-Order Interface Conditions for Slab Structures and Their Applications in Waveguide Analysis,” *Opt. Express* 18(5), 4088-4102 (2010).

[55] Y. Zhou, Y. Xia, H. Zhang, and F. Luan. "Metallic diffraction grating enhanced coupling in whispering gallery resonator," *Opt. Express* 21(7) 8939-8944 (2013).

[56] Y. Li, L. Li, B. Tian, G. Roelkens, and R. Baets. "Reflectionless tilted grating couplers with improved coupling efficiency based on a silicon overlay," *IEEE Photonics Technol. Lett.* 25(3) 1195-1198 (2013).

[57] C. L. Zou, F. J. Sun, Z. J. Gong, Z. F. Hang, and G. C. Guo. "Theory of free space coupling to high-Q whispering gallery modes," *Opt. Express* 21(8) 9982-9995 (2013).

[58] J. Mu and W. P. Huang. "Analytical Expressions for Radiation Effects on Guided Mode Propagation in Long Period Gratings," *J. Lightwave Technol.* 29(7) 997-1002 (2011).

[59] D. Ahn, C. Y. Hong, J. Liu, W. Giziewicz, M. Beals, L. C. Kimerling, J. Michel, J. Chen, and F. X. Knrtner. "High performance, waveguide integrated Ge photodetectors," *Opt. Express* 15(7) 3916-3921 (2007).

[60] H. Derudder, F. Olyslager, D. De Zutter, and S. Van den Berghe. "Efficient mode-matching analysis of discontinuities in finite planar substrates using perfectly matched layers," *IEEE Trans. Antennas Propag.*49(2) 185-195 (2001).

[61] P. Bienstman and R. Baets. "Optical modelling of photonic crystals and VCSELs using eigenmode expansion and perfectly matched layers," *Opt. Quant. Electro.* 33(4-5), 327-341 (2001).

[62] P. Bienstman, H. Derudder, R. Baets, F. Olyslager, and D. De Zutter. "Analysis of cylindrical waveguide discontinuities using vectorial eigenmodes and perfectly matched layers," *IEEE Trans. Microwave Theory Tech.* 49(2), 349-354 (2001).

[63] J. Ctyroky, S. Helfert, R. Pregla, P. Bienstman, R. Baets, R. De Ridder, R. Stoffer, G. Klaasse, J. Petracek, P. Lalanne, J. P. Hugonin, and R. M. De La Rue. "Bragg waveguide grating as a 1D photonic band gap structure: COST 268 modelling task." *Opt. Quant. Eletro.*34(5), 455-470 (2002).

[64] H. Rogier and D. De Zutter. "Berenger and leaky modes in microstrip substrates terminated by a perfectly matched layer," *IEEE Trans. Microwave Theory Tech.* 49(4) 712-715 (2001).

[65] H. Rogier and D. De Zutter. "Berenger and leaky modes in optical fibers terminated with a perfectly matched layer," *J. Lightwave Technol.* 20(7), 1141 (2002).

[66] J. Zhu and Y. Y. Lu. "Asymptotic solutions of eigenmodes in slab waveguides terminated by perfectly matched layers," *J. Opt. Soc. Am. A* 30(10) 2090-2095 (2013).

[67] W. P. Huang and J. Mu. "Complex coupled-mode theory for optical waveguides," *Opt. Express* 17(21) 19134-19152 (2009).

[68] L. Yang, L. L. Xue, Y. C. Lu, and W. P. Huang. "New insight into quasi leaky mode approximations for unified coupled-mode analysis." *Opt. Express* 18(20), 20595-20609 (2010).

[69] J. Mu and W. P. Huang. "Simulation of three-dimensional waveguide discontinuities by a full-vector mode-matching method based on finite-difference schemes," *Opt. Express* 16(22), 18152-18163 (2008).

[70] J. Mu, X. Li, and W. P. Huang, "Compact Bragg Grating with Embedded Metallic Nano-Structures," *Opt. Express* 18(15),15893-15900(2010).

[71] P. Benech, D. A. Khalil, and F. S. Andre. "An exact simplified method for the normalization of radiation modes in planar multilayer structures," *Opt. Commun.* 88(2) 96-100 (1992).

[72] J. Petracek and K. Singh. "Determination of leaky modes in planar multilayer waveguides," *IEEE Photonics Technol. Lett.* 14 (6), 810-812 (2002).

[73] W. C. Chew and W. H. Weedon. "A 3D perfectly matched medium from modified Maxwell's equations with stretched coordinates," Microwave and optical technology letters 7, no. 13 (1994): 599-604.

[74] M. Reed, P. Sewell, T. M. Benson, and P. C. Kendall, "Efficient propagation algorithm for 3D optical waveguides," *IEE P-Optoelectron.* 145(1), 53-58(1998).

[75] G. V. Eleftheriades, A. S. Omar, L. P. B. Katehi, and G. M. Rebeiz, "Some important properties of waveguide junction generalized scattering matrices in the context of the mode matching technique," *IEEE Trans. Microw. Theory Techn.* 42(10), 1896-1903(1994)

[76] K. L. Chan and S. R. Judah, "Mode-matching analysis of a waveguide junction formed by a circular and a larger elliptic waveguide," *IEE Proc. Microw. Anten. P.* 145(1), 123-127(1998).

[77] S. L. Lin, L. W. Li, T. S. Yeo, and M. S. Leong, "Novel unified mode matching analysis of concentric waveguide junctions," *IEE Proc. Microw. Anten. P.*, 148(6), 369-374(2001).

[78] J. Mu and W. P. Huang, "Simulation of three-dimensional waveguide discontinuities by a full-vector mode-matching method based on finite-difference schemes," *Opt. Express* 16(22), 18152-18163(2008).

[79] J Mu, H. Zhang, and W. P. Huang, "Design of waveguide Bragg gratings with strong index corrugations," *J. Lightwave Technol.* 26(12), 1596-1601(2008).

[80] J. Mu, H. Zhang and W. Huang,“A theoretical investigation of slot waveguide Bragg gratings,” *IEEE J. Quantum Elect*. 44(7), 622-627(2008).

[81] R. Wang, L. Han, J. Mu, and W. P. Huang, "Simulation of waveguide crossings and corners with complex mode-matching method," *J. Lightwave Technol.* 30(12), 1795-1801(2012).

[82] M. Hammer, "Quadridirectional eigenmode expansion scheme for 2-D modeling of wave propagation in integrated optics," *Opt. Commun.* 235(4), 285-303(2004).

[83] X. Lu, H. Shi, and Y. Y. Lu, "Vertical mode expansion method for transmission of light through a single circular hole in a slab," *J. Opt. Soc. Am. A.* 31(2), 293-300(2014).

[84] X. Du, S. Vincent, and T. Lu, "Full-vectorial whispering-gallery-mode cavity analysis," *Opt. Express,* 21(19), 22012-22022(2013).

[85] X. Du, S. Vinsent, M. Faucher, M. Picard, and T. Lu, "Generalized full-vector multi-mode matching analysis of whispering gallery microcavities", *Opt. Express* 22(11), 13507-13514(2014).

[86] G. H. Golub and C. F. van Loan, "Orthogonalization and least squares" in *Matrix computations* , 3rd ed. The Johns Hopkins, 1996, pp. 236-237.

[87] A. Melloni, P. Monguzzi, R. Costa, and M. Martinelli, "Design of curved waveguides: the matched bend." *J. Opt. Soc. Am. A.* 20(1), 130-137 (2003).

[88] W. Yuan ,and D. C. Hall, "A General Scaling Rule for Matched Bend Waveguides," *J. Lightwave Technol.* 29(24), 3786-3796 (2011)

[89] K. R. Hiremath, M. Hammer, R. Stoffer, L. Prkna, and J. Ctyroky, "Analytic approach to dielectric optical bent slab waveguides," *Opt. Quant. Electron.*, 37(1-3), 37-61 (2005).

[90] P. Bienstman, E. Six, M. Roelens, M. Vanwolleghem, and R. Baets. "Calculation of bending losses in dielectric waveguides using eigenmode expansion and perfectly matched layers," *IEEE Photonic. Tech. L.*14(2), 164-166(2002).

[91] M. Heiblum and J. H. Harris, "Analysis of curved optical waveguides by conformal transformation," *IEEE J. of Quantum Elect.* 11, 75-83(1975).

[92] D. F. P. Pile, T. Ogawa, D. K. Gramotnev, K. Dmitri, Y. Matsuzaki, K. C.Vernon, C. Kristy, K. Yamaguchi, T. Okamoto, T. Takeshi, M. Haraguchi, and M. Fukui, "Two-dimensionally localized modes of a nano-scale gap plasmon waveguide," *Appl. Phys. Lett.* 87(26), 261114 (2005)

[93] I. Avrutsky, R. Soref, and W. Buchwald, "Sub-wavelength plasmonic modes in a conductor-gap-dielectric system with a nanoscale gap," *Opt. Express* 18(1), 348-363 (2010).

[94] X. Y. Zhang, A. Hu, J. Z. Wen, T. Zhang, X. J. Xue, Y. Zhou and W. W. Duley, "Numerical analysis of deep sub-wavelength integrated plasmonic devices based on semiconductor-insulator-metal strip waveguides," *Opt. Express* 18(18), 18945-18959 (2010).

[95] C. Huang, R. J. Lamond, S. K. Pickus, Z. R. Li and V. J. Sorger, "A sub-λ-size modulator beyond the efficiency-loss limit," *IEEE Photonics J.* 5(4), 2202411 (2013).

[96] J. Mu, R. Soref, L. C. Kimerling, and J. Michel "Silicon-on-nitride structures for mid-infrared gap-plasmon waveguiding," *Appl. Phys. Lett.* 104(3), 031115 (2014).

[97] R. Adato and J. Guo "Characteristics of ultra-long range surface plasmon waves at optical frequencies," *Opt. Express* 15(8), 5008-5017 (2007).

[98] Y. Bian and Q. Gong, "Low-loss light transport at the subwavelength scale in silicon nano-slot based symmetric hybrid plasmonic waveguiding schemes," *Opt. Express* 21(20), 23907-23920 (2013).

[99] M. Z. Alam, J. S. Aitchison , and M. Mojahedi, "A marriage of convenience: Hybridization of surface plasmon and dielectric waveguide modes," *Laser & Photonics Reviews* 8(3), 394-408 (2014).

[100] H. S. Chu, E. P. Li, P. Bai and R. Hegde, "Optical performance of single-mode hybrid dielectric-loaded plasmonic waveguide-based components," *Appl. Phys. Lett.* 96(22), 221103 (2010).

[101] M. Z. Alam, J. Meier, J. S. Aitchison and M. Mojahedi, "Propagation characteristics of hybrid modes supported by metal-low-high index waveguides and bends," *Opt. Express* 18(12), 12971-129792010).

[102] V.R. Almeida, Q. Xu, C.A. Barrios, and M. Lipson, "Guiding and confining light in void nanostructure," *Opt. Lett.* 29, (11), 1209-1211, (2004).

[103] M. Bass, C. DeCusatis, J. Enoch, V. Lakshminarayanan, G. Li, C. MacDonald, V. Mahajan, and E. V. Stryland, "Handbook of Optics, ", 3rd edition (McGraw-Hill, 2009), Chap. 4

[104] E. D. Palik, "Handbook of Optical Constants of Solids," (Academic, 1985), Chap. 1-3.

[105] D. Tanaka, Y. Shoji, M. Kuwahara, X. Wang, K. Kintaka, H. Kawashimi, T. Toyosaki, Y. Ikuma, and H. Tsuda, "Ultra-small self-holding, optical gate switch using Ge2Sb2Te5 with a multi-mode Si waveguide," *Opt. Express* 20(9) ,10283-10294 (2012).

[106] T. Moriyama, H. Kawashima, M. Kywahara, X. Wang, H. Asakura, and H. Tsuda, "Small-sized Mach-Zehnder interferometer optical switch using thin film Ge2Sb2Te5 phase-change material," in Optical Fiber Communication Conference , San Francisco , CA, 2014, paper Tu3E-4.

[107] W. H. P. Pernice and H. Bhaskaran, "Photonic non-volatile memories using s," *Appl. Phys. Lett.* 101(17) , 171101(2012).

[108] P. Hosseni, C. D. Wright, and H. Bhaskaran, "An optoelectronic framework enabled by low-dimensional phase-change films," *Nature* 511(7508), 206-211 (2014).

[109] K. J. A. Ooi, P. Bai, H. S. Chu and L. K. Ang, "Ultracompact vanadium dioxide dual-mode plasmonic waveguide electroabsorption modulator," *Nanophotonics* 2(1), 13-19 (2013).

[110] P. Markov, J. D. Rykman, R. E. Marvel, K. A. Hallman, R. F. Haglund and S. M. Weiss, "Silicon-VO2 hybrid electro-optic modulator," in CLEO: Science and innovations, 2013, paper CTu2F-7.

[111] C. Ye, S. Khan, Z. R. Li, E. Simsek, and V. J. Sorger, "λ-size ITO and Graphene-based electro-optic modulators on SOI," *IEEE J. of Sel. Top Quant. Electron.* 20(4), 3400310 (2014).

[112] D. Ielmini, A. L. Lacaita, A. Pirovano, F. Pellizzer, R. Bez, "Analysis of Phase Distribution in Phase-Change Nonvolatile Memories," *IEEE Electron Device Lett.* 25(7), 507-509 (2004).

[113] V. Weidenhof, I. Friedrich, S. Ziegler, and M. Wutting, "Laser induced crystallization of amorphous Ge2Sb2Te5 films," *J Appl. Phys.* 89(6), 3168-3176 (2001).

[114] V. Weidenhof, N. Pirch, I. Friedrich, S. Ziegler, and M. Wutting, "Minimum time for laser induced amorphization of Ge2Sb2Te5 films, "*J Appl. Phys.* 88(2), 657–664(2000).

[115] S. Okamine, S. Hirasawa, M. Terao, and Y. Miyauchi, "Computer simulation of material flow induced by thermal deformation In phase-change recording films", In Applications of Artificial Neural Networks, International Society for Optics and Photonics, 1992, pp. 315-321.

[116] W. J. Wang, L. P. Shi, R. Zhao,K. G. Lim, H. K. Lee, T. C. Chong and Y. H. Wu, "Fast phase transitions induced by picosecond electrical pulses on phase change memory cells," *Appl. Phys. Lett.* 93(4), 043121 (2008).

[117] M. Wuttig, N. Yamada, "Phase-change materials for rewriteable data storage," *Nat. Mater.* 6 (11), 824-832(2007).

[118] R. Soref, "Mid-infrared 2 x 2 electro-optical switching by silicon and germanium three-waveguide and four-waveguide directional couplers using free-carrier injection," *Photonics Res.* 2 (5), 102-110 (2014).

[119] J. Hendrickson, R. Soref, J. Sweet, and W. Buchwald, "Ultrasensitive silicon photonic-crystal nanobeam electro-optical modulator: design and simulation," *Opt. Express* 22(3), 3271-3283(2014).

[120] R. Soref, J. Guo, and G. Sun, "Low-energy MOS depletion modulators in silicon-on-insulator micro-donut resonators coupled to bus waveguides," *Opt. Express* 19(19), 18122-18134(2011).

[121] S. Y. Kim, S. J. Kim, H. Seo, and M. R. Kim, "Variation of the complex refractive indices with Sb-addition in Ge-Sb-Te alloy and their wavelength dependence," in Optical Data Storage'99, pp. 112-115,1998.

[122] J. Orava, T. Wagner, J. Sik, J. Pnkryl, M. Frumar, and L. Benes, "Optical properties and phase change transition in Ge2Sb2Te5 flash evaporated thin films studied by temperature dependent spectroscopic ellipsometry," *J. Appl. Phys., vol.* 104(4), 043523(2008).

[123] B. Gholipour, J. Zhang, K. F. MacDonald, D. W. Hewak, and N. I. Zheludev, "An all-optical non-volatile, bidirectional, phase-change meta-switch," *Adv. Mater.* 25(22), 3050-3054 (2013).

[124] N. Yamada, "Development of materials for third generation optical storage media" in s: Science and Applications, S. Raoux and M. Wuttig, eds, Springer, 2009, pp. 199-226.

[125] D. Strand, D. V. Tsu, R. Miller, M. Hennessey, and D. Jablonski, "Optical routers based on Ovonic s," presented at the European Phase Change and Ovonic Science Symposium, Grenoble, France, 2006.

[126] Y. F. Choi, "Phase-change materials: trends and prospects," presented at the ECI Workshop, Lehigh University, Jan 10, 2013.

[127] K. Shportko, S. Kremers, M. Woda, D. Lencer, J. Robertson, and M. Wuttig, "Resonant bonding in crystalline phase-change materials," *Nat. Mater.* 7(8), 653-658 (2008).

[128] H. Tsuda, D. Tanaka, M. Kuwahara, and X. Wang, "Self-holding optical switch using phase-change material for energy efficient photonic network," in The 24th Symposium on Phase Change Oriented Science (PCOS 2012), , Hamamatsu, Japan, 2012, pp. A13.

[129] M. N. Petrovich, F. Poletti, J. P. Wooler, A. M.Heidt, N. K. Baddela, Z. Li, D. R. Gray et al., "Demonstration of amplified data transmission at 2 μm in a low-loss wide bandwidth hollow core photonic bandgap fiber," *Opt. Express* 21(23), 20559-20569(2013).

[130] M. Nedeljkovic, R. A. Soref and G. Z. Mashanovich, "Free-carrier electrorefraction and electroabsorption modulation predictions for silicon over the 1-14 μm infrared wavelength range," *IEEE Photonics J.* 3(6), 1171-1180 (2011).

[131] T. Tsuchizawa, K. Yamada, T. Watanabe, S. Park, H. Nishi, R. Kou, H. Shinojima and S. Itabashi, "Monolithic integration of silicon-, germanium-, and silica-based optical devices for telecommunications applications," *IEEE. J. of Sel. Topics in Quant. Elect.* 17(3), 516-527(2011).

[132] H. Liang, J. Mu, X. Li, and W.P. Huang, "insights into complex Berenger modes: a view from the weighted optical path distance perspective", *Opt. Lett.* 39(9), 2811-2814(2014).

[133] B. M. Rude, J. Pello, R. E. Simpson, J. Osmond, G. Roelkens, J. J. G. M. van der Tol, and V. Pruneri, "Optical switching at 1.55 μm in silicon racetrack resonators using s," *Appl. Phys. Lett.* 103(14), 141119 (2013).

[134] A. Joushaghani, J. Jeong, S. Paradis, D. Alain, J. S. Aitchison and J. K. S. Poon, "Wavelength-size hybrid Si-VO2 electroabsorption optical switches and photodetectors," *Opt. Express* 23(3), 3657-3668 (2015).

[135] J. Mu, Z. Han, S. Grillanda, A. Melloni, J. Michel, L. C. Kimerling, and A. Agarwal, "Towards ultra-subwavelength optical latches," *Appl. Phys. Lett.* 103(4), 043115 (2013).

[136] S. Raoux, F. Xiong, M. Wuttig, and E. Pop, "s and phase change memory," *MRS Bull.* 39(8), 703-711 (2014).

[137] D. Lener, M. Salinga, B. Grabowski, T. Hickel, J. Neugebauer, and M. Wuttig, "A map for phase-change materials," *Nat. Mater.* 7(12), 972 (2008).

[138] R. Soref, J. Hendrickson, H. Liang, A. Majumdar, J. Mu, X. Li, and W.P. Huang, "Electro-optical switching at 1550 nm using a two-state GeSe phase-change material," *Opt. Express* 23(2), 1536-1546 (2015).

[139] R. A. Integlia, L. Yin, D. Ding, D. Z. Pan, D. M. Gill, and W. Jiang, "Parallel-coupled dual racetrack silicon micro-resonators for quadrature amplitude modulation", *Opt. Express* 19(16), 14892-14902 (2011).

[140] O. D. Herrera, R. Himmelhuber, K. J. Kim, R. A. Norwood, and N. N. Peyghambarian, "Silicon/electro-optic polymer hybrid directional coupler switch," in SPIE OPTO (International Society for Optics and Photonics 2014), p.89910Q.

[141] R. A. Norwood, "Organic electro-optic materials and devices: molecular engineering driving device performance and technology innovation ," in CLEO: Science and Innovations (Optical Society of America 2014), p. SM2M.1.